

AD-A051 134

UTAH STATE UNIV LOGAN SPACE SCIENCE LAB

F/G 20/14

ANALYSIS OF THE FARADAY ROTATION DIFFERENTIAL ABSORPTION TECHNI--ETC(U)

AUG 77 K D BAKER, R D HARRIS, R A MCCUE F19628-74-C-0130

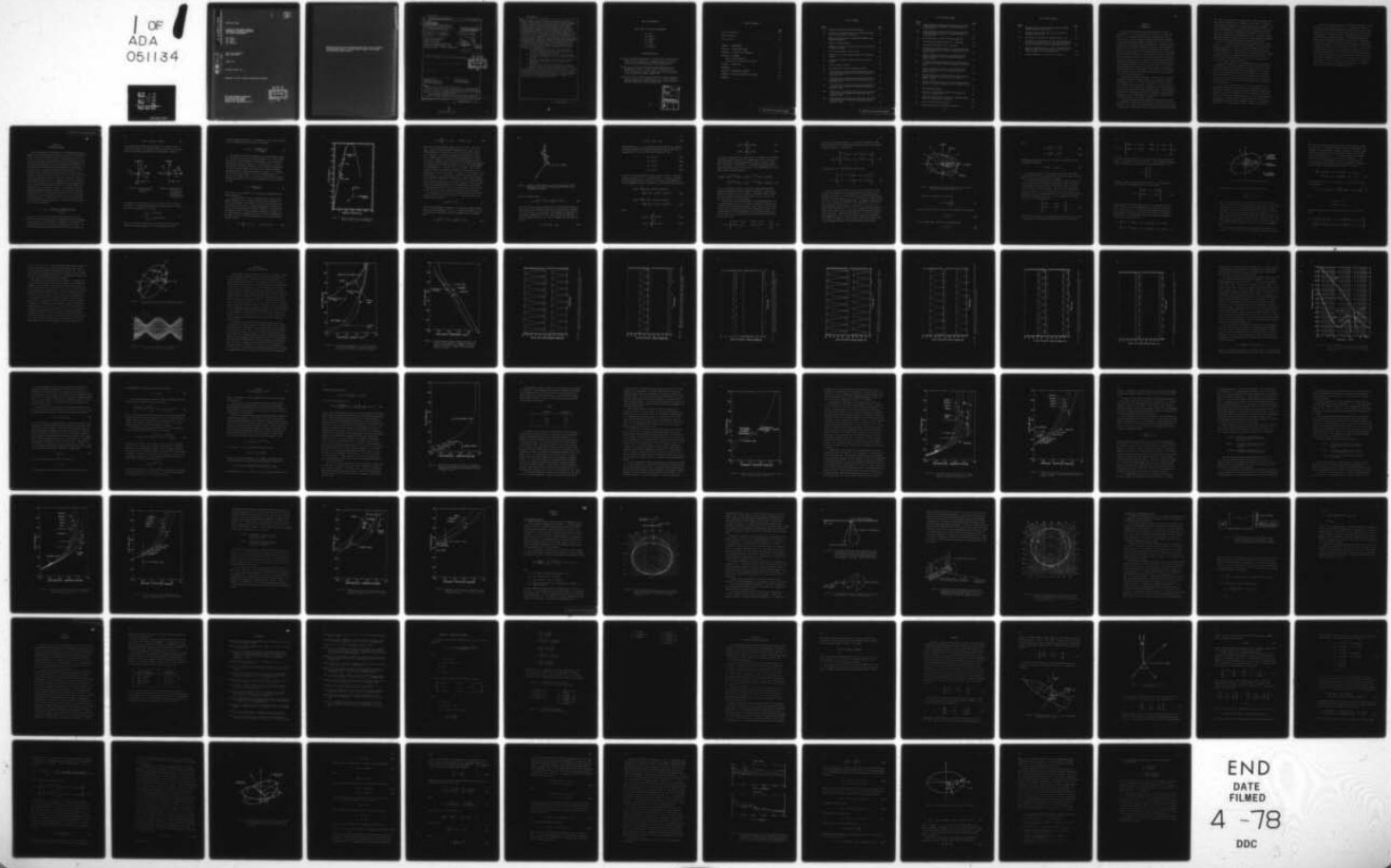
UNCLASSIFIED

SCIENTIFIC-4

AFGL-TR-77-0184

NL

1 OF
ADA
051134



END
DATE
FILMED
4 -78
DDC

AD A 051134

AFGL-TR-77-0184

(2)

ANALYSIS OF THE FARADAY ROTATION
DIFFERENTIAL ABSORPTION TECHNIQUE
FOR D-REGION MEASUREMENTS

R.A. McCue
R.D. Harris
K.D. Baker
C.D. Westlund

AD No.
FILE COPY

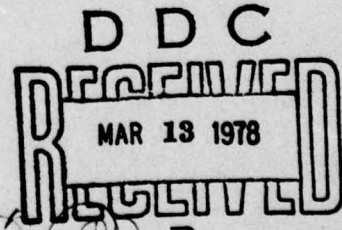
Utah State University
Logan, Utah 84322

August 1977

Scientific Report No. 4

Approved for public release; distribution unlimited

AIR FORCE GEOPHYSICS LABORATORY
AIR FORCE SYSTEMS COMMAND
UNITED STATES AIR FORCE
HASNSCOM AFB, MASSACHUSETTS 01731



Qualified requestors may obtain additional copies from the Defense Documentation Center. All others should apply to the National Technical Information Service.

Unclassified

SECURITY CLASSIFICATION OF THIS PAGE (When Data Entered)

19 REPORT DOCUMENTATION PAGE		
1 REF ID NUMBER AFGL-TR-77-0184	2 GOVT ACCESSION NO.	3 RECIPIENT'S CATALOG NUMBER
4 TITLE (Include Subtitle) Analysis of the Faraday Rotation Differential Absorption Technique for D-Region Measurements		
5 AUTHOR(S) R.A./McCue → K.D./Baker, R.D./Harris C.D./Westlund	6 TYPE OF REPORT & PERIOD COVERED Scientific Report No. 4	
7 PERFORMING ORGANIZATION NAME AND ADDRESS Space Science Laboratory Utah State University Logan, Utah 84322	8 PERFORMING ORGANIZATION REPORT NUMBER 10 SCIENTIFIC-4	
9 CONTROLLING OFFICE NAME AND ADDRESS Air Force Geophysics Laboratory Hanscom AFB, Massachusetts 01731 Contract Monitor: Thomas D. Conley/CPR	10 PROGRAM ELEMENT, PROJECT, TASK AREA & WORK UNIT NUMBER 76701004	
11 MONITORING AGENCY NAME & ADDRESS (if different from Controlling Office)	12 REPORT DATE August 1977	
13 NUMBER OF PAGES 97	14 NUMBER OF PAGES 94P	
15 SECURITY CLASSIFICATION OF THIS REPORT Unclassified		
16 DECLASSIFICATION/DOWNGRADING SCHEDULE		
17 DISTRIBUTION STATEMENT (for this report) Approved for public release; distribution unlimited		
18 DISTRIBUTION STATEMENT (for the abstract entered in Block 20, if different from Report)		
19 KEY WORDS (Continue on reverse side if necessary and identify by block number) FARADAY ROTATION ELECTRON DENSITY DIFFERENTIAL ABSORPTION COLLISION FREQUENCY RADIO WAVE PROPAGATION		
20 ABSTRACT (Continue on reverse side if necessary and identify by block number) This report describes the optimization of a radio propagation experiment suitable for studies of the ionosphere D-region utilizing relatively low power, portable ground-based transmitters and simple receivers aboard small sounding rockets. A wave propagation model has been developed that numerically calculates the radio signal that would be received by a dipole		

DD FORM 1 JAN 73 1473 EDITION OF 1 NOV 65 IS OBSOLETE

Unclassified
SECURITY CLASSIFICATION OF THIS PAGE (When Data Entered)

i
407 724
W

Unclassified

SECURITY CLASSIFICATION OF THIS PAGE When Data Entered)

antenna aboard a rocket traveling up through the ionospheric D-region. The Faraday rotation and differential absorption experienced by the wave can be used to deduce both electron concentrations and electron-neutral collision rates in the D-region. Faraday rotation and differential absorption were numerically calculated for a number of radio frequencies for three types of extreme conditions such as occur at high magnetic latitudes. Altitude profiles of these quantities provide information to base a selection of 2 or 3 frequencies that will yield maximum information on electron density and collision rate, based on the expected ionospheric conditions. The propagation experiment proposed employs multiple frequencies together with low power transmitters, and inexpensive, movable antennas. Signal limitations such as atmospheric noise, telemetry error and transmission power were also used to interpret the Faraday rotation and differential absorption curves in order to achieve maximum accuracy. The results of this analysis are:

- 1) For high electron density (PCA conditions) and low collision frequency conditions, wave frequencies of 3.25, 10, and 19 MHz should be used.
- 2) For high electron density and high collision frequency conditions, frequencies of 3.25, 14, and 25 MHz should be used.
- 3) For low electron density and low collision frequency conditions, frequencies of 3.25 and 4.25 MHz are sufficient.
- 4) For low electron density and high collision frequency conditions, 3.25 and 6 MHz frequencies are sufficient.

A method of estimating transmission power and rocket receiver range requirements (based on noise levels) was developed, as well as equations by which coning modulation of the received signal can be separated from actual Faraday rotation and differential absorption. A data reduction scheme was developed to remove errors associated with the motions of the rocket.

Unclassified

SECURITY CLASSIFICATION OF THIS PAGE When Data Entered)

LIST OF CONTRIBUTORS

Kay D. Baker - Principal Investigator

D.A. Burt
R.D. Harris
L.C. Howlett
R.A. McCue
E.F. Pound
C.D. Westlund

RELATED PUBLICATIONS

Neal, P.C., Design and calibration of a rocket-borne electron spectrometer, *Scientific Report No. 1 - HAES Report No. 8, AFCRL-TR-74-0629*, 78 pp., Contract No. F19628-74-C-0130, Space Science Laboratory, Utah State University, Logan, December 1974.

Howlett, L.C. and R.J. Bell, Rocketborne instrumentation for the measurement of electric fields - Paiute Tomahawk 10.312-3, *Scientific Report No. 2 - HAES Report No. 11, AFCRL-TR-75-0023*, 91 pp., Contract No. F19628-74-C-0130, Space Science Laboratory, Utah State University, Logan, January 1975.

Grieder, W.F. and L.A. Whelan, Geometric aspects of rocket photometry, *Scientific Report No. 3 - HAES Report No. 41, AFGL-TR-76-0046*, 107 pp., Contract No. F19628-74-C-0130, Space Science Laboratory, Utah State University, Logan, February 1976.

1011721

ACCESSION for	
NTIS	White Section <input checked="" type="checkbox"/>
DDC	Buff Section <input type="checkbox"/>
UNANNOUNCED	<input type="checkbox"/>
JUSTIFICATION _____	
BY _____	
DISTRIBUTION/AVAILABILITY CODES	
Dist.	AVAIL and/or SPECIAL
A	

TABLE OF CONTENTS

	<u>Page</u>
List of Contributors	iii
Table of Contents	v
List of Figures	vii
CHAPTER I - INTRODUCTION	1
CHAPTER II - PROPAGATION THEORY	5
CHAPTER III - SELECTION OF FREQUENCIES	21
CHAPTER IV - ANTENNAS.	53
Ground Station Antennas	53
Antennas for the Rocketborne Receiver	59
CHAPTER V - CONCLUSIONS	63
REFERENCES.	65
APPENDIX A - MAGNETOIONIC FORMULAS	A-1
APPENDIX B - THE WAVE ELECTRIC FIELD VECTOR	B-1
APPENDIX C.	C-1

LIST OF FIGURES

<u>Figure</u>		<u>Page</u>
1a	Rotation of $H/ H $ for increasing altitude	6
1b	Rotation of the complex unit Tr_1 as altitude increases for the VHF frequency in Figure 1a.	6
2	Rocket trajectory for all computations dependent upon trajectory parameters	8
3	EM wave coordinate system	9
4	Relation of the \underline{x}^r , \underline{y}^r axes to the \underline{x}' , \underline{y}' axes for two different altitudes	13
5	Relationship between coordinate axes	16
6a	Projection of \underline{E}^r onto antenna relative to the \underline{E} -field ellipse	20
6b	V_s and V_R as function of time, one rotation of the antenna	20
7	Electron density profiles	22
8	Electron-neutral collision frequency profiles	23
9a	7 MHz signal for disturbed electron density and winter collision frequency profiles for rocket altitudes of 50 km and 55 km	24
9b	7 MHz signal for disturbed electron density and winter collision frequency profiles for rocket altitudes of 60 km and 65 km	25
9c	7 MHz signal for disturbed electron density and winter collision frequency profiles for rocket altitudes of 70 km and 75 km	26
10a	20 MHz signal for disturbed electron density and winter collision frequency profiles for rocket altitudes of 50 km and 55 km	27
10b	20 MHz signal for disturbed electron density and winter collision frequency profiles for rocket altitudes of 60 km and 65 km	28

LIST OF FIGURES (CONT.)

<u>Figure</u>		<u>Page</u>
10c	20 MHz signal for disturbed electron density and winter collision frequency profiles for rocket altitudes of 70 km and 75 km	29
10d	20 MHz signal for disturbed electron density and winter collision frequency profiles for rocket altitudes of 85 km and 95 km	30
11	Noise temperature at medium and high frequencies	32
12	Differential absorption profile for a 7 MHz wave	37
13	Faraday rotation profile for a 7 MHz wave	42
14	Differential absorption profiles for the disturbed electron density and winter collision frequency profiles of Figures 7 and 8	44
15	Faraday rotation profiles for the disturbed electron density and winter collision frequency profiles of Figures 7 and 8	45
16	Differential absorption profiles for the disturbed electron density and summer collision frequency of Figures 7 and 8	47
17	Faraday rotation profiles for the disturbed electron density and summer collision frequency profiles of Figures 7 and 8	48
18	Differential absorption profiles for the quiet electron density and winter collision frequency profiles of Figures 7 and 8	49
19	Faraday rotation profiles for the quiet electron density and winter collision frequency profiles of Figures 7 and 8	50
20	Half-wavelength dipoles	54
21	Three-wire folded half-wavelength antenna phased and driven by a coaxial cable	56
22	Tuned matching network for matching an unbalanced signal source to a balanced dipole antenna	56
23	Antenna and screen configurations	57
24	Measured normalized field intensity patterns	58

LIST OF FIGURES (CONT.)

<u>Figure</u>		<u>Page</u>
25	Experimental test used to determine antenna terminal voltage versus field intensity	60
C1	Stationary antenna frame (\underline{x}^a , \underline{y}^a , \underline{z}^a) orientation relative to (\underline{x}^t , \underline{y}^t , \underline{z}^t)	C-2
C2	Orientation of (\underline{x}^b , \underline{y}^b , \underline{z}^b) relative to (\underline{x}^t , \underline{y}^t , \underline{z}^t) .	C-3
C3	Orientation of the antenna plane (\underline{x}^a , \underline{y}^a) determined by the spinning antenna relative to the plane of polarization for all motion variables except spin held fixed	C-8
C4	Typical signal modulation of rocket coning-shaded region indicates signal envelope modulation relative to the signal envelope for a non-coning rocket	C-13
C5	<u>E</u> -field components in the plane of the antenna	C-15

CHAPTER I INTRODUCTION

In recent years several propagation experiments have been reported [Mechtly *et al.*, 1967; Kane, 1959; Bennett *et al.*, 1972; and Megill *et al.*, 1971] which determine electron density and electron collision rate from the Faraday rotation and differential absorption of radio waves propagating between the ground and a rocket vehicle. It is well known that radio waves propagating in an anisotropic plasma medium, such as the earth's ionosphere, propagate in the independent modes called the ordinary and extraordinary modes [Kelso, 1964]. The propagation characteristics of each mode reveal that the extraordinary wave is absorbed faster than the ordinary wave, the result being that when the propagation direction is near parallelism with the geomagnetic figure, the total wave, which is the sum of the two modes, experiences an amplitude modulation and a change in the wave polarization as the wave propagates through the medium. The former effect is called differential absorption and the latter Faraday rotation. By measuring each of these phenomena independently it is possible to work backwards via a propagation theory and uniquely determine the electron density and electron collision frequency.

Kane [1959] performed an experiment to measure electron collision frequencies when the ionization density of the ionospheric D region was anomalously high. A 7.75 MHz radio signal and its 6th harmonic were transmitted from a rocketborne transmitter to a ground receiver. On the ground the low frequency was multiplied by 6 and compared with the ordinary component of the high frequency signal. By utilizing the resulting beat frequency and the signal strengths of the two polarization modes of the 7.75 MHz signal, it was possible to determine the collision frequency as a function of altitude.

A high resolution propagation system to measure Faraday rotation and differential absorption was developed by the University of Illinois [Mechtly *et al.*, 1967]. This system employed an elaborate antenna and a constant power transmitter to launch a circularly polarized 3.385 MHz

wave into the ionosphere as the ordinary mode. The extraordinary mode was generated 500 hz higher in frequency, but was part of a variable power feedback loop which held the extraordinary signal strength at the rocket (modulation ratio) at a constant ratio to the ordinary wave. By carefully calibrating the transmitter power and recording the rocket roll rate by independent instruments it was possible to extract both differential absorption and Faraday rotation data. With both of these propagation quantities measured, both the electron density and electron collision frequency could be uniquely determined from the data.

Megill et al. [1971] measured the electron density with a 3 frequency (7, 17, 27 MHz) Faraday rotation experiment. The data were considered satisfactory as long as the Sen-Wyller [1960] and modified Appleton-Hartree [Kelso, 1964] forms (modified by using an effective collision frequency $v' = (5/2)v_m$ where v_m is momentum-transfer collision frequency) of the wave propagation differed by less than a factor of 2. It was found that neither theory gave satisfactory results when the radio wave frequency was less than $v_m/1.2$.

Total electron content along a propagation path was determined by *Dean* [1972] by transmitting 6 continuous wave (CW) frequencies from a rocketborne beacon. Three frequencies were harmonically related and phase coherent so that dispersive phase measurements could be made. The other 3 frequencies were used for determination of rf absorption. By receiving both the left and right hand polarized wave components, the rocket spin effects and Faraday rotation effects were eliminated. Electron density profiles could then be determined from the dispersive phase measurements.

Bennett et al. [1972] reported a propagation experiment where 3 independent frequencies were transmitted to a rocketborne receiver. Each signal contained the effects of Faraday rotation and differential absorption. At any given altitude one of the frequencies yielded the most accurate data, so 3 values were chosen to cover the altitude range of interest. By utilizing these data with either the Sen-Wyller or Appleton-Hartree magneto-ionic propagation theories, it was possible to reconstruct electron density and electron collision rate profiles.

In view of the complexity of some of the above experiments, it was desirable to investigate the possibility of a propagation experiment that would utilize simple and portable antennas, and inexpensive transmitters in order that the experiment would be modest in cost and could be transported to remote field sites. This work describes such a multiple frequency propagation experiment. The propagation model was developed for high magnetic latitudes and includes the considerations of errors due to noise, reflections and rocket coning. The signal received by a spinning rocket was developed in Chapter II. These results are employed in Chapter III to illustrate the Faraday rotation and differential absorption that results from extreme values of polar ionospheric D-region conditions. From these curves we developed methods for predicting optimum wave frequencies and specifications for receiver gain levels. Potential errors due to rocket coning are evaluated in the appendix, and a method is developed to systematically eliminate these errors. Finally, a discussion and evaluation of transmitting and receiving antennas is reported in Chapter IV.

CHAPTER II
PROPAGATION THEORY

The initial mathematical descriptions of electromagnetic wave propagation in the ionosphere were developed by Appleton [1932] and Hartree [1931]. Their equation, which described the refractive index of the wave as a function of electron density, collision frequency, wave frequency and propagation direction with respect to the geomagnetic field, has come to be appropriately called the Appleton-Hartree equation. In this derivation the collision process was assumed to be independent of electron energy. Subsequent experiments have shown [Phelps and Pack, 1959] that the electron-neutral collision process is indeed energy-dependent. This fact was utilized by Sen and Wyller [1960] in an extension of the magnetoionic formulas of Appleton and Hartree. Numerous experiments have shown this latter formulation to better describe the actual characteristics of an electro-magnetic wave in a plasma medium. Both of the above-mentioned theories show that a plasma immersed in a magnetic field is a birefringent medium; i.e. regardless of the wave configuration impinging upon the medium, only two possible modes will propagate internally. These propagation modes can then be described in part by their complex indices of refraction n_o , n_x and their wave polarizations R_o , R_x . The subscripts o and x refer to the "ordinary" and "extraordinary" modes, respectively. The refractive indices given by Sen and Wyller [1960] are

$$n^2 = (\mu - j\chi)^2 = \frac{A + B\sin^2\phi \pm \sqrt{B^2\sin^4\phi - C^2\cos^2\phi}}{D + E\sin^2\phi}$$

where A, B, C, D and E are functions of electron density, electron-neutral collision frequency, electron gyrofrequency, and wave frequency, and are repeated for ready reference in Appendix A. The variable ϕ is the angle between the earth's magnetic field B_e and the ray path. For an upward moving wave the quantity under the radical in equation (1)

$$H(z, \phi) = B^2 \sin^4 \phi - C^2 \cos^2 \phi \quad (2)$$

is a complex number which rotates clockwise in the complex plane as altitude z increases. The normalized values of equation (2) are represented by the lengths and angles of the arrows shown in Figure 1a.

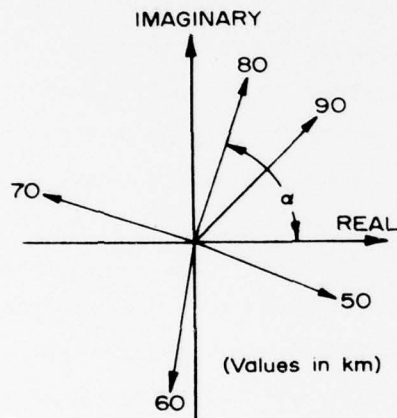


Figure 1a. Rotation of $H/|H|$ for increasing altitude.

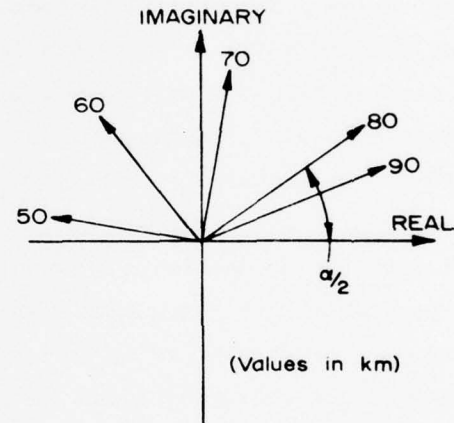


Figure 1b. Rotation of the complex unit Tr_1 as altitude increases for the VHF frequency in Figure 1a.

An ambiguity in the interpretation of the two modes of (1) may arise because \sqrt{H} is a complex, double-branched function of a complex variable. The two branch functions can be written

$$\sqrt{H} = \begin{cases} Tr_1 = |H|^{1/2} e^{j\alpha/2} \\ Tr_2 = |H|^{1/2} e^{j(\alpha/2-\pi)} \end{cases} \quad (3)$$

where α is the angle between the real axis and the radius vector described by the complex number $H/|H|$. The variation of Tr_1 with

altitude is shown in Figure 1b. The ambiguity in (1) can now be removed if Tr_1 is substituted for the radical in (1) giving

$$(\mu - j\chi)^2 = \frac{A + B\sin^2\phi \pm \text{Tr}_1}{D + E\sin^2\phi} \quad (4)$$

The ordinary mode of wave propagation can now be defined by using the "+" sign in (4) and the extraordinary mode by the "-" sign regardless of the relative magnitudes of gyrofrequency and wave frequency. One obvious advantage of using (4) in computing indices is that the ordinary and extraordinary components can be determined independently of the values of gyrofrequency, wave frequency, collision frequency, and plasma frequency, which are imbedded in the angle α . In addition, the discontinuity encountered by Ratcliffe [1962] (pp. 69-70 and Figure 7.4) no longer occurs. The function H also appears in the wave polarization equation of Sen and Wyller [1960] which can be written in the form

$$R = - \frac{B\sin^2\phi \pm \text{Tr}_1}{C\cos\phi} \quad (5)$$

where again + and - correspond to the ordinary and extraordinary wave modes, respectively.

A coordinate system (\underline{x} , \underline{y} , \underline{z}) is defined with \underline{z} vertical and \underline{y} pointing magnetic north. A typical rocket trajectory illustrated in Figure 2 is described in this system. Only the trajectory upleg will be considered in this report. The wave propagation is defined in the (\underline{x}' , \underline{y}' , \underline{z}') coordinate system, where \underline{z}' is parallel to the direction of propagation and \underline{y}' lies in the magnetic meridian. The angle ϕ is the angle between the geomagnetic field in the northern hemisphere and the upward ray path. The wave polarization in the latter coordinate system is given by

$$R_o = \frac{-E_{oy}}{E_{ox}} = \delta_o + j\gamma_o \quad \text{with } \delta_o, \gamma_o \text{ real} \quad (6a)$$

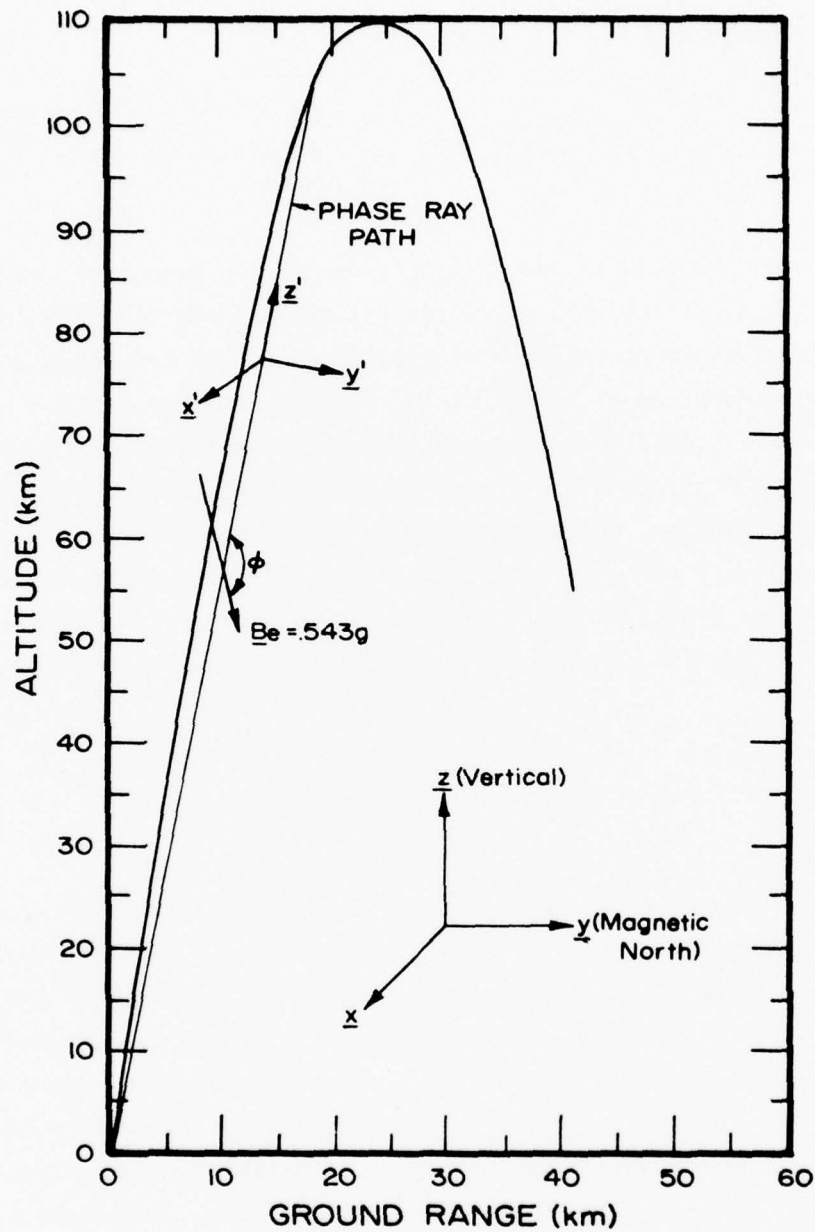


Figure 2. Rocket trajectory for all computations dependent upon trajectory parameters.

$$R_x = \frac{-E_{xy}}{E_{xx}} = \delta_x + j\gamma_x \quad \text{with } \delta_x, \gamma_x \text{ real} \quad (6b)$$

where the total ordinary wave component of the electric field is $\underline{E}_o = E_{ox}\underline{x}' + E_{oy}\underline{y}'$ and the extraordinary component is $\underline{E}_x = E_{xx}\underline{x}' + E_{xy}\underline{y}'$. The polarization is defined by the ratio of the transverse electric field components. In general, both modes are elliptically polarized since a complex value of R means elliptic polarization [Kelso, 1964, pp. 36,37]. However, for our geometry and for frequencies typically of interest in Faraday rotation and differential absorption measurements, i.e. between 2.5 and 25 MHz, the values of δ_o and γ_x are approximately 10^{-3} while $0.998 < \gamma_o \leq 1.00$ and $-1.00 < \gamma_x < -0.998$. Thus, for the geometry of Figure 2, the wave polarizations of equation (6), can be approximated to good accuracy by $R_o = +j$ and $R_x = -j$ on the upleg of the rocket flight. $R = \pm j$ corresponds to circularly polarized waves in the quasi-longitudinal propagation approximation. Figure 3 shows schematically that $R_o = +j$ and $R_x = -j$. This means that in the Northern hemisphere, the ordinary mode \underline{E} -field rotates clockwise in time when viewed along the $\underline{+z}'$ direction, while the extraordinary mode vector rotates in the opposite direction. Actually, the more general elliptical waves of (6) also rotate in the clockwise and counterclockwise directions.

We assume that the initial wave is excited with the electric field aligned parallel to the \underline{x}' axis (Figure 3). Below the D-region, this \underline{E} -field can be described by

$$\underline{E} = M e^{j(\omega t - kz')} \underline{x}', \quad (7)$$

where k is the propagation coefficient, ω is the wave angular frequency and M is the wave amplitude. For $R \approx \pm j$, the wave described by (7) can be written as the sum of two circularly polarized waves, an ordinary mode

$$\underline{E}_o = \frac{M}{2} e^{j(\omega t - k_o z')} \underline{x}' - j \frac{M}{2} e^{j(\omega t - k_o z')} \underline{y}', \quad (8a)$$

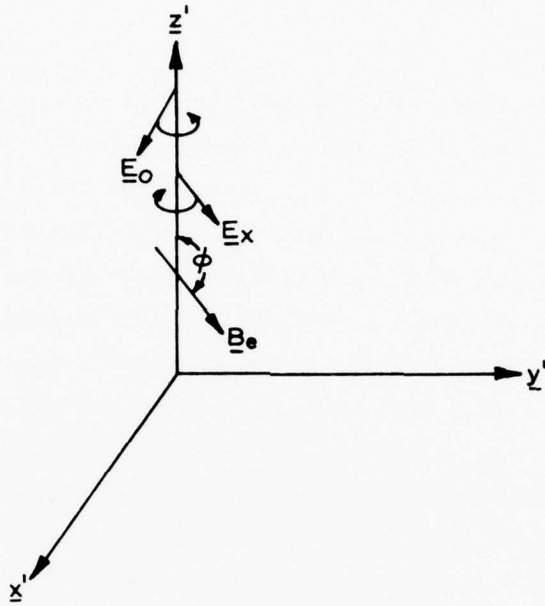


Figure 3. EM wave coordinate system. \underline{B}_e lies in the (\underline{z}' , \underline{y}') plane. Propagation is in the (\underline{z}') direction with rotation of the two modes as indicated.

and an extraordinary mode

$$\underline{E}_x = \frac{M}{2} e^{j(\omega t - k_x z')} \underline{x}' + j \frac{M}{2} e^{j(\omega t - k_x z')} \underline{y}' . \quad (8b)$$

Since the Faraday rotation and differential absorption will be shown to depend only on the difference between the two allowed modes of propagation, the wave phase at the bottom of the ionosphere is arbitrary; for convenience we assume it to be zero. Note that (8a) and (8b) add to give the original plane wave (7). The two propagation coefficients are given by

$$k_o = \frac{w}{c} n_o = \frac{w}{c} (\mu_o - j\chi_o) \quad (9a)$$

$$k_x = \frac{w}{c} n_o = \frac{w}{c} (\mu_x - j\chi_x) \quad (9b)$$

where quantities μ_o , μ_x , χ_o , χ_x depend on electron density N_e , electron collision frequency ν_e , the earth's magnetic field B_e , and the angle of propagation ϕ . If N_e and ν_e vary with altitude only, then

$$\mu_o = \mu_o(z, \phi) \quad (10a)$$

$$\chi_o = \chi_o(z, \phi) \quad (10b)$$

$$\mu_x = \mu_x(z, \phi) \quad (10c)$$

$$\chi_x = \chi_x(z, \phi) \quad (10d)$$

Let $\theta(z)$ be the angle between the z and z' axes of Figure 2. The path length is then given by $z' = z \sec[\theta(z)]$ where z is the vertical height. By substituting (9) and (10) into (8), the electric field components of the two ionospheric modes at a distance h' into the plasma can be written

$$\begin{aligned} E_o(h') &= \frac{M}{2} \exp \left\{ j[\omega t - \phi_o(h')] - \alpha_o(h') \right\} \underline{x}' \\ &\quad + j \frac{M}{2} \exp \left\{ j[\omega t - \phi_o(h')] - \alpha_o(h') \right\} \underline{y}' \end{aligned} \quad (11a)$$

$$\begin{aligned} E_x(h') &= \frac{M}{2} \exp \left\{ j[\omega t - \phi_o(h')] - \alpha_x(h') \right\} \underline{x}' \\ &\quad - j \frac{M}{2} \exp \left\{ j[\omega t - \phi_x(h')] - \alpha_x(h') \right\} \underline{y}' \end{aligned} \quad (11b)$$

where

$$\phi_o(h') = \frac{\omega}{c} \int_0^{h'} \mu_o(z, \phi) dz' \quad (12a)$$

$$\phi_x(h') = \frac{\omega}{c} \int_0^{h'} \mu_x(z, \phi) dz' \quad (12b)$$

$$\alpha_o(h') = \frac{\omega}{c} \int_0^{h'} \chi_o(z, \phi) dz' \quad (12c)$$

$$\alpha_x(h') = \frac{\omega}{c} \int_0^{h'} \chi_x(z, \phi) dz' . \quad (12d)$$

It is shown in Appendix B that the curvature of ray paths in the D-region is extremely small; therefore, it is assumed that $\theta(z)$ is the same for both the ordinary and extraordinary waves and that θ remains constant over a given path. At altitude h , $h = h' \cos[\theta(z)]$, the total E-field is given by the vector sum of (11a) and (11b). The observable part of the total electric field would then be

$$\begin{aligned} \text{Re}[\underline{E}(h)] = & \frac{M}{2} \left\{ e^{-\alpha_o(h)} \cos[\omega t - \phi_o(h)] + e^{-\alpha_x(h)} \cos[\omega t - \phi_x(h)] \right\} \underline{x}' \\ & - \frac{M}{2} \left\{ e^{-\alpha_o(h)} \sin[\omega t - \phi_o(h)] - e^{-\alpha_x(h)} \sin[\omega t - \phi_x(h)] \right\} \underline{y}' . \quad (13) \end{aligned}$$

At a given altitude h , $\text{Re}[\underline{E}(h)]$ represents a vector with direction-dependent magnitude rotating in space with frequency ω . The locus of points traced out by (13) is an ellipse. The maximum length of $\text{Re}(\underline{E})$ will not necessarily be parallel with either the \underline{x}' or \underline{y}' axes, nor are the values of E_x' and E_y' the same.

The next step in the interpretation of the wave propagation is to transform $\text{Re}[\underline{E}(h)]$ of (13) to a coordinate frame which rotates in synchronism with the polarization ellipse. Since ϕ_o and ϕ_x are functions of height, the orientation of the ellipse rotates with altitude. The transformation from the electromagnetic wave coordinate axes ($\underline{x}', \underline{y}', \underline{z}'$) of Figure 3 to the axes ($\underline{x}^r, \underline{y}^r, \underline{z}^r$) rotating about the \underline{z}' axis is given by the matrix

$$R(h) = \begin{bmatrix} \cos[(\phi_o - \phi_x)/2] & \sin[(\phi_o - \phi_x)/2] & 0 \\ -\sin[(\phi_o - \phi_x)/2] & \cos[(\phi_o - \phi_x)/2] & 0 \\ 0 & 0 & 1 \end{bmatrix} . \quad (14)$$

R is seen to be orthogonal [Det(R) = 1], so that R represents a proper rotation from the (\underline{x}' , \underline{y}') axes about the \underline{z}' axis of $(\phi_o - \phi_x)/2$ radians. If (13) is written as a column vector

$$\text{Re}(\underline{E}) = \frac{M}{2} \begin{bmatrix} e^{-\alpha_o} \cos(\omega t - \phi_o) + e^{-\alpha_x} \cos(\omega t - \phi_x) \\ -e^{-\alpha_o} \sin(\omega t - \phi_o) + e^{-\alpha_x} \sin(\omega t - \phi_x) \\ 0 \end{bmatrix} \quad (15)$$

the matrix product $R \cdot [\text{Re}(\underline{E})]$ yields the new vector

$$\underline{E}^r = \frac{M}{2} \begin{bmatrix} (e^{-\alpha_o} + e^{-\alpha_x}) \cos\{[\omega t - (\phi_o + \phi_x)]/2\} \\ -(e^{-\alpha_o} - e^{-\alpha_x}) \sin\{[\omega t - (\phi_o + \phi_x)]/2\} \\ 0 \end{bmatrix} \quad (16)$$

One can easily verify that in the (\underline{x}^r , \underline{y}^r , \underline{z}^r) reference frame \underline{E}^r represents the equation of an ellipse with major axis parallel to \underline{x}^r and minor axis along \underline{y}^r . The relationship is illustrated schematically in Figure 4 where the angle $(\phi_o - \phi_x)/2$ is the angle of rotation between the (\underline{x}' , \underline{y}') and (\underline{x}^r , \underline{y}^r) coordinate axes. The lengths of the major and minor axes are respectively $\frac{M}{2}(e^{-\alpha_o} + e^{-\alpha_x})$ and $\frac{M}{2}(e^{-\alpha_o} - e^{-\alpha_x})$. The rotation between the two coordinate systems (\underline{x}' , \underline{y}') and (\underline{x}^r , \underline{y}^r) is called Faraday rotation with $F = (\phi_o - \phi_x)/2$ being the Faraday rotation angle and the shape of the \underline{E} -field ellipse vary with position along the rocket trajectory. Calculations show that $\phi_o > \phi_x$ for all measurable quasi-longitudinal cases, so not only does \underline{E}^r rotate clockwise within the ellipse at frequency ω , but the ellipse itself rotates slowly clockwise as altitude increases, as described by the Faraday rotation.

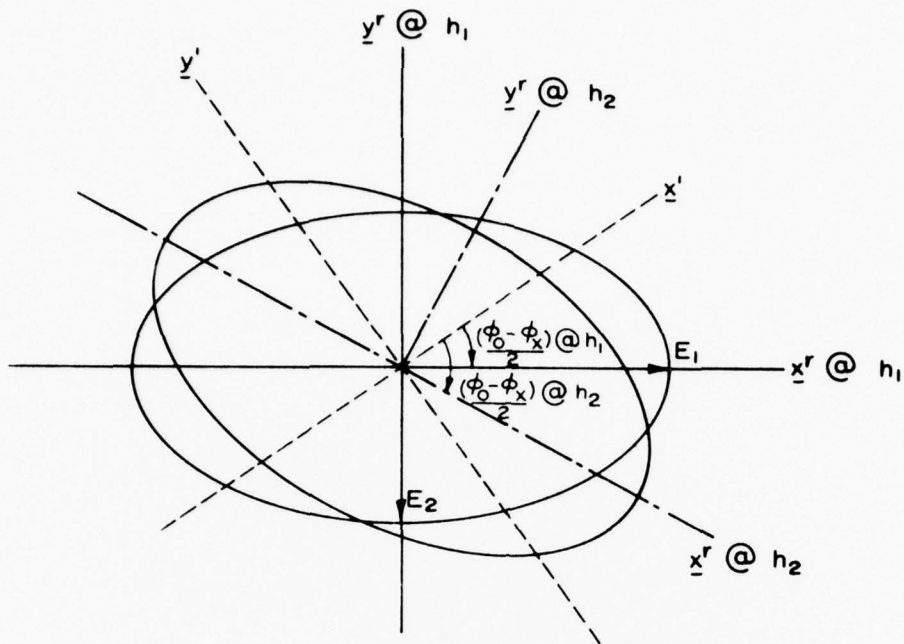


Figure 4. Relation of the \underline{x}^r , \underline{y}^r axes to the \underline{x}' , \underline{y}' axes for two different altitudes, where $h_2 > h_1$.

Differential absorption A is defined as

$$A = 20 \log_{10} \left[\frac{E_x}{E_o} \right] \quad (17)$$

In the $(\underline{x}^r, \underline{y}^r, \underline{z}^r)$ frame the electric field amplitude can be written

$$\frac{E_o}{E_x} = \frac{E_1 + E_2}{2} \quad (18a)$$

for the ordinary wave, and for the extraordinary mode

$$\frac{E_x}{E_o} = \frac{E_1 - E_2}{2} \quad (18b)$$

where

$$E_1 = \frac{M}{2} \left(e^{-\alpha_o} + e^{-\alpha_x} \right) \quad (19a)$$

$$E_2 = \frac{M}{2} \left(e^{-\alpha_o} - e^{-\alpha_x} \right) \quad (19b)$$

Substitution of (18) and (19) into (17) yields an expression for the differential absorption.

$$A = 20[\alpha_o - \alpha_x] \log_{10} e \quad (20)$$

As discussed earlier both the Faraday rotation and differential absorption (14) and (20) are independent of the initial phase and amplitude of the wave at the bottom of the ionosphere.

It is now assumed that the wave transmitter is physically near the rocket launch site, and the rocket symmetry axis \underline{z}^a which is parallel to the direction in which the rocket is initially fired, is constant over the up-leg of the rocket flight. Then \underline{z}^a and \underline{z}' are almost parallel, see Figure 2. For a rocket spinning in the same sense as the Faraday rotation, the transformation from the frame in which the rocket antenna is stationary (\underline{x}^a , \underline{y}^a , \underline{z}^a) to the electromagnetic wave frame (\underline{x}' , \underline{y}' , \underline{z}') can be represented by

$$S = \begin{bmatrix} \cos \dot{\alpha}t & -\sin \dot{\alpha}t & 0 \\ \sin \dot{\alpha}t & \cos \dot{\alpha}t & 0 \\ 0 & 0 & 1 \end{bmatrix} \quad (21)$$

where $\dot{\alpha}$ is the spin rate. The transformation from the (\underline{x}^a , \underline{y}^a , \underline{z}^a) axes to the (\underline{x}^r , \underline{y}^r , \underline{z}^r) Faraday rotation axes is given by (14) and (21)

$$T = RS = \begin{bmatrix} \cos[\dot{\alpha}t - (\phi_o - \phi_x)/2] & -\sin[\dot{\alpha}t - (\phi_o - \phi_x)/2] & 0 \\ \sin[\dot{\alpha}t - (\phi_o - \phi_x)/2] & \cos[\dot{\alpha}t - (\phi_o - \phi_x)/2] & 0 \\ 0 & 0 & 1 \end{bmatrix} \quad (22)$$

We assume the rocket antenna to be a short dipole pointing radially outward, i.e. perpendicular to the rocket axis. For other antenna configurations, this would be the direction of the equivalent dipole. Let

$$\underline{\tau}^a = \begin{bmatrix} 1 \\ 0 \\ 0 \end{bmatrix}$$

represent a unit vector in the dipole direction, i.e. \underline{x}^a is parallel to the antenna. Multiplying $\underline{\tau}^a$ on the left by T gives

$$\underline{\tau}^r = T\underline{\tau}^a = \begin{bmatrix} \cos[\dot{\alpha}t - (\phi_o - \phi_x)/2] \\ \sin[\dot{\alpha}t - (\phi_o - \phi_x)/2] \\ 0 \end{bmatrix} \quad (23)$$

which represents the rocket antenna direction in the Faraday rotation frame (\underline{x}^r , \underline{y}^r , \underline{z}^r). The relationship between the various coordinate axes is shown in Figure 5. Now that the transformations between the three principal coordinates are available, the value of the E-field in the direction of the rocketborne antenna can be found by forming the scalar product of (16) and (23):

$$\begin{aligned} E_s &= \frac{M}{2}(e^{-\alpha_o} + e^{-\alpha_x})\cos[\omega t - (\phi_o + \phi_x)/2]\cos[\dot{\alpha}t - (\phi_o - \phi_x)/2] \\ &\quad - \frac{M}{2}(e^{-\alpha_o} - e^{-\alpha_x})\sin[\omega t - (\phi_o + \phi_x)/2]\sin[\dot{\alpha}t - (\phi_o - \phi_x)/2] \end{aligned} \quad (24)$$

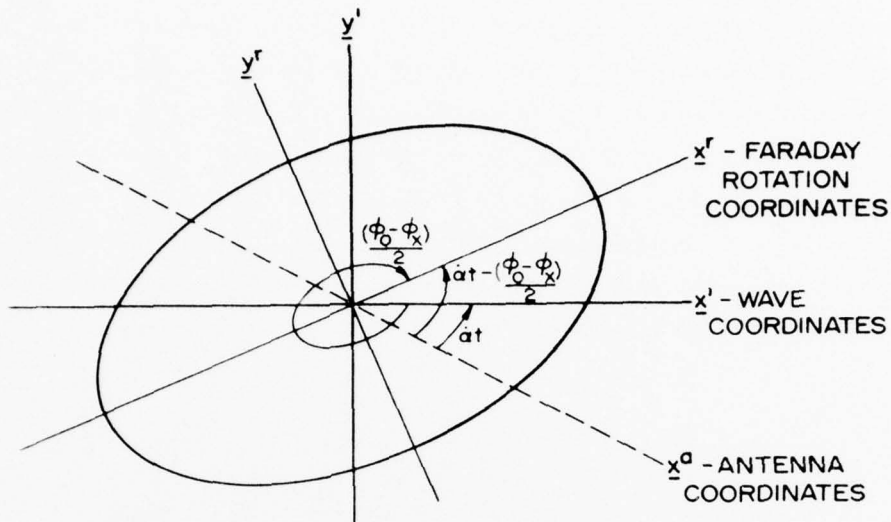


Figure 5. Relationship between coordinate axes.

The potential measured at the antenna terminals is simply

$$V_s = \int_0^l \underline{E}_s \cdot d\underline{L} \approx l E_s$$

where l is the effective electrical length of the equivalent dipole antenna. Spatial variations transverse to the directions of propagation can be neglected if we use simple horizontal dipole antennae at the transmitter. From (24) it can be noted that V_s is a scalar function of time t , spin rate $\dot{\alpha}$, and altitude z through the changes in α_o , α_x , ϕ_o , and ϕ_x with electron density and collision rate. When the altitude is held fixed, there is a rapid oscillation in V_s at frequency ω with a much slower amplitude modulation $\dot{\alpha}$. This is exactly what would be expected from a rotating dipole antenna in the field of a plane electromagnetic wave.

For a Faraday rotation-differential absorption measurement, the values of $\omega \approx 10^7 \text{ sec}^{-1}$ and $\dot{\alpha} \approx 20\pi \text{ sec}^{-1}$ might be typical. This means

that the rocket antenna does not move significantly during the period of one wave cycle. The voltage waveform at the antenna terminals then consists of a sinusoid signal of angular frequency $\omega \approx 10^7 \text{ sec}^{-1}$, with a much slower amplitude variation produced by rocket spin and Faraday rotation not exceeding 10^3 sec^{-1} . The maximum value of the induced signal voltage V_R during one cycle of the wave frequency ($\tau = 2\pi/\omega \approx 6 \times 10^{-7} \text{ sec}$) is proportional to the value of E_s when $dE_s/dt = 0$. Differentiating (24) with respect to time, but holding $\dot{\alpha}$ constant because the spin is quasi-stationary with respect to ω , gives

$$\begin{aligned} \frac{dE_s}{dt} &= -E_1 \omega \sin[\omega t - (\phi_o + \phi_x)/2] \cos[\dot{\alpha}t - (\phi_o - \phi_x)/2] \\ &\quad - E_2 \omega \cos[\omega t - (\phi_o + \phi_x)/2] \sin[\dot{\alpha}t - (\phi_o - \phi_x)/2] . \end{aligned} \quad (26)$$

Setting (26) equal to zero gives a value of $\omega t - (\phi_o + \phi_x)/2$ for which E_s is maximum, i.e.

$$[\omega t - (\phi_o + \phi_x)/2]_{\max} = -\tan^{-1} \left\{ \frac{E_2}{E_1} \tan[\dot{\alpha}t - (\phi_o + \phi_x)/2] \right\} \quad (27)$$

with

$$\begin{aligned} E_1 &= M/2(e^{-\alpha_o} + e^{-\alpha_x}) \\ E_2 &= M/2(e^{-\alpha_o} - e^{-\alpha_x}) . \end{aligned}$$

Substituting (27) into (25) yields the peak value of V_s over a wave period

$$\begin{aligned} V_R &= V_1 \left[\cos \left(\tan^{-1} \left\{ \frac{E_2}{E_1} \tan[\dot{\alpha}t - (\phi_o - \phi_x)/2] \right\} \right) \cos[\dot{\alpha}t - (\phi_o - \phi_x)/2] \right] \\ &\quad + V_2 \left[\sin \left(\tan^{-1} \left\{ \frac{E_2}{E_1} \tan[\dot{\alpha}t - (\phi_o - \phi_x)/2] \right\} \right) \sin[\dot{\alpha}t - (\phi_o - \phi_x)/2] \right] \end{aligned}$$

where $V_1 = \ell E_1$, $V_2 = \ell E_2$. Passing the instantaneous antenna voltage (25) through a detector with a time constant long compared with the wave period, the detected output voltage would be given by (28). This voltage contains the differential absorption and Faraday rotation information about the ionosphere and needs only be interpreted to evaluate the D-region electron density and collision frequency.

The differential absorption given by equations (17) through (20) requires values for E_1/E_2 . These are proportional to the maximum and minimum values of V_R which occur when the antenna is parallel to the major and minor axis of the E-field ellipse. Figure 6a illustrates the E-field polarization ellipse geometry. Since V_R is proportional to the maximum value of $(\underline{t}^r \cdot \underline{E}^r)$ over each cycle, it is seen that when the major axis of the polarization ellipse is parallel or perpendicular to the antenna the value of V_R is maximum or minimum. Another aspect of the signal is illustrated in Figure 6b where the time varying voltage is displayed. The envelope of this signal is V_R and the minimum and maximum values of V_R are V_1 and V_2 . In reality, the oscillation of V_s is much more rapid relative to oscillation of V_R . Since the shape of the polarization ellipse changes as the wave propagates through the ionosphere, the values V_2 and V_1 also change and the determination of differential absorption depends upon their evaluation. Faraday rotation is also obtained from the voltage of Figure 6b, but it is more easily understood after several graphs are developed in Chapter III.

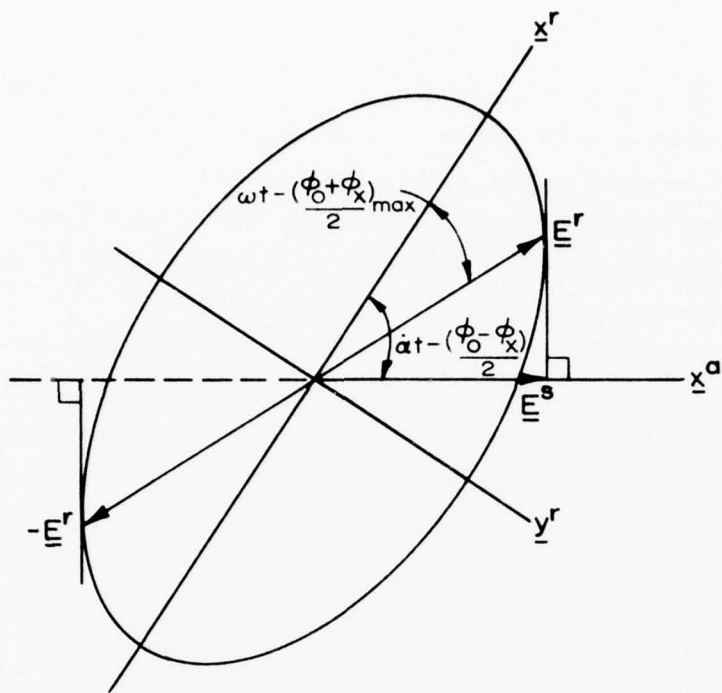


Figure 6a. Projection of \underline{E}^r onto antenna at $V_s = V_R$ for a typical antenna position relative to the \underline{E} -field ellipse.

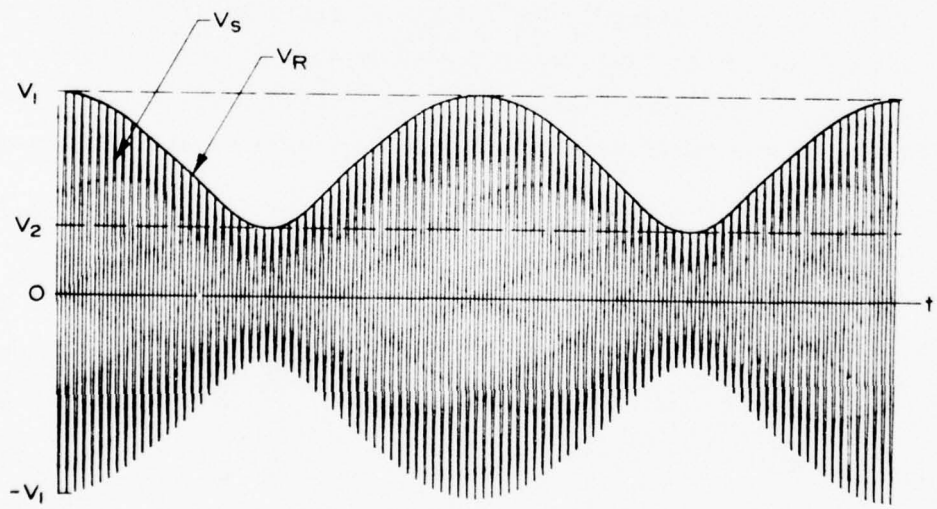


Figure 6b. V_s and V_R as functions of time, shown for the time of one rotation of the antenna.

CHAPTER III SELECTION OF FREQUENCIES

In this chapter we use the theory of Chapter II to develop a scheme for selecting wave frequencies that will yield optimum results from a D-region Faraday rotation - differential absorption experiment. A computer program was developed to calculate numerically the radio wave signal that would be detected at a rocket vehicle traveling through the ionosphere on a given trajectory. A model ionosphere of the electron density and electron-neutral collision rate is required to calculate wave propagation. Profiles used for illustration were chosen to bracket extreme conditions that might be found in the polar D-region. Electron density profiles for "quiet" and "disturbed" conditions were measured during PCA events and are shown in Figure 7. These conditions are not unique to, but may be typical of rather severe PCA. Collision frequency versus altitude is plotted in Figure 8. The winter profile of collision rate is a moderate estimate that might be expected over the winter months. At high latitudes, the summer season and possibly other factors can lead to large variations in the collision frequency profile, as commented upon by Thrane *et al.*, [1966] and Belrose *et al.*, [1966]. We have chosen a high collision rate of three times the lower curve to bracket the possible values.

The profiles of disturbed D-region electron density and winter collision rate were used to calculate a rocket antenna signal. Figure 9 illustrates a 0.5 second segment of V_R (equation 28) each 5 km altitude for a wave frequency of 7 MHz. The wave at the bottom of the ionosphere was assumed to be linearly polarized, so that the minimum value of V_R (V_2 in Figure 6b) is essentially zero at 50 km. As the wave propagates higher into the ionosphere, the polarization ellipse gets "fatter" with the result that the minimum value of V_R gets larger, as illustrated in Figure 9b and 9c. Similar curves for 20 MHz are plotted in Figure 10. The higher frequency, 20 MHz, is less effected by the ionosphere than the 7 MHz signal. Since differential absorption depends upon the largest and smallest values of V_R , Figures 9 and 10 illustrate how differential

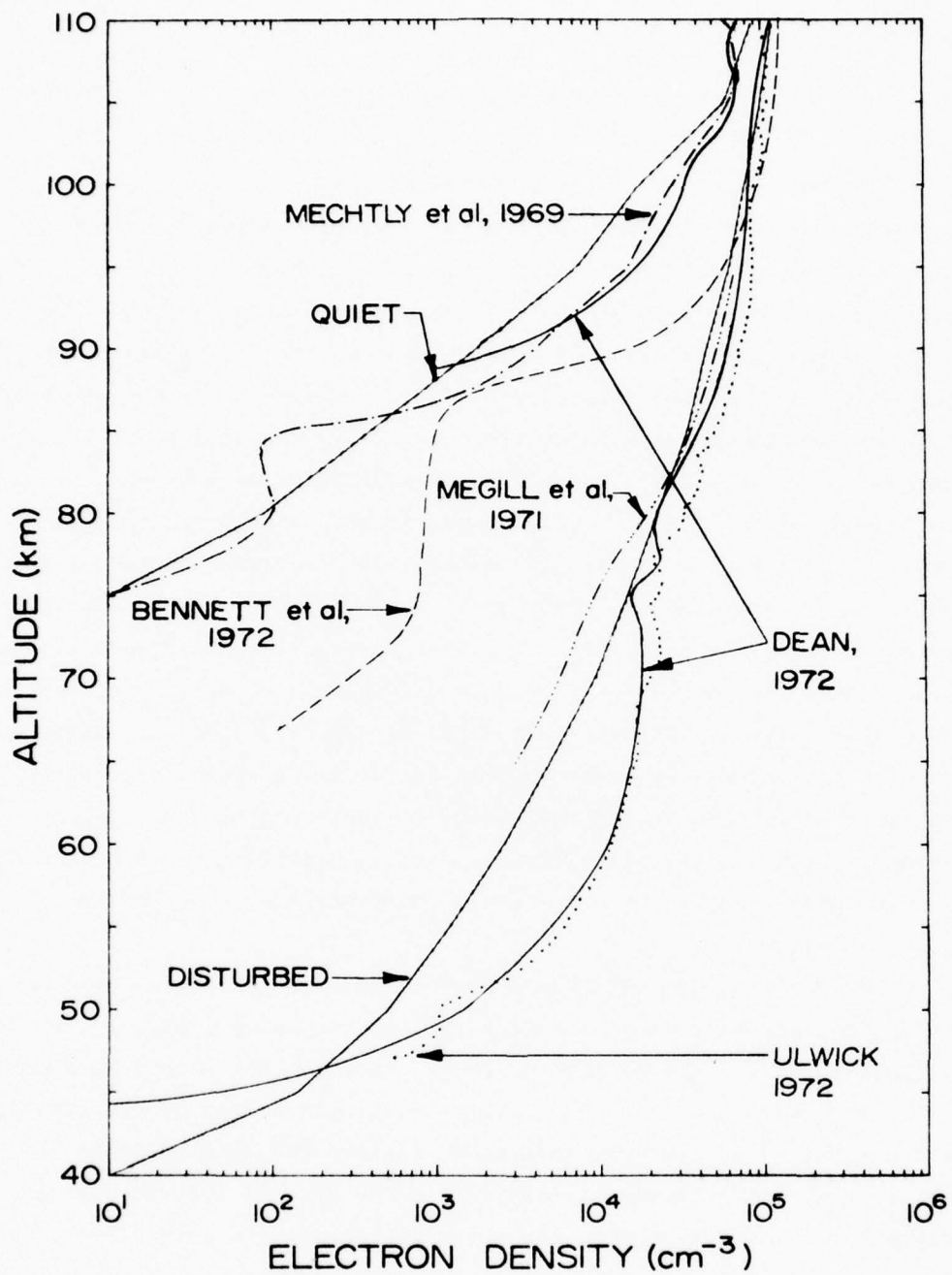


Figure 7. Electron density profiles. The profiles labeled 'QUIET' and 'DISTURBED' were chosen by the authors to bracket a wide range of possible conditions.

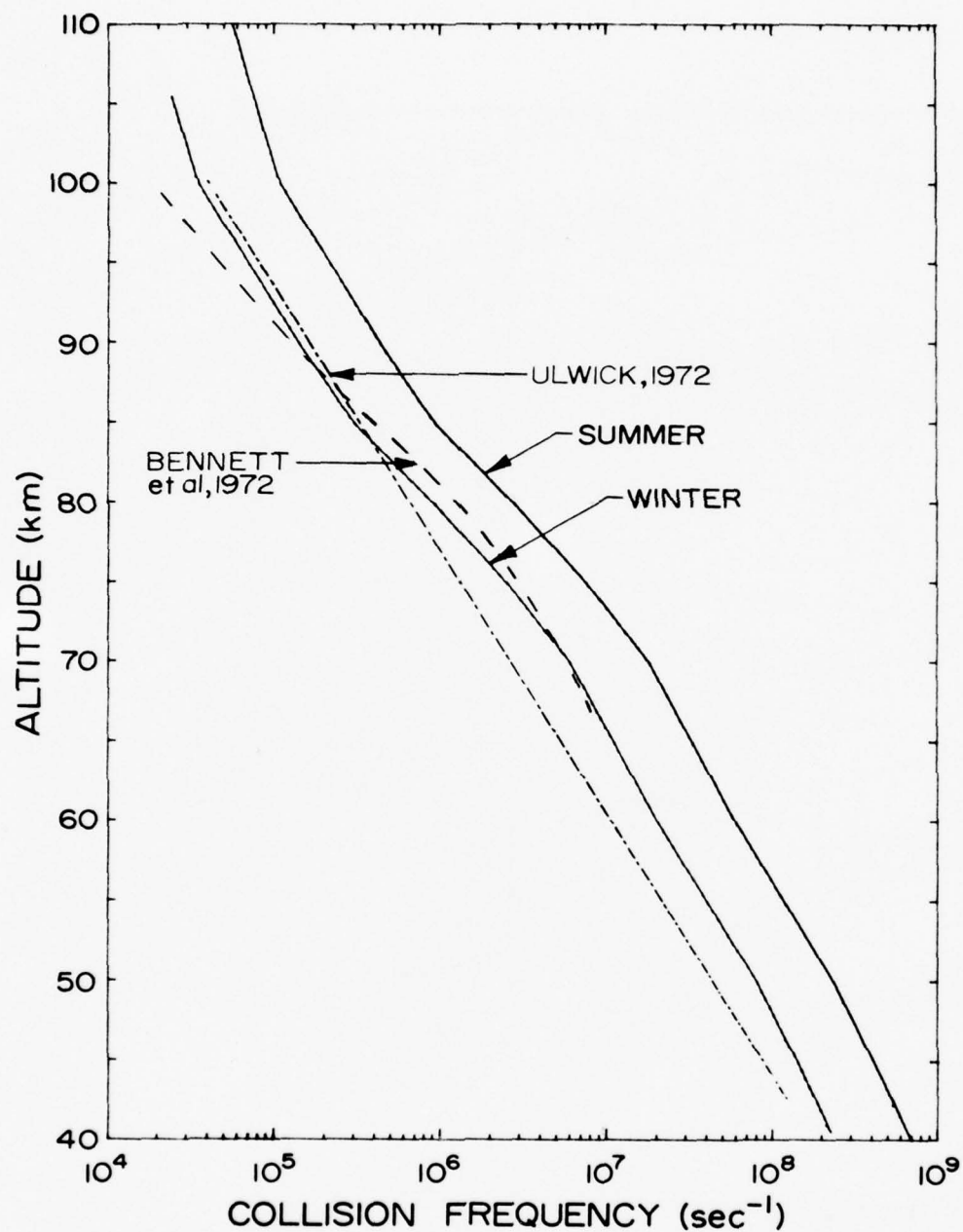


Figure 8. Electron-neutral collision frequency profiles. The profile labeled 'WINTER' was chosen as a moderate example by the authors. The 'SUMMER' profile was chosen to account for seasonal and other possible effects (see text).

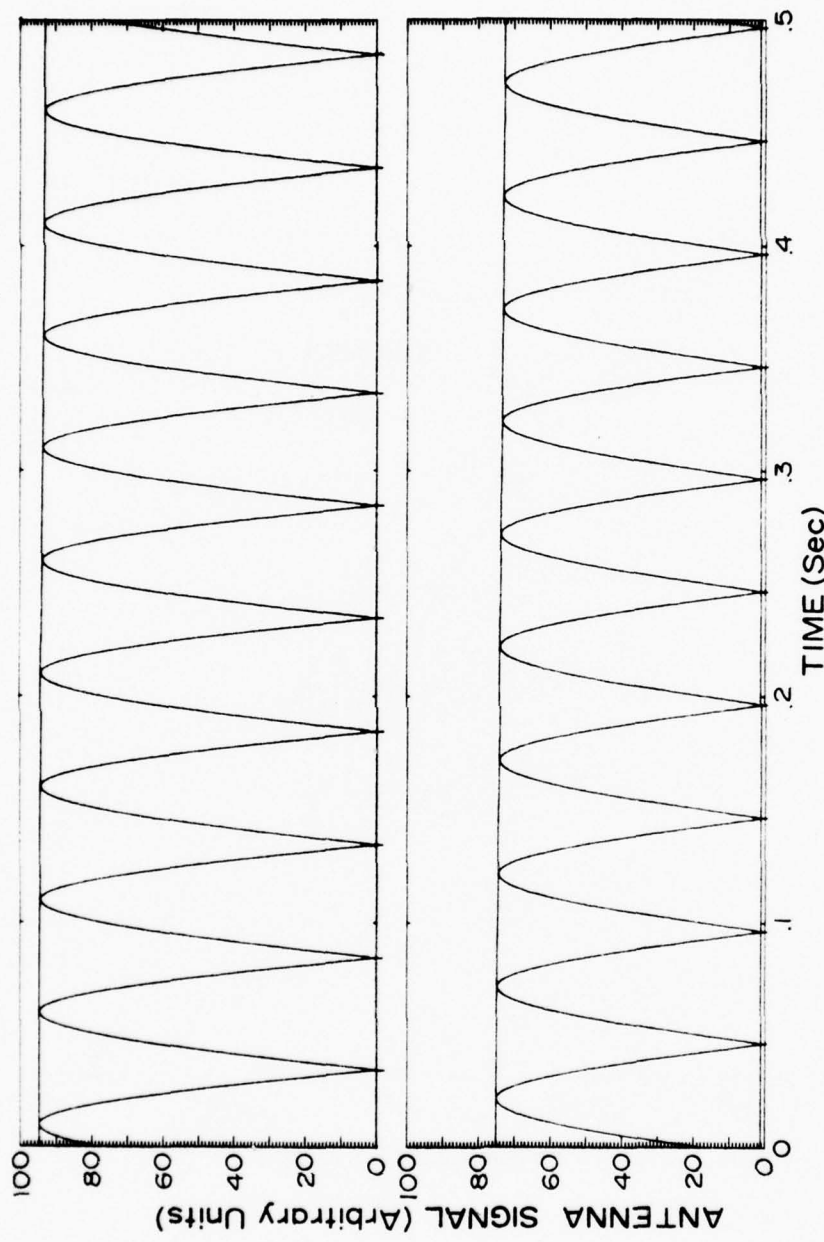


Figure 9a. 7 MHz signal for disturbed electron density and winter collision frequency profiles for rocket altitudes of 50 km (top) and 55 km (bottom).

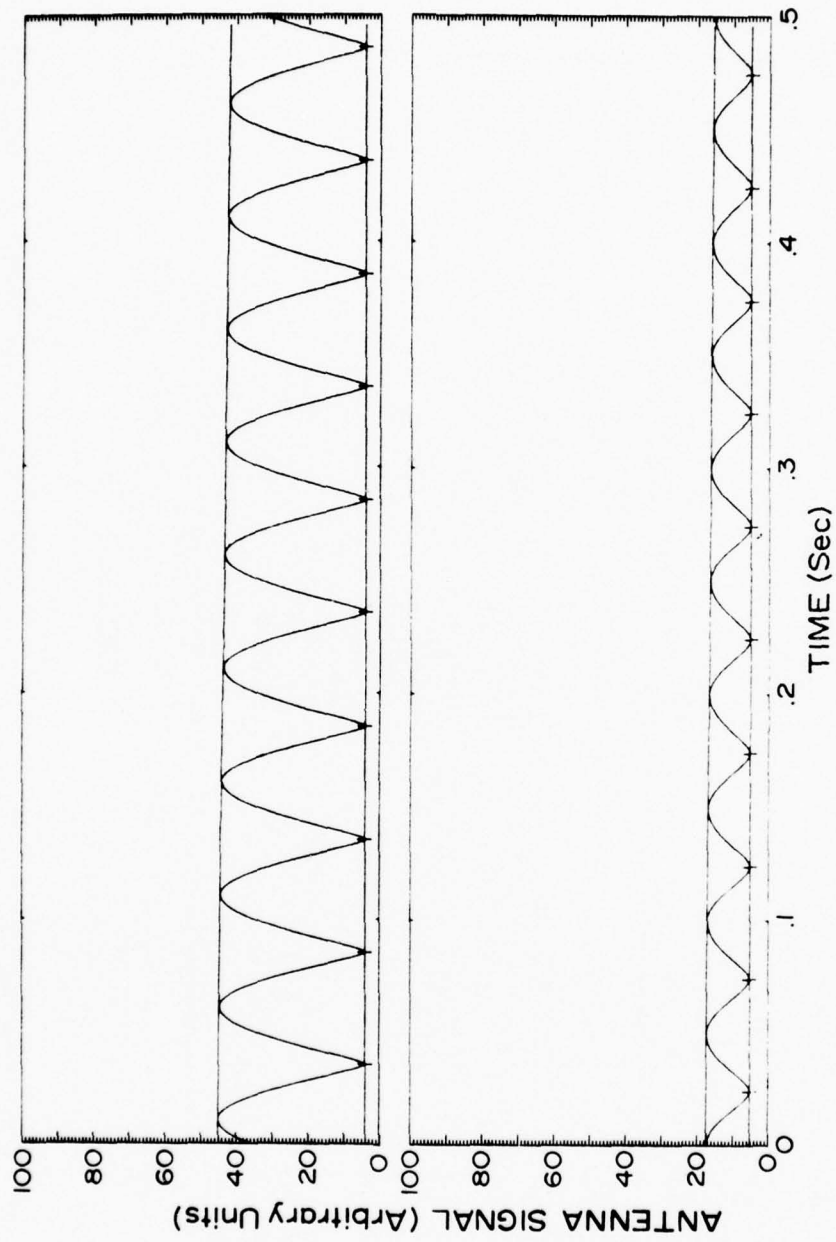


Figure 9b. 7 MHz signal for disturbed electron density and winter collision frequency profiles for rocket altitudes of 60 km (top) and 65 km (bottom).

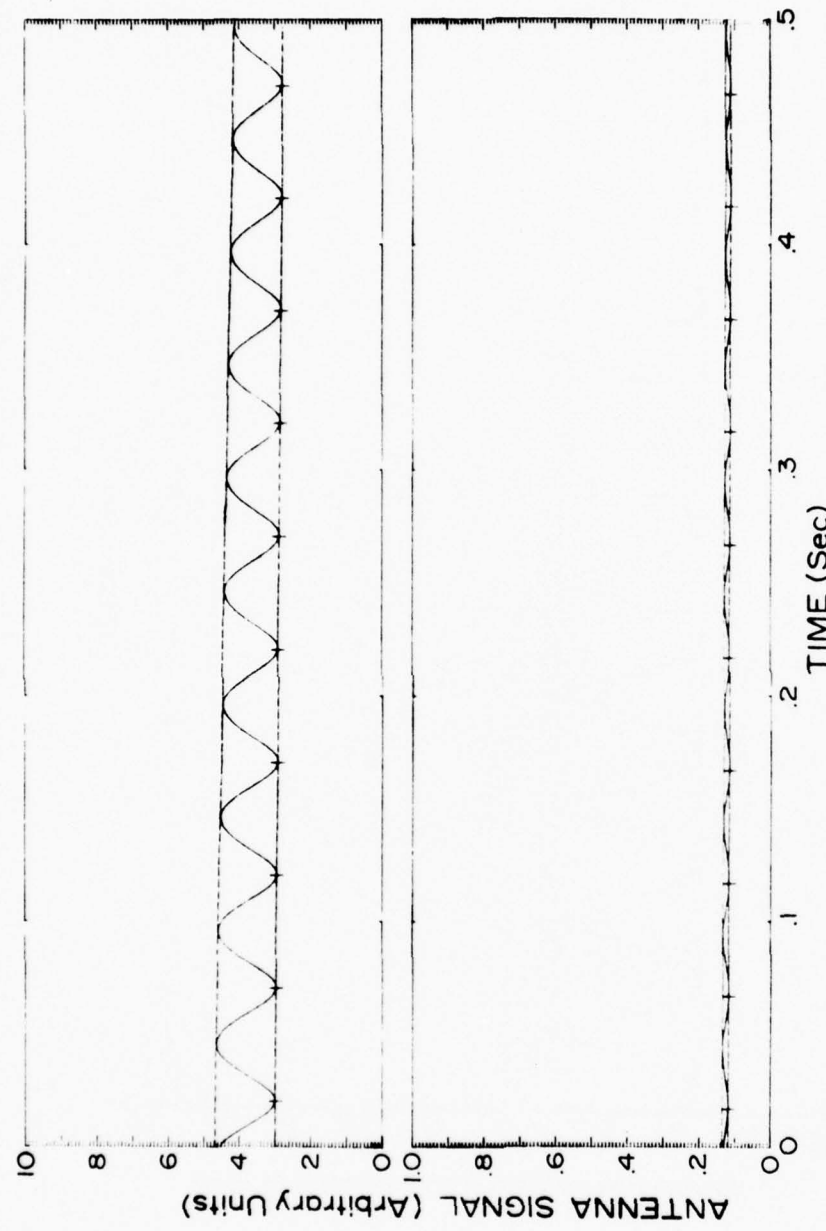


Figure 9c. 7 MHz signal for disturbed electron density and winter collision frequency profiles for rocket altitudes of 70 km (top) and 75 km (bottom). Note the potential scales have been multiplied by factors of 0.1 and 0.01.

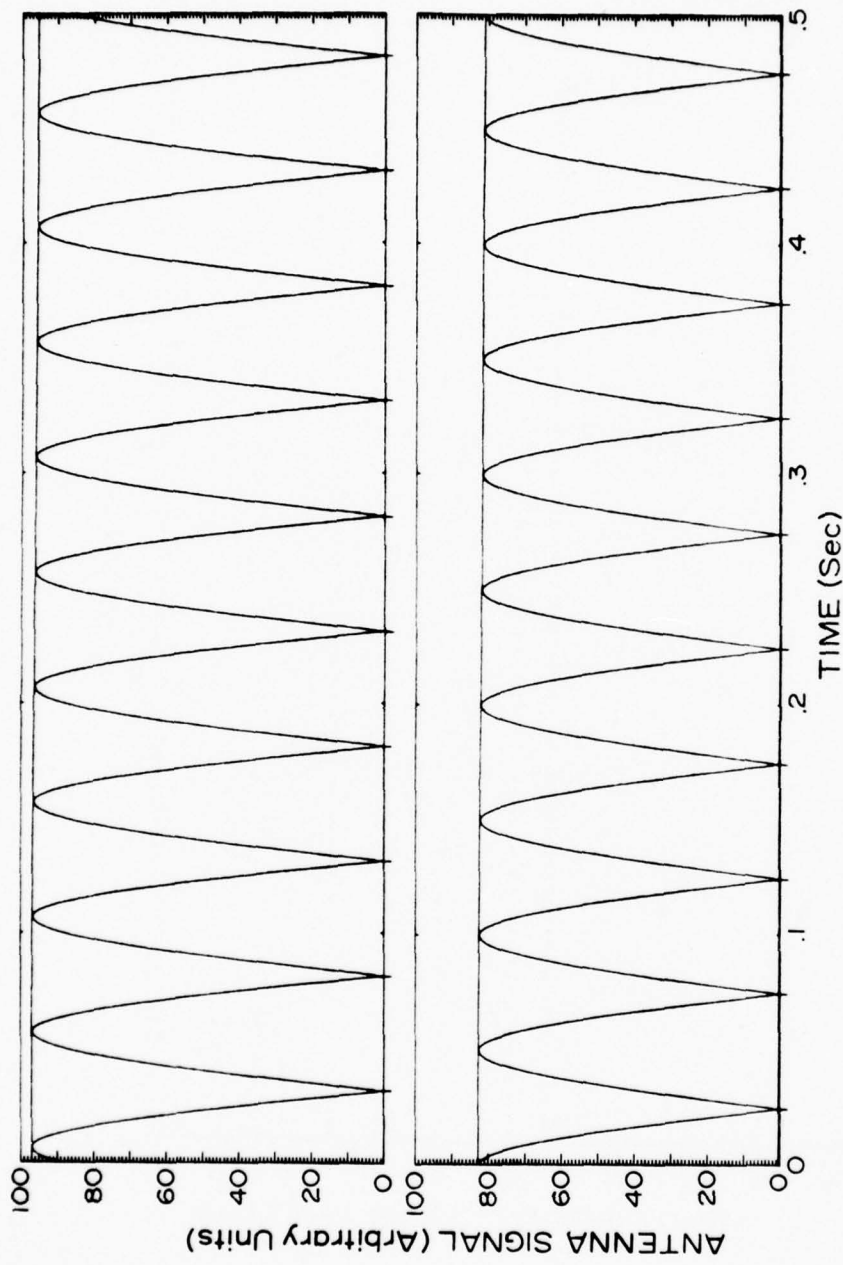


Figure 10a. 20 MHz signal for disturbed electron density and winter collision frequency profiles for rocket altitudes of 50 km (top) and 55 km (bottom).

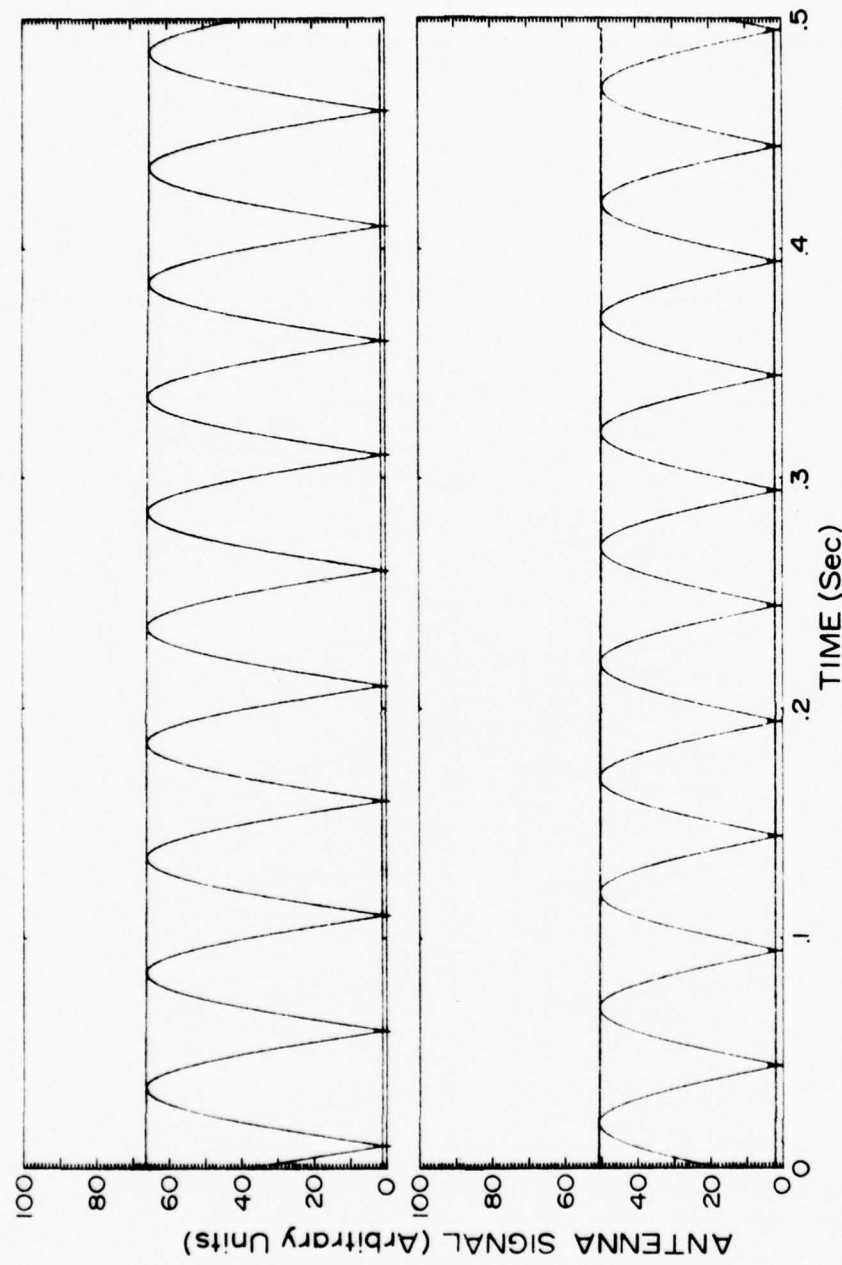


Figure 10b. 20 MHz signal for disturbed electron density and winter collision frequency profiles for rocket altitudes of 60 km (top) and 65 km (bottom).

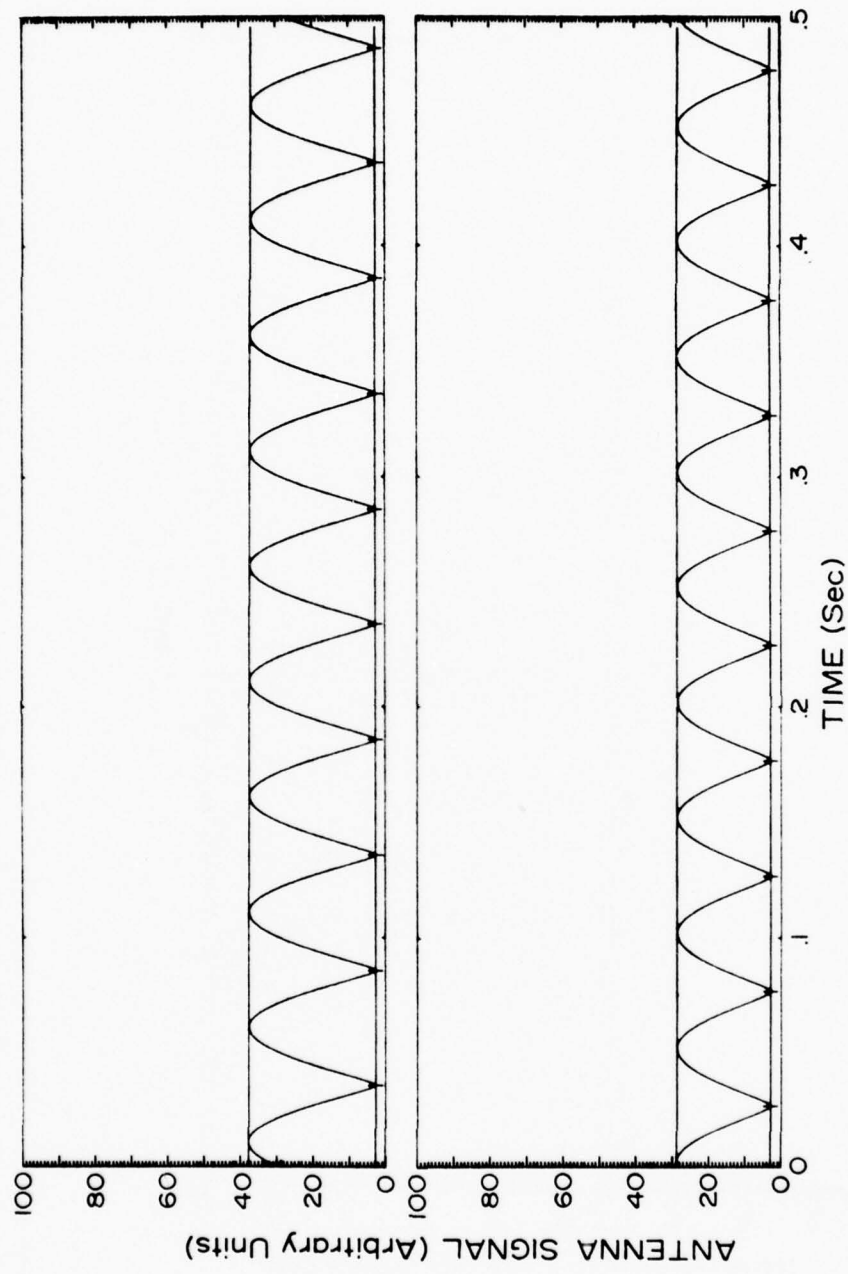


Figure 10c. 20 MHz signal for disturbed electron density and winter collision frequency profiles for rocket altitudes of 70 km (top) and 75 km (bottom).

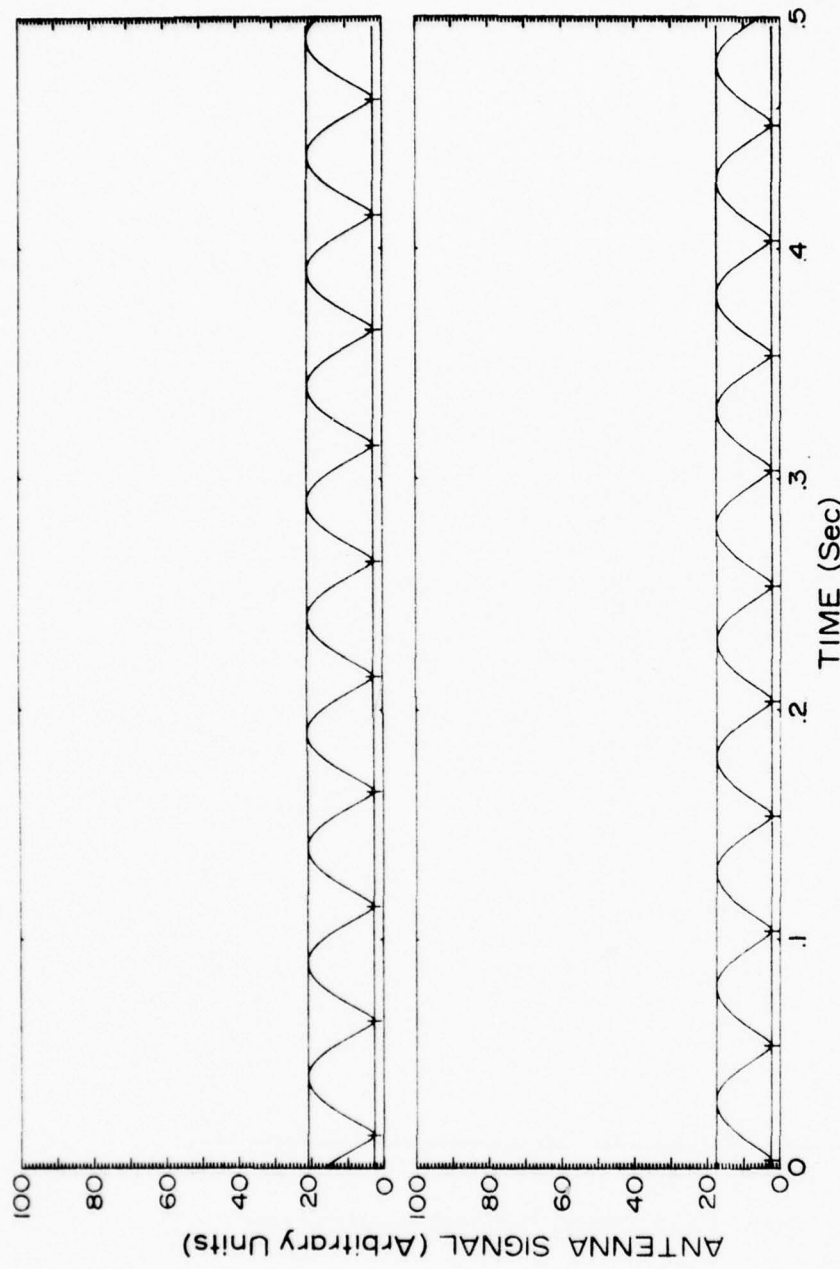


Figure 10d. 20 MHz signal for disturbed electron density and winter collision frequency profiles for rocket altitudes of 85 km (top) and 95 km (bottom).

absorption may be extracted from the telemetry data. The lowest altitude at which differential absorption can be measured is the lowest altitude where V_R can be identified to be at its minimum values. This measurement is limited by noise, as discussed latter.

The voltage V_R given by equation (28) is composed of two terms; each term is a periodic function of the "spin" argument $[\dot{\alpha}t - (\phi_o - \phi_x)/2]$. The maximum values of V_R occur at $[\dot{\alpha}t - (\phi_o - \phi_x)/2] = n\pi$ and minimum values at $[\dot{\alpha}t - (\phi_o - \phi_x)/2] = (n + 1/2)\pi$, where n is an integer. The Faraday rotation $[(\phi_o - \phi_x)/2]$ can be deduced from the periodicity of V_R , if $\dot{\alpha}$ is known. If $(\phi_o - \phi_x)/2$ were constant over a number of cycles of $\dot{\alpha}t$, then V_R would obtain its minimum value V_2 every $t = \pi/\dot{\alpha}$ seconds corresponding to a half rotation of the rocket. On the other hand, if $(\phi_o - \phi_x)/2$ varies slightly during each period, then the minimum value V_2 would be slightly displaced in time from a regular period. A rocket spin rate of 10 rps ($20/\pi$ rad/sec) was used in calculating the data of Figures 9 and 10. Tick marks every half spin revolution are marked on the lower boundary. These marks coincide with the antenna lying parallel to the magnetic meridian plane. It can be seen that the signal minima and the tick marks shift apart as the wave propagates upward. A measure of this separation determines the Faraday rotation. In an actual experiment, the rocket spin rate must be resolved by an independent measurement such as an on-board magnetometer. The spin rate data can then be used to help recover the Faraday rotation rate.

Radio interference at frequencies of interest for a rocket experiment comes from other radio frequency transmissions, from atmospheric and cosmic noise, and from receiver and telemetry equipment. Figure 11 shows the relative magnitude of some of these noise sources. The root mean square electric field corresponding to a given noise power is proportional to an equivalent antenna noise temperature T_A and bandwidth B by the relationship

$$E_A = [120\pi B k T_A]^{1/2} \quad (\text{volts/meter})$$

where k is Boltzmann's Constant (1.38×10^{-23} watt-sec/K). On the basis of (29) we can talk about the equivalence of noise temperature and noise power.

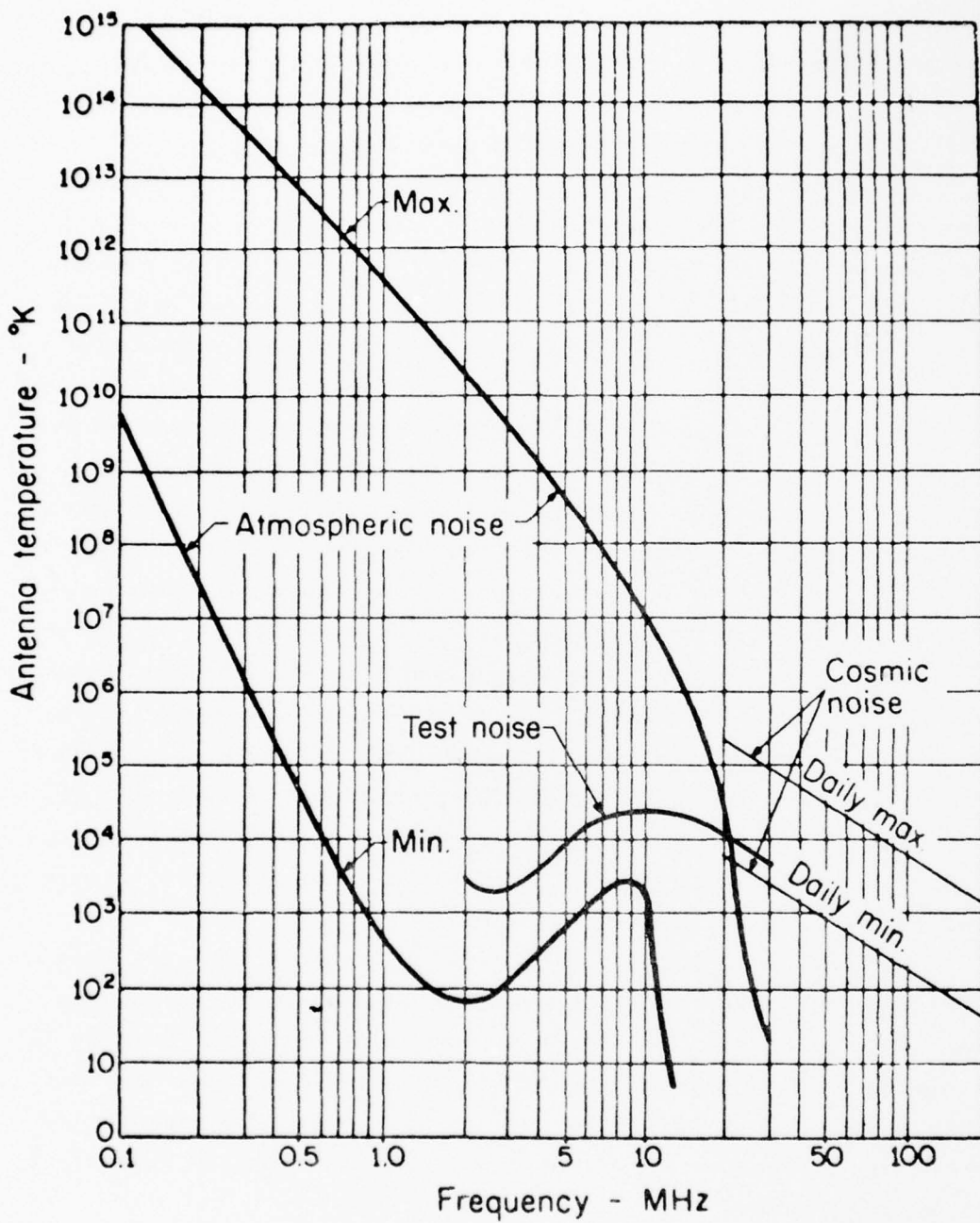


Figure 11. Noise temperature at medium and high frequencies [Jordan and Balmain, 1968]. Curve labeled 'Test noise' was selected by authors for all computations involving T_A .

One other important factor in receiver design is the exclusion of unwanted radiofrequency transmissions [Ginther and Smith, 1975]. A foreknowledge of transmissions at the experiment site allows one to select frequencies close to those listed above, but with a minimum of interference. Such a choice together with a narrow receiver bandwidth minimizes the error from this source. Some serious consideration should be given to this possible source of noise pollution before the experiment parameters are firmly fixed.

The total noise can be represented as an equivalent electric field and can be written as the sum of noise generated outside the rocket, signal degradation by the telemetry system and receiver generated noise

$$E_N = E_A + S_R E_{R_1} + E_{REC} \quad (30)$$

In the 1-30 MHz region, a good receiver has a noise figure of about 3 dB, which means the receiver equivalent noise temperature is only twice that of an ideal noiseless receiver. This means that the receiver noise can generally be neglected compared to the other noise sources. Telemetry noise is expressed as a small fraction S_R of the full-scale signal E_{R_1} ; the full-scale voltage recorded on the lowest gain range of the receiver. A good telemetry system will have a value of S_R around 0.01. The receiver system should be designed so that the telemetry error is approximately the same order of magnitude as the other noise sources. If $S_R E_{R_1} \gg E_A$, then the telemetry degradation is unnecessarily large while if $E_A \gg S_R E_{R_1}$ the receiver may be unnecessarily expensive. Assuming that

$$S_R E_{R_1} \approx E_A \quad (31)$$

the noise equivalent electric field is approximately

$$E_N \approx 2E_A .$$

If we ignore signals that are less than 10 dB above the noise level,

the minimum signal E_2 that would yield accurate data is

$$E_2 = 2\sqrt{10} E_A . \quad (32)$$

In terms of ground-based transmitter power P_T , transmitter antenna gain G_T and the absorption indices, (32) becomes

$$\left[\frac{e^{-\alpha_o(h_m)} - e^{-\alpha_x(h_m)}}{2} \right] = 2\sqrt{10} E_A R_m (30 P_T G_T)^{-\frac{1}{2}} \quad (33)$$

where h_m is the lowest altitude at which condition (32) is satisfied and R_m is the distance from the transmitter to the rocket receiver. This minimum altitude will obviously depend on transmitted power. Thus, the stronger the transmitted signal the lower the altitude and electron density that can be measured by differential absorption.

The maximum received signal is proportional to E_1 , equation (19). At the altitude where (33) is valid E_1 can be written

$$E_1(h_m) = (30 P_T G_T)^{\frac{1}{2}} \left[\frac{e^{-\alpha_o(h_m)} + e^{-\alpha_x(h_m)}}{2} \right] R_m^{-1} \quad (34)$$

The difference between E_1 and E_2 at h_m is several orders of magnitude. Therefore, it is necessary to incorporate an automatic gain switching capability into the rocketborne receiver in order to measure linearly this large variation in signal strength. This means that several ranges, each having a different value of gain, must be used. If each range has an impedance separating it by 15 dB from the next highest range, then the k^{th} range can measure a field strength of

$$E_{RK} = 10^{3(k-1)/4} E_{R_1}$$

The range that measures the largest voltages has the lowest gain and must measure $E_1(h_m)$ linearly. For $S_R = 0.01$, $E_{R_1} = E_A / 0.01$ and this implies that the largest value of k is the integer κ given by

$$\kappa \geq \frac{4}{3} \log_{10} \left[\frac{E_1(h_m)}{E_A} \right] - 1.667 \quad (35)$$

Thus κ is the number of ranges separated by 15 dB necessary to measure $E_1(h_m)$ linearly.

The necessary criteria to estimate the lowest altitude at which differential absorption measurements can be made are now available. Some compromise will probably be necessary in the choice of transmitted power, number of receiver ranges, etc., but there is enough flexibility to satisfy most investigations.

There also exists a practical upper altitude limit for measurement of differential absorption. This limit arises from the progressively decreasing separation between signal maxima and signal minima, E_1 and E_2 . Figure 9c illustrates the antenna voltage at an altitude where the extraordinary wave has been almost completely absorbed. At some altitude h_z , E_1 and E_2 will become indistinguishable due to noise fluctuations. For the D-region the ordinary wave component is usually so large that the signal must be measured in one of the middle ranges of the receiver. Here the noise is caused primarily by telemetry degradation. Thus

$$E_N = S_R E_{Rk} = S_R 10^{3(k-1)/4} E_{R_1}$$

If we require $E_1 - E_2$ to be 10 dB above the noise, then

$$E_1(h_z) - E_2(h_z) \geq 10^{\frac{1}{2}} E_N$$

Since $E_{Rk} \geq E_1(h_z)$ and $10^{3/4} E_1(h_z) \geq E_{Rk} = E_N/S_R$, the highest altitude at which differential absorption may conservatively be evaluated is

$$E_1(h_z) - E_2(h_z) \geq 10^{\frac{1}{2}} S_R \left[10^{3/4} E_1(h_z) \right] \geq \left[10^{\frac{1}{2}} S_R - E_N/S_R \right]$$

By substituting $E_2 = E_o - E_x$ and $E_1 = E_o + E_x$ in the above equation, the

following expression results

$$2E_x(h_z) \geq 10^{1.25} S_R [E_o(h_z) + E_x(h_z)]$$

which can be rearranged to give

$$20 \log_{10} \left(\frac{E_x(h_z)}{E_o(h_z)} \right) \geq 20 \log_{10} \left(\frac{S_R}{0.112 - S_R} \right) \approx -20.2 \text{ dB} \quad (36)$$

if $S_R = 0.01$. Equation (36) provides a means to determine the approximate altitude where the differential absorption becomes too small for measurement. Equation (20) was integrated numerically for the conditions of Figure 9. The resulting differential absorption is shown in Figure 12. The lowest altitude at which differential absorption can be measured, the condition of (33), was computed for several different values of T_A . Decreasing transmitter power or increasing the bandwidth by an order of magnitude will have the same effect on the lower limit for differential absorption as increasing the antenna temperature by an order of magnitude. Based on the recommendation of Westlund (Chapter IV), values of $P_T = 200$ watts and $G_T = 3.5$ were chosen for this example. A bandwidth of 2 Khz was chosen for this illustration. For a median value of noise $T_A = 2 \times 10^4 \text{ K}^\circ$, see Figure 11, $E_A = 0.97 \times 10^{-6} \text{ V/m}$. The minimum height for differential absorption measurements is calculated to be $h_m \approx 48.1 \text{ km}$; the maximum electric field at this altitude is $E_1(h_m) \approx 6.5 \times 10^{-3} \text{ V/m}$. Therefore, the minimum and maximum antenna voltages, V_2 and V_1 , differ by three orders of magnitude. From (31) $E_R \approx 1 \times 10^{-4} \text{ V/m}$, and condition (35) specifies 4 receiver ranges. The full scale equivalent electric field strength for each receiver range and the equivalent telemetry noise are given in Table I.

The -20.2 dB limit of (36) occurs at 72.9 km, Figure 12. Above this altitude the rate of change of the differential absorption is masked by the telemetry uncertainty. At 72.9 km, $E_1(h_z) - E_2(h_z) \approx 0.4 \times 10^{-3} \text{ V/m}$ which would be measured in the third range. Table I indicates that the telemetry error is a factor of 10 larger than atmospheric noise in this receiver range.

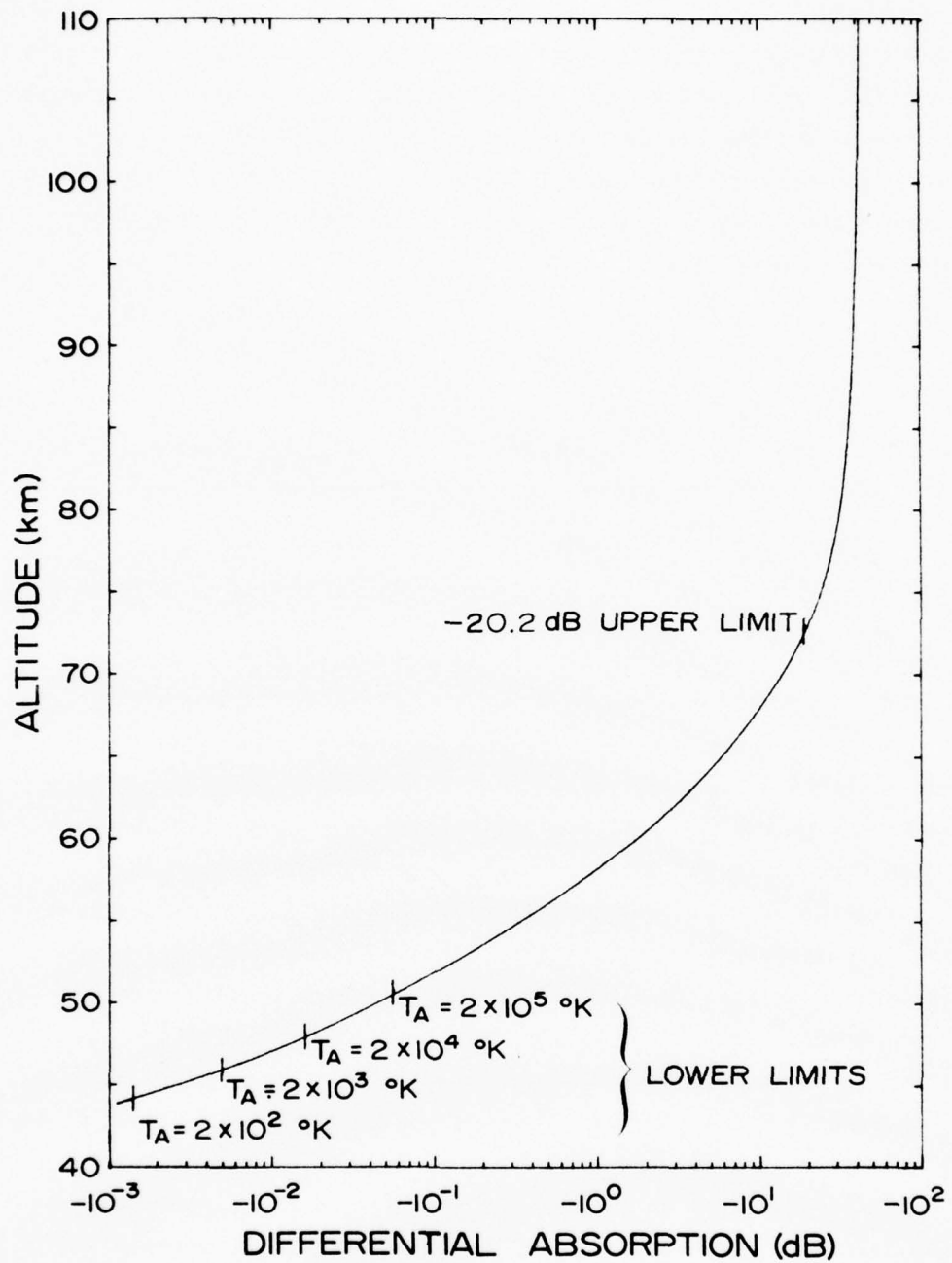


Figure 12. Differential absorption profile for a 7 MHz wave, the trajectory of Figure 2, and the winter collision frequency and disturbed electron density profiles of Figures 7 and 8.

Curves similar to that of Figure 12 can be calculated for a variety of frequencies. The limitations on differential absorption measurements can be imposed and the set of curves used to predict appropriate frequencies which will give good results and cover the desired altitudes. These curves are based of course on certain expected electron density and collision rate profiles.

TABLE I

k	E_{Rk} (mV/m)	$S_R E_{Rk}$ (μ V/m)
1	.1	1
2	.562	5.62
3	3.16	31.6
4	17.8	178

The limitations associated with determination of electron density by measurement of Faraday rotation are partly due to the differential absorption phenomenon and partly due to telemetry bandwidth. The highest altitude of measurement is reached when the extraordinary wave is completely absorbed. This limit is then the same as the differential absorption limit. The lowest altitude at which Faraday rotation can be measured is determined by the ability to detect a shift in the signal null position from the spin null position. Limiting the receiver bandwidth also limits the ability to distinguish the precise time of the signal nulls. A 1° resolution was achieved by Knoebel and Skaperdas [1966]. This value will be adopted for our determination of Faraday rotation. We note that the width of the Faraday rotation minimum increases as the separation between signal maxima and minima decreases, i.e. with increasing altitude. At the lowest altitudes the minima are reasonably sharp and will permit Faraday rotation measurements to be sensitive, even though the rate of change of the phase is not very large.

Actually, the magnetoionic theory of wave propagation is very sensitive to the assumed dependence of electron collision frequency on the

electron velocity. The Appleton-Hartree equations assume the collision frequency to be independent of electron energy while the Sen-Wyller equations assume the collision frequency to be directly proportional to electron energy. Adams [1971] has shown that neither theory is accurate below an altitude where the collision frequency v_m is greater than 1.2 times the wave frequency. This limitation was based on the comparison of electron density profiles deduced from Faraday rotation measurements and from model calculations.

The Faraday rotation for the wave propagation illustrated in Figures 9 and 12 is plotted in Figure 13. The altitude where $v_m = 1.2f$ is denoted Z_V and occurs at 67.2 km. The altitude that corresponds to a 1° resolution in the Faraday rotation is well below 67.2 km. This means that Faraday rotation data could be distinguished to lower altitudes, but unfortunately interpretation of the data is not straightforward. For the 7 MHz signal under consideration, the rotation data is only good between 67.2 km and 72.9 km.

A discussion of the returns in data by increasing the transmitted power is now in order. Consider the preceding example, where it has been determined that differential absorption data down to about 46 km can be secured. Multiplying the transmitted power P_T by a factor of 10 to 2 Kw would have the following effects. From (35) an extra 15 dB range would be necessary since $E_1(h_m)$ has been multiplied by a factor of about 4 (see (34)). The minimum signal V_2 drops off quickly at these low altitudes. The effect on h_m determined by (33) would be equivalent to lowering T_A by an order of magnitude (see Figure 12). Thus h_m would be about 2 km lower. Barring the influence of large man-made radio frequency transmissions, there wouldn't be any gains in differential absorption information at higher altitudes, or Faraday rotation throughout the medium.

At the altitudes where both Faraday rotation and differential absorption data are available, it is possible to determine electron density and the electron-neutral collision rate. Below this common altitude region, differential absorption data are still available but independent electron density and collision frequency determinations are not possible. The collision frequency is generally thought to be the most predictable

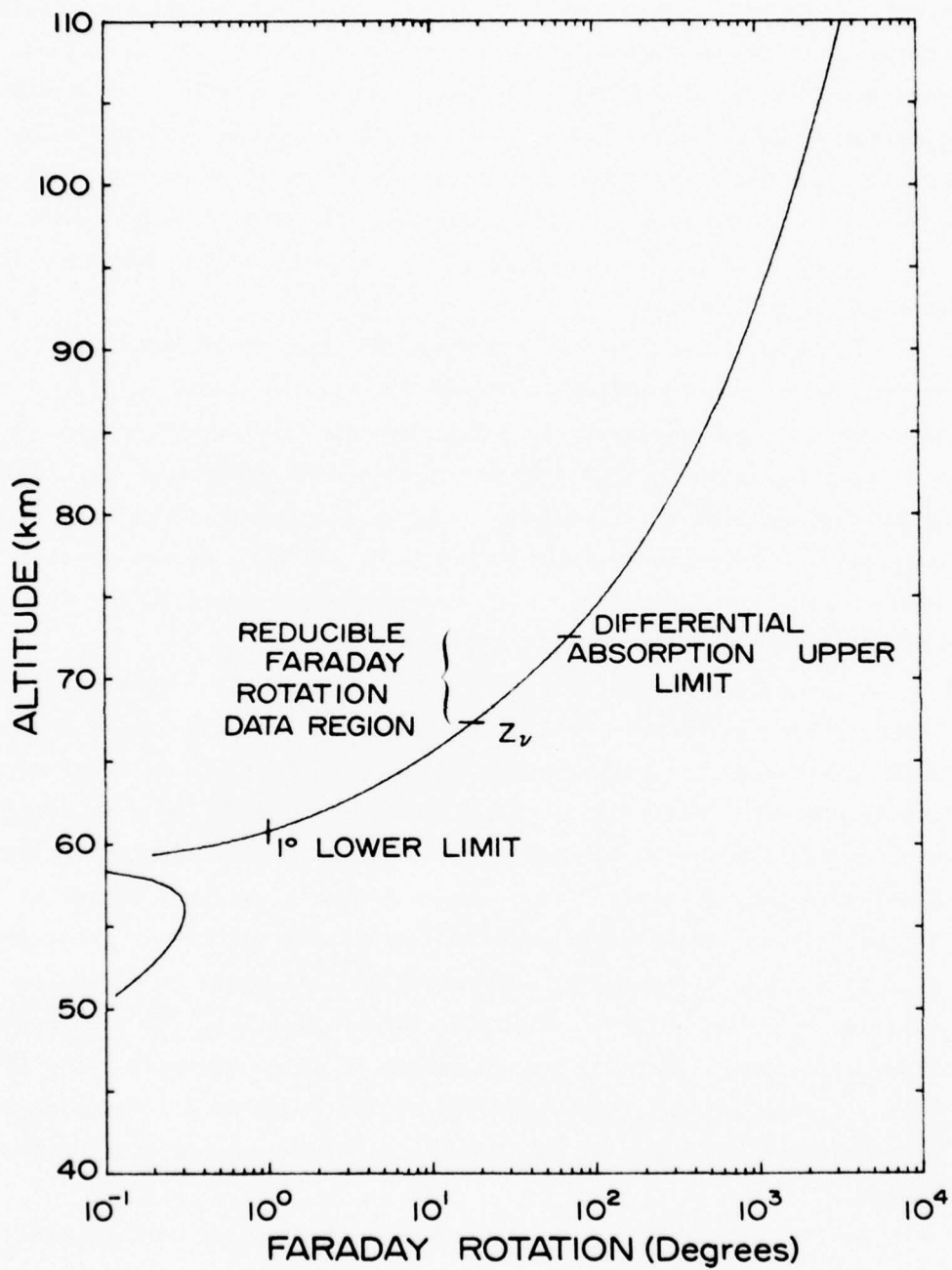


Figure 13. Faraday rotation profile for a 7 MHz wave for the same conditions as that of Figure 12.

quantity and so is often extrapolated to lower altitudes in order to determine electron densities. The procedure of extrapolating the collision rate to lower altitudes by assuming a particular pressure variation with altitude *Pack and Phelps*, [1961] is described in detail by *Thrane and Piggott*, [1966] and *Dickenson et al.*, [1976].

The remainder of this chapter will deal with the selection of a set of frequencies to probe the D-region under the extreme conditions that are found in the polar zone. Sets of curves corresponding to the values of electron density and collision frequency shown in Figures 7 and 8 have been developed. A set of curves of differential absorption and Faraday rotation for frequencies between 3.25 and 25 MHz have been calculated based on the disturbed D-region electron density and winter v_m profiles. These are plotted in Figures 14 and 15. Frequencies below 3.25 MHz were not considered in this report because it was felt that antenna construction would become too costly. One of the goals of this study was to develop an experiment which would be cheap and portable, and hence would not require great towers for the transmitter antenna (see Chapter IV). The 3.25 MHz frequency should not be considered a limitation since our computer code can generate Faraday rotation and differential absorption curves for any frequency of interest. Noise depends on the time of day, weather, season of year, and geographical location. As a compromise, the curve called "test noise" in Figure 11 was used to compute the lower altitude limit for differential absorption measurement.

The magnitude of differential absorption steadily increases with increasing altitude in Figure 14. This corresponds to the absorption of the extraordinary mode. The absorption quantities actually determined from the raw radio wave data are the maximum and minimum signal strengths, or the modulation envelope. The rate of change in the signal strength data, from which dA/dz is indirectly obtained, is dependent upon the rate of attenuation of the extraordinary mode. This can be visualized as the rate of change of the signal envelope relative to the maximum signal (see Figures 9 and 10). Although dF/dz becomes larger with altitude, the decreasing change in the signal envelope width relative to the maximum signal implies that the values of dA/dz decrease in accuracy with

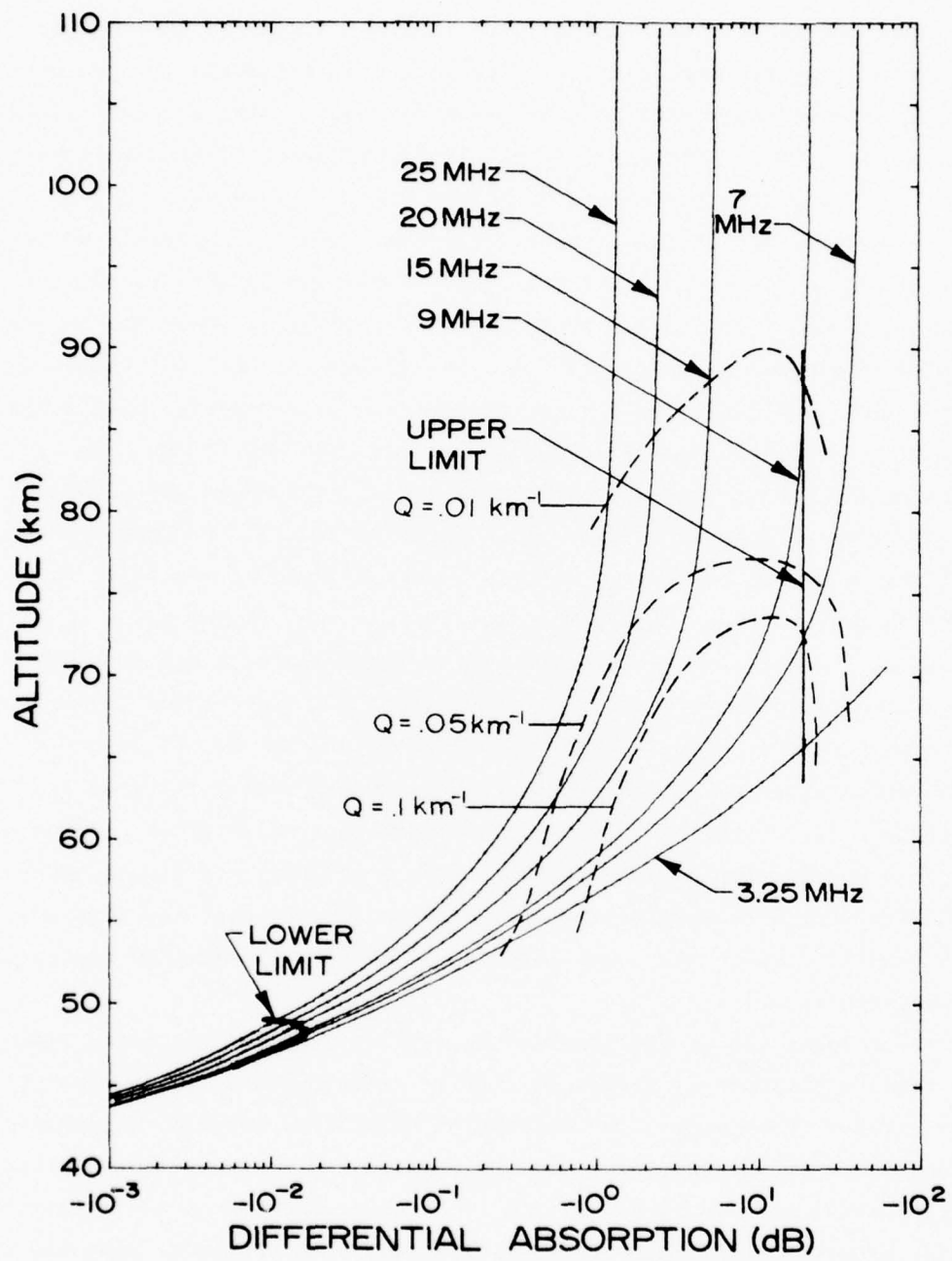


Figure 14. Differential absorption profiles for the disturbed electron density and winter collision frequency profiles of Figures 7 and 8.

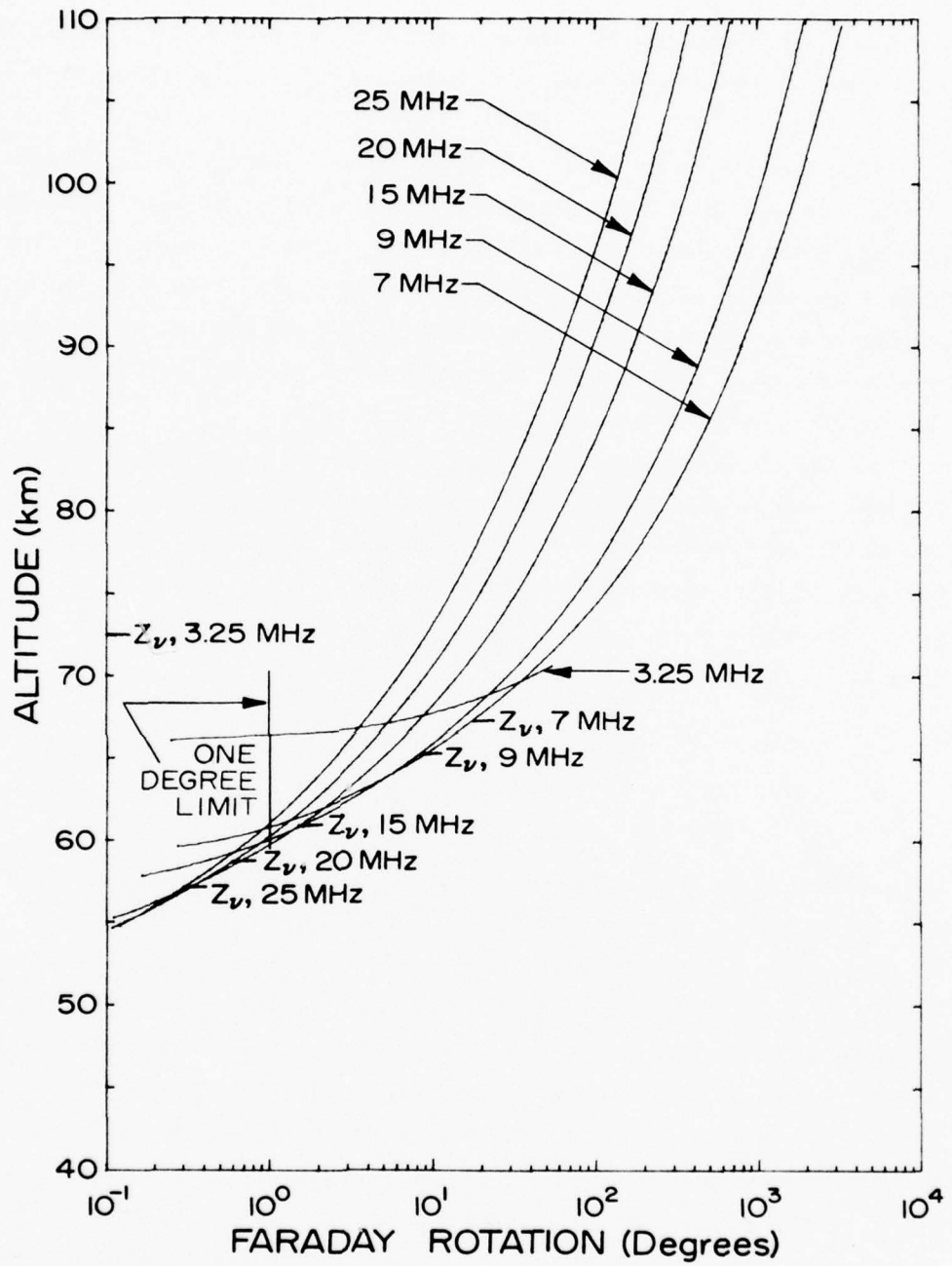


Figure 15. Faraday rotation profiles for the disturbed electron density and winter collision frequency profiles of Figures 7 and 8.

altitude. This problem is further complicated by additional modulation of the signal envelope produced by rocket coning as described in Appendix C.

The upper altitude limit for differential absorption was found to be -20.2 dB and intersects the 9 MHz curve at about 86 km. A frequency slightly greater than 9 MHz remains within this limit because of the asymptotic character of the curves. As anticipated, the 3.25 MHz signal has the lowest altitude of measurability (≈ 46 km) but only propagates to about 66 km before the extraordinary mode absorption is so great that the signal modulation can no longer be measured.

As the rocket moves into the upper D-region, the rate at which the recorded signal varies with altitude will give an indication of the resolution in the reduced data. It is desirable to specify analytically the decrease in accuracy of differential absorption measurements with altitude. We define Q as the rate of change in the signal envelope width relative to the maximum signal

$$Q = 2 \frac{dE_x}{dz} / (E_0 + E_x) .$$

This quantity is directly related to the accuracy of the measurement and equivalently, the number of data points that can be determined over an altitude z . Thus, if Q for a given frequency is about 0.1 over some distance, there would be roughly ten times the number of data points as compared to a signal with $Q = 0.01$ over the same distance. The dashed Q contour lines plotted in Figure 14 indicate the relative accuracy of differential absorption data for various frequencies. For the D-region conditions represented by this figure, a transmitter frequency of around 10 or 11 MHz will give the highest values of Q to the highest altitude. It is seen from the dashed contours that Q decreases with increasing altitude, and that for any given altitude there exists a distinct frequency giving the largest value of Q . This will be the frequency that provides the best resolution and hence the greatest accuracy.

The corresponding Faraday rotation values are shown in Figure 15. The lowest height for measurement of Faraday rotation, Z_v , decreases

as frequency increases. The 1° resolution forms a lower limit, however, for this decrease. At 18-19 MHz these two limits occur at about 59 km. The rate of change of Faraday rotation with altitude dF/dz is the quantity extracted from the telemetry data. Although dF/dz is not particularly small, it is seen that the values do indeed decrease with increasing frequency. Although the differential absorption becomes very difficult to read in the upper D-region, the electron density is sufficiently high that the Faraday rotation is easily measured. This is the reason the Faraday rotation can be recorded more accurately at higher altitudes than the differential absorption. Examination of the 3.25 MHz curves in Figures 14 and 15 shows that the upper limit for differential absorption measurements is very near the lower altitude limit for Faraday rotation. Thus, at 3.25 MHz there is not altitude where simultaneous measurements of Faraday rotation and differential absorption can be made.

Enough limits have now been prescribed that a choice of frequencies can be made to achieve optimum results for expected ionospheric conditions. For a disturbed polar ionosphere and moderate collision rates such as found in winter, the following frequencies are recommended.

19.0 MHz - Differential absorption data for
48 to 85 km. Faraday rotation data
for 59 to 110 km.

10 MHz - Differential absorption data for 48
to 90 km. Faraday rotation for 65
to 110 km.

3.25 MHz - Differential absorption data for 46
to 66 km. No Faraday rotation data.

The upper altitude limit for differential absorption was chosen for a value of Q which would give one data point per kilometer. It should be emphasized that above this level there is still differential absorption that can be measured, but the rate of absorption is too low to yield an accurate value every kilometer.

It is not possible to determine both electron density and collision frequency below 59 km since that is the lowest altitude for Faraday rotation measurements. The collision frequency can be extrapolated downward

to obtain estimated electron densities below 59 km. Even though it is indicated that Faraday rotation data for 19 MHz can be read down to 48 km, the data is a factor of 2 to 3 less accurate than the 10 MHz signal below 70 km.

Receiver requirements for this experiment are greatest for the 3.25 MHz signal where the noise temperature $T_a = 3 \times 10^{30}$ K corresponds to $0.38 \mu\text{V/m}$. The lowest range full scale voltage E_{R_1} must then be about $4.2 \mu\text{V/m}$. At $h_m \approx 46 \text{ km}$, $E_1 \approx 6.8 \text{ mV/m}$, so that 4 receiver ranges are needed. (As noise increases, less sensitivity is useable in the receiver.)

The calculations described above were repeated for a disturbed D-region but with the high collision frequency profile of Figure 8. The values are plotted in Figures 16 and 17. The higher collision rate increases the total absorption with the net result that the lowest altitude for reliable measurements has been raised about 4 km. For the same reason higher frequencies must be used to measure the top portion of the D-region ionosphere. The dashed lines in Figure 16 represent constant values of Q . The 1° and Z_V limits for Faraday rotation measurements occur about 65 km for a 25 MHz wave, Figure 17.

The three optimum frequencies for this model are:

25 MHz - Differential absorption data for 54 to 90 km. Faraday rotation data for 65 to 110 km.

14 MHz - Differential absorption data for 51 to 96 km. Rotation data for 71 to 110 km.

3.25 MHz - Differential absorption data from about 48 to 70 km.

Receiver requirements for these conditions are similar to the disturbed winter case. For an equivalent electric field noise of $0.38 \mu\text{V/m}$, 4 receiver ranges are needed to measure the signal at 51 km where the minimum signal is $1.2 \mu\text{V/m}$ and the maximum signal is 6.2 mV/m .

The third case of interest is that of a quiet D-region and winter collision rates. Utilizing the appropriate curves in Figures 7 and 8,

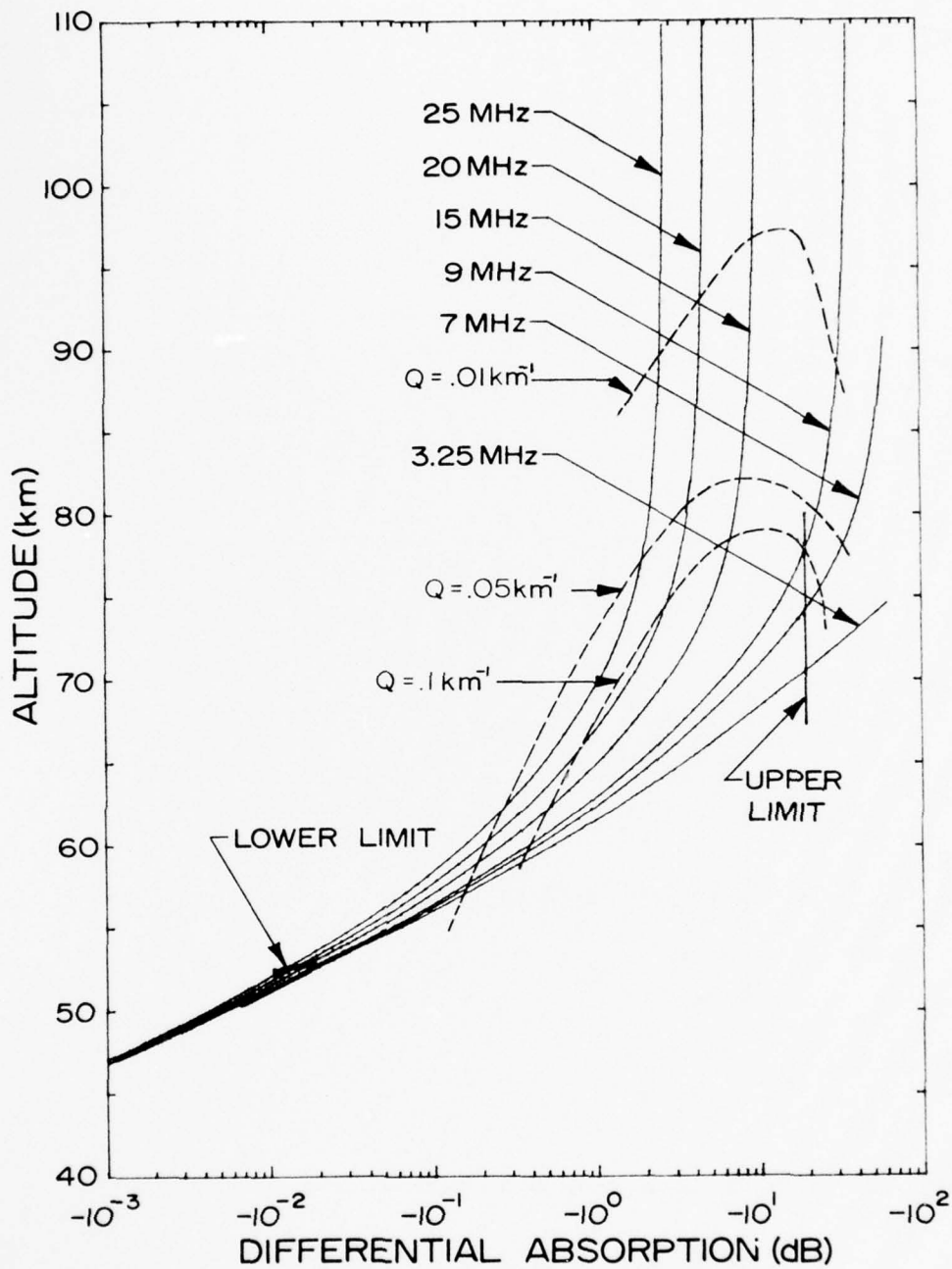


Figure 16. Differential absorption profiles for the disturbed electron density and summer collision frequency profiles of Figures 7 and 8.

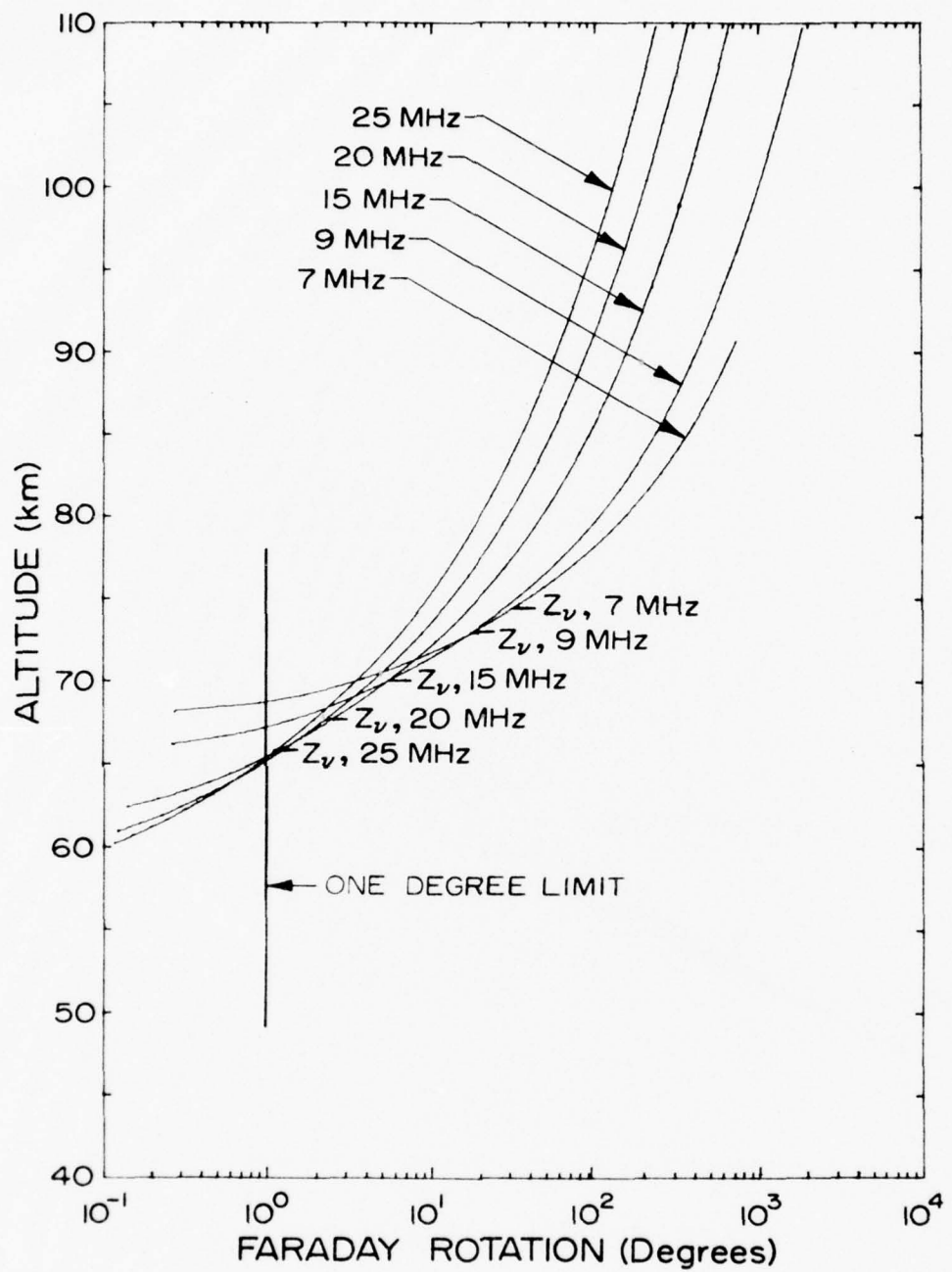


Figure 17. Faraday rotation profiles for the disturbed electron density and summer collision frequency profiles of Figures 7 and 8.

the differential absorption and Faraday rotation were calculated and plotted in Figures 18 and 19. Values of dA/dz and dF/dz for this case are much larger than for the disturbed cases. For the case of Faraday rotation, z_V for all frequencies is well below the 1° Faraday rotation altitude. For differential absorption measurements to 110 km, a frequency close to 4 MHz is needed. Frequencies greater than 7 MHz have values of Q less than 0.05 over the entire range. For this reason, they are not included in the figures. For measurements under these ionospheric conditions two frequencies would be selected:

4.25 MHz - Differential absorption data for
75 to 110 km. Faraday rotation
data 81 to 110 km.

3.25 MHz - Differential absorption data for
73 to 103 km. Faraday rotation
data for 79 to 106 km.

A 2.5 MHz curve was calculated for comparison with experiments described by *Bennett et al.*, [1972] and *Mechtly*, [1974] under similar atmospheric conditions. As can be seen this lower frequency yields more accurate results over the 70-90 km height region. Receiver requirements for the 3.25 MHz signal at the lower limit of 73 km also call for 4 ranges, the highest measuring a field of 4.4 millivolts/meter. This gives a total dynamic amplitude range of 2811:1.

In conclusion, it can be seen by comparison of Figures 14 and 18 and Figure 7, that while electron density measurements as low as 10 cm^{-3} are possible under quiet conditions, barely 100 cm^{-3} are attainable for the disturbed case. The difference, of course, is the higher degree of absorption for the disturbed case for any given electron density. This dependence also shows up by comparing Figures 14 and 16. Thus, as a general rule, measurement accuracy and electron density determination at lower altitudes decrease with increasing electron collision frequency profile.

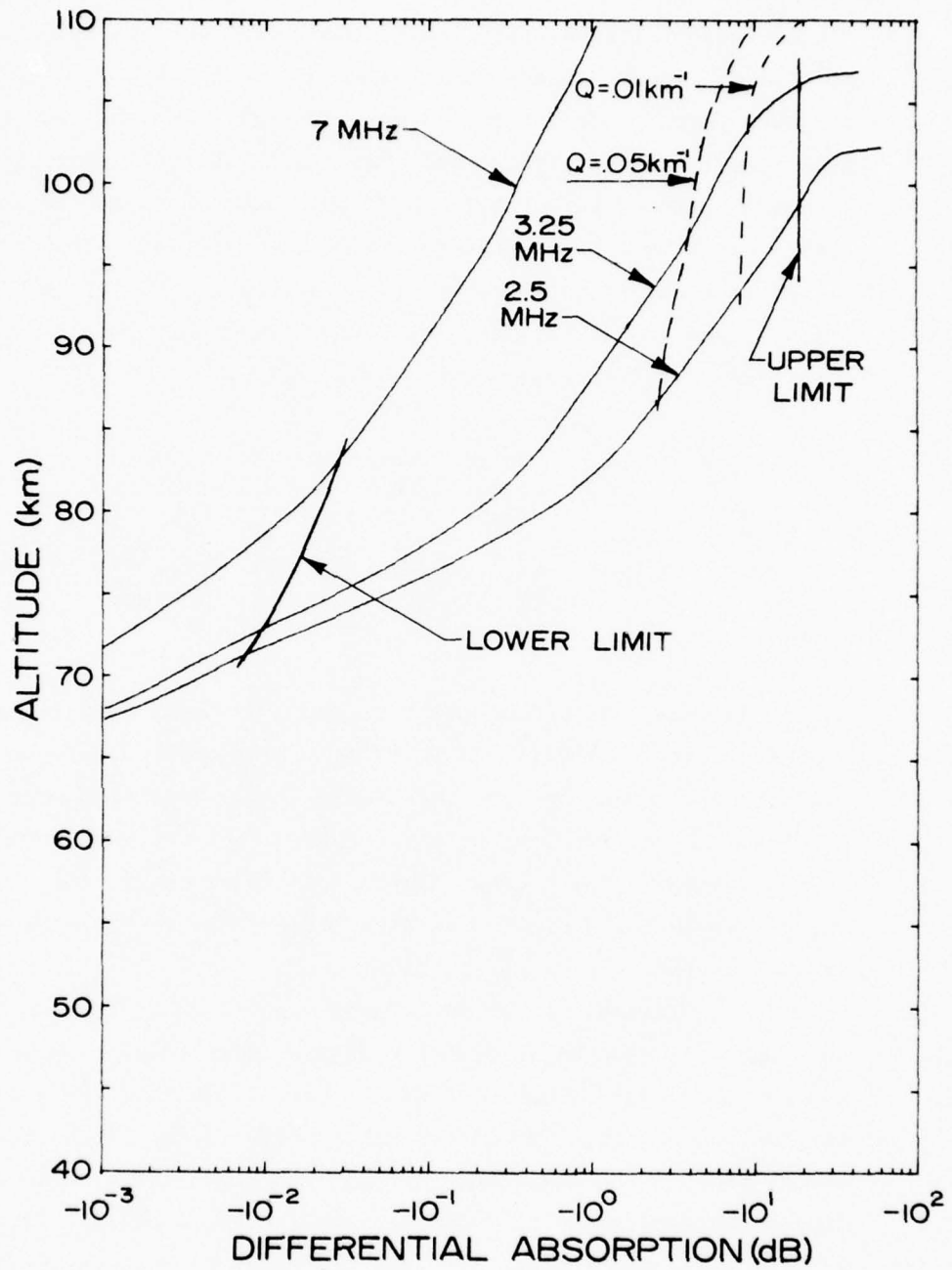


Figure 18. Differential absorption profiles for the quiet electron density and winter collision frequency profiles of Figures 7 and 8.

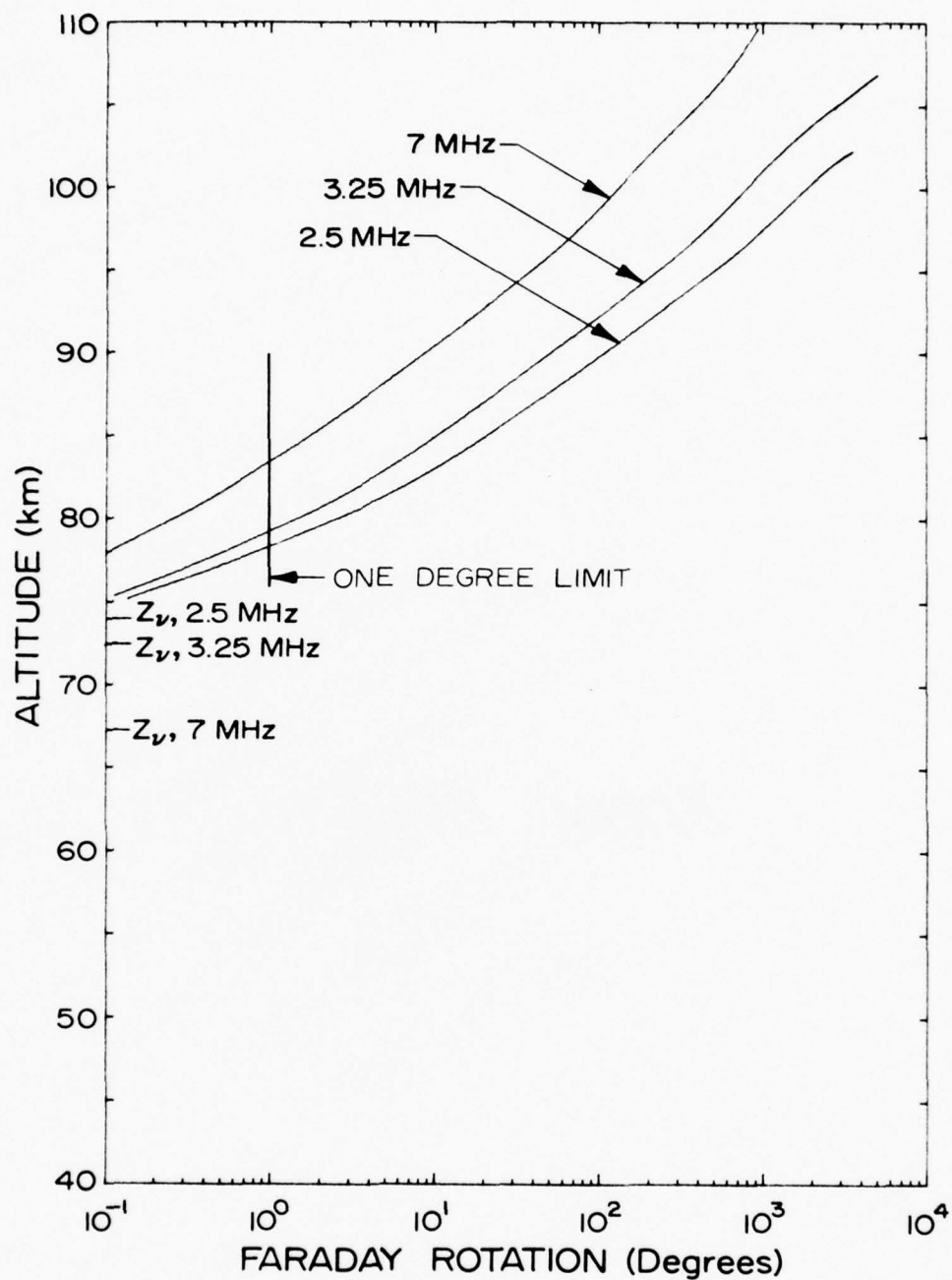


Figure 19. Faraday rotation profiles for the quiet electron density and winter collision frequency profiles of Figures 7 and 8.

CHAPTER IV
ANTENNAS

Ground Station Antennas

Signals from the ground station must radiate throughout that portion of the ionosphere traversed by the missile. A radiation pattern similar to that of a one-half wavelength dipole mounted horizontally one-fourth wavelength above a ground plane would be suitable. The antennas must be easily erected and movable from location to location as needed. It is to be noted that supporting masts, to be practical, cannot exceed about 25 or 30 feet in height without being permanently placed in position. The minimum frequency that could easily be used (with $\lambda/4$ height) would then be about 8 MHz. However, horizontal dipoles may be mounted somewhat lower than one-fourth wavelength without seriously affecting the radiation pattern.

Kraus [1950] gives a relationship for the gain in field intensity at large distances for a "Half-Wavelength Antenna Above Ground" (HWAG) with respect to that of a "Half-Wavelength Antenna in Free Space" (HWFS) as

$$G_f(\alpha) \left[\frac{\text{HWAG}}{\text{HWFS}} \right] = \sqrt{\frac{R_{11} + R_{1L}}{R_{11} + R_{1L} - R_m}} [2 \sin(h_r \sin \alpha)]$$

where

$h_r = 2\pi/\lambda$ times the height above ground = $(2\pi/\lambda)h$

R_{11} = self resistance of a $\lambda/2$ antenna

R_{1L} = loss resistance of the $\lambda/2$ antennas

R_m = mutual resistance of the $\lambda/2$ antenna and its image at a distance of $2h$

Plots of radiation patterns are given in Figure 20 for $h = 0.25 \lambda$, 0.1λ , and 0.05λ . R_{1L} is assumed zeros for the plots shown. It is seen that as h becomes smaller, the field intensity pattern deviates only slightly from the pattern for $h = \lambda/4$. However, the terminal impedance decreases rapidly as h decreases. For plot A the terminal impedance is

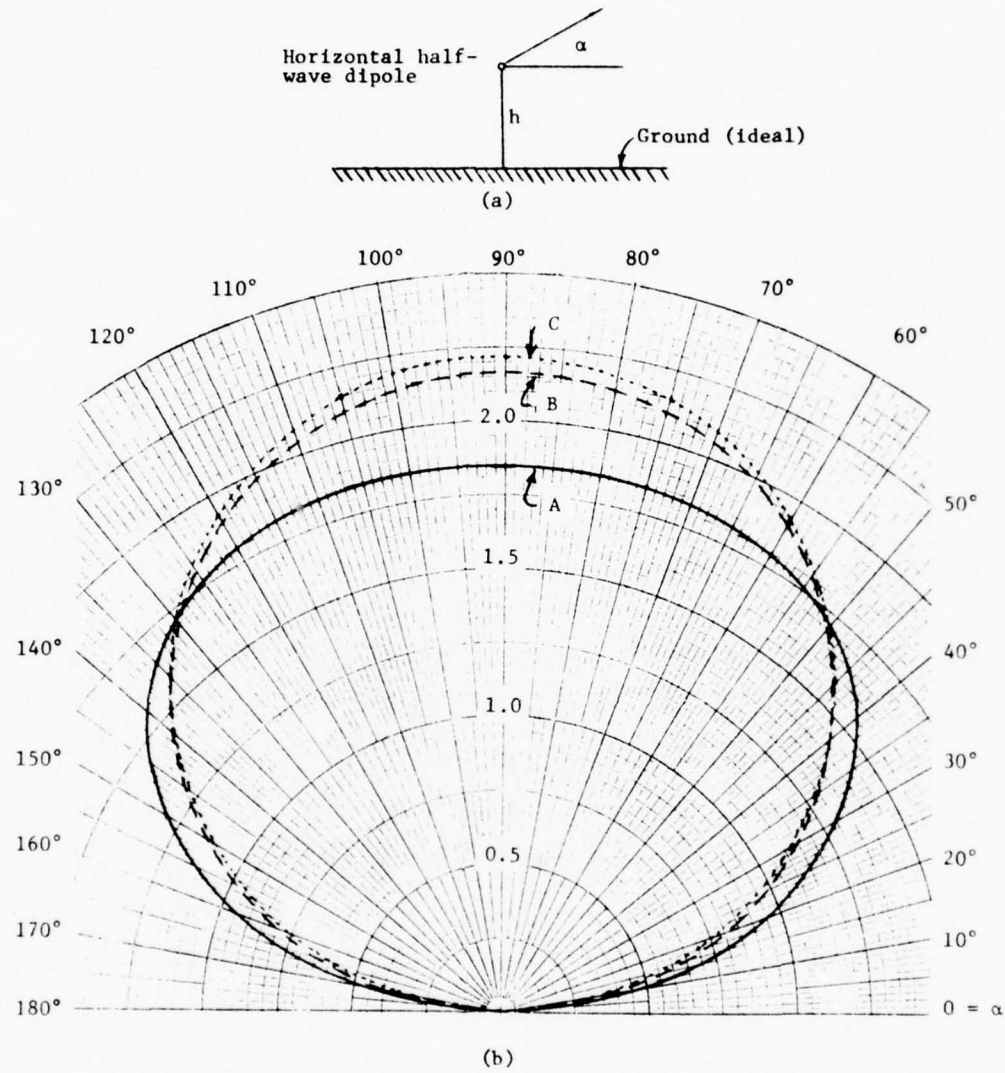


Figure 20. The half-wavelength dipoles, mounted above a ground plane as in (a) produce field intensity patterns as shown in (b) for A, $h = \lambda/4$; B, $h = \lambda/10$; and C, $h = \lambda/20$.

approximately 86 ohms, for B it is about 22 ohms, and for C it is about 6 ohms. When h is very small, the efficiency of the antenna would decrease because the loss resistance becomes significant compared to the radiation resistance. With minimum h chosen as $\lambda/10$, and with masts no higher than 30 feet, it is seen that the minimum frequency to be used for the propagation experiment should not be lower than about 3.25 MHz. As the frequency is increased, the decreasing wavelength will permit the antenna to be mounted a greater fraction of a wavelength above the ground plane.

Matching the antennas to the coaxial cable feed lines may be accomplished by using either of several matching networks. The lowest frequency antenna ($h = \lambda/10$) with a terminal impedance of $Z_t = 22 + jx$ for a $\lambda/2$ antenna may be efficiently matched rather easily. Z_t may be increased by a factor of 9 by using a 3-wire folded dipole. As shown in Figure 21, a coaxial cable drives one-half of the antenna directly from the center conductor. The other half of the antenna is excited from the center conductor through a $\lambda/2$ length of coaxial cable. The resulting terminal impedance is approximately $49 + j0$ ohms after the length of the antenna has been adjusted for zero reactance.

When higher frequencies are chosen, the height of the antennas may be adjusted to $h > \lambda/10$, and then 2-wire folded-dipoles may be used. The terminal impedance may again be adjusted for an excellent match with the 50 ohm source cable, as in Figure 21, by adjusting the height above the ground plane and by trimming the antenna length for zero reactance. The height of the antenna will then be about 0.16λ above a well defined ground plane.

Alternate matching networks make use of the balun for matching balanced to unbalanced impedances, or the network in Figure 22 may be used.

Each of the matching methods described for the folded- and single-wire antennas have been built and tested successfully at a frequency of 4 MHz in connection with this report.

The theoretical field intensity patterns shown in Figure 20 are difficult to measure without a suitable antenna range. However, an attempt was made to verify the radiation patterns for $h = \lambda/4$ and $\lambda/10$.

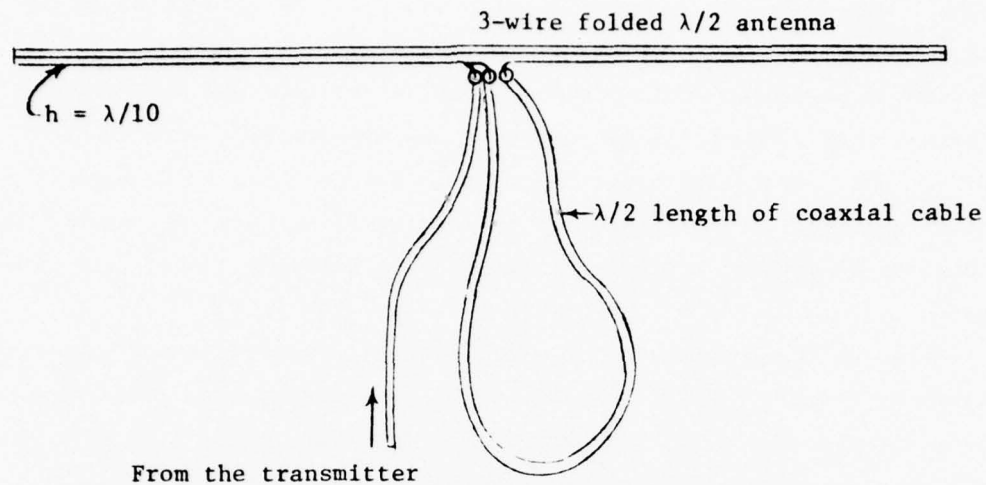


Figure 21. A three-wire folded half-wavelength antenna phased and driven by a coaxial cable. With $h \approx \lambda/10$ above the ground plane and with the length trimmed for zero reactance, the terminal impedance presented to the transmission line is $Z_t \approx 22 \Omega \times (3)^2/4 = 49 \Omega$.

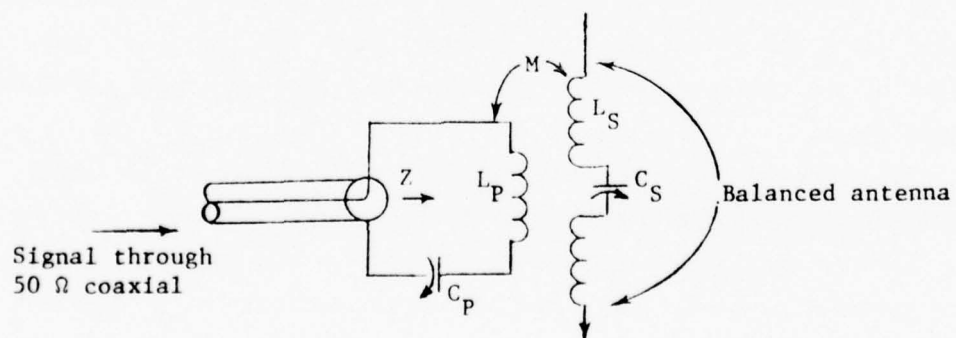


Figure 22. A tuned matching network for matching an unbalanced signal source to a balanced dipole antenna.

Vertical dipoles were mounted in front of a vertical screen and the radiation in the ground plane was measured. Field intensity patterns were measured with the spacing between the antenna and the screen adjusted first to $\lambda/10$ and then to $\lambda/4$. The model was operated at 24 MHz which permitted use of the smallest possible model within the range of available field-intensity measuring equipment. The vertical screen was 40 feet long and 15 feet high and consisted of vertical wires spaced 1 foot apart. Since the screen was only about 1 wavelength long, the horizontal radiation pattern was not expected to match the ideal pattern but only to verify the performance. The antenna and screen configurations are shown in Figure 23. The measured normalized field intensity patterns are shown in Figure 24. The field intensity was measured 45 meters from the center of the screen.

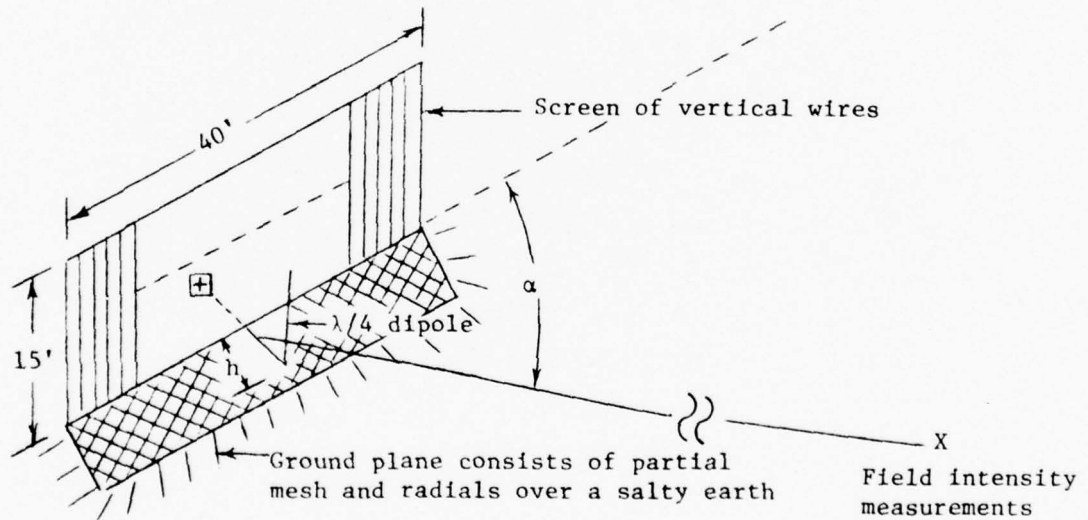


Figure 23. The field intensity measurements were made in the ground plane around the dipole and the screen. The antenna was excited through a coaxial cable from a signal generator located at X behind the screen.

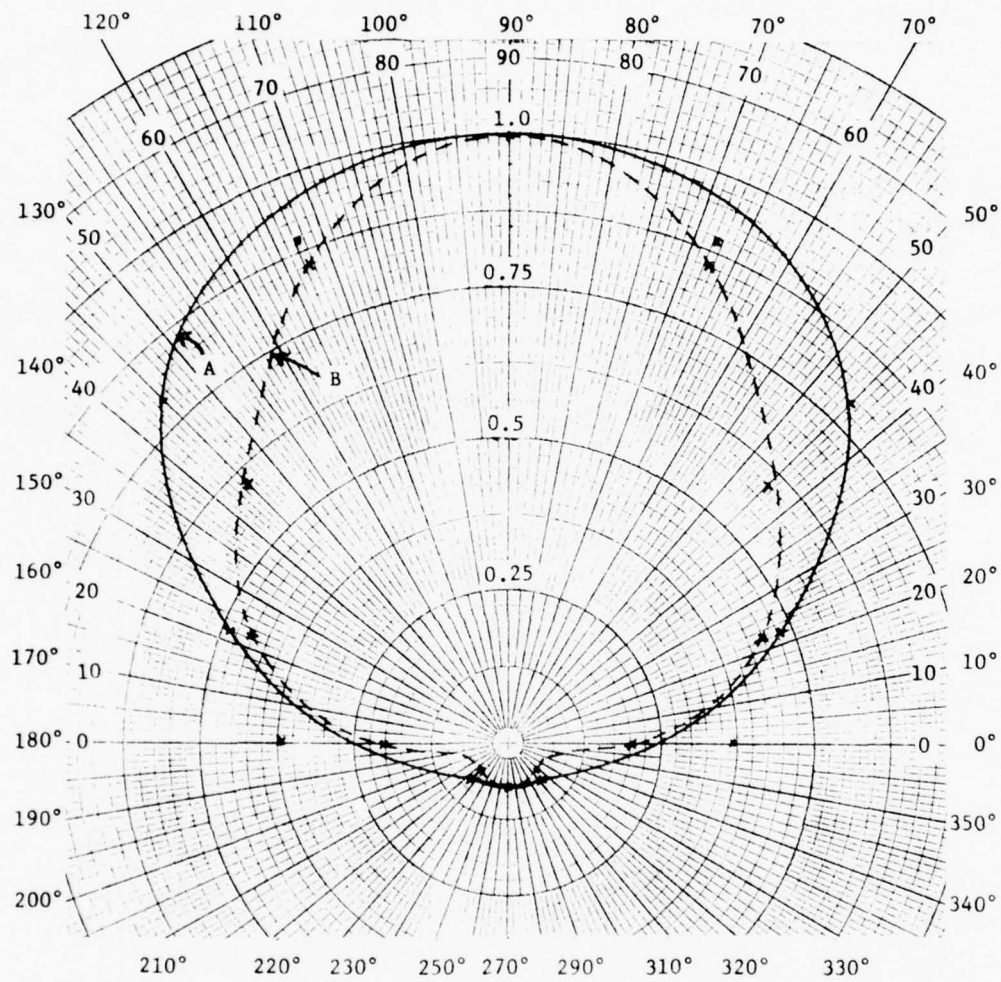


Figure 24. Measured, normalized, field intensity, patterns with a vertical $\lambda/4$ monopole (A) $\lambda/4$ in front of a 40' x 15' screen, and (B) $\lambda/10$ in front of the same screen. The frequency was 24 MHz.

Antennas for the Rocketborne Receiver

The small size and high velocity of the sounding rocket make the use of outboard antennas impractical. Therefore, ferrite core antennas are proposed for use with the payload.

Ferrite core antennas were fabricated and tested at frequencies of 4 MHz, 17 MHz, and 25 MHz. Initial tests were made using ferrite rods measuring 0.337 inches diameter x 7.5 inches long of Q₁ and Q₂ material from Permag Sierra Corporation. The objective was to determine the voltage at the output terminals of the antennas versus the field intensity. The Q₁ material was clearly superior in performance at 4 MHz, the Q₂ material gave the best results at 25 MHz, while at 17 MHz the two materials gave approximately equal results.

The final tests were made with the same core material shortened to 3.75 inches. The results using the shortened ferrite rods were approximately the same as those observed with the longer antenna rods except that the terminal voltages were roughly one-third less. It is anticipated that antenna rods will be less than 4 inches in length for most payloads using the propagation experiment because of the likelihood that small missiles will be used.

The antennas were fabricated by winding the ferrite rods with closely spaced turns of No. 24 Nylclad copper wire. Each antenna was tuned with about 10 pF capacitance. The terminal impedance of the antennas was adjusted to 1,000 ohms. An emitter follower was then used to match the antenna impedance to the 50 ohm terminal impedance of a Stoddard Model No. NM20-B RI-FI Meter which served as the field intensity meter and also as a sensitive voltmeter. Figure 25 shows the experimental arrangement used for measuring antenna terminal voltage versus field intensity. A typical result at 4 MHz was 65 μ V delivered by the antenna to a 1,000 ohm load with 1.55 mV/meter of electric field intensity. It is safe to say that 1 μ V of signal would produce a favorable signal to noise ratio so that a signal strength of 1.55×10^{-3} (V/m)/65 = 24×10^{-6} V/m. If the greatest distance between the transmitting and receiving antennas is 10^5 meters and if the gain of the transmitting antenna is given a safe value of 3.5, then we may calculate the transmitted power

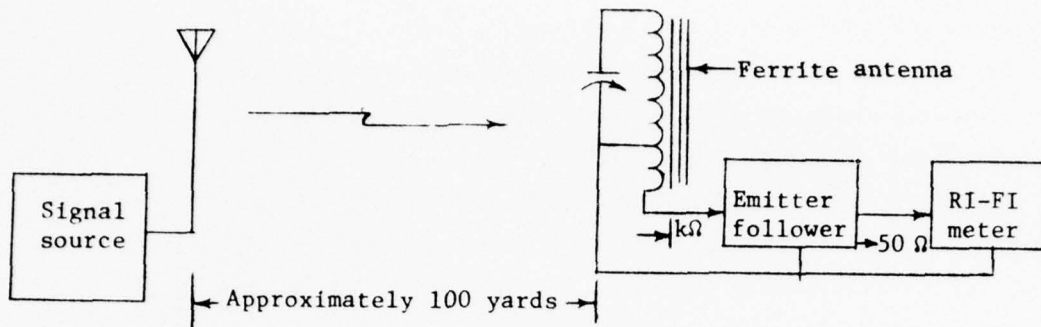


Figure 25. The experimental test used to determine antenna terminal voltage versus field intensity. Both the output voltage of the antenna and the strength of the E-field were measured with the IR-FI Meter.

without the effects of Faraday rotation and attenuation through the ionosphere. There is good evidence from the work of Dr. Harris (Utah State University) that the dynamic range imposed by Faraday rotation is about 100 to 1, and that the absorption of the signal at the lowest frequencies of interest imposes another factor of 100. The transmittal power may then be calculated from the relationship

$$P_T = \frac{4\pi r^2 P_d}{G_T} \times (\text{attenuation factor}) \times (\text{Faraday rotation factor})$$

P_d = power density at the receiving antenna

$$= \frac{E^2}{Z_0} = \frac{(24 \times 10^{-6} \text{ V/m})^2}{377} = 1.53 \times 10^{-2} \text{ W/m}^2$$

$$r = 10^5 \text{ m}$$

$$G_T = 3.5$$

$$P_T = \frac{4\pi \times 10^{10} \times 1.53 \times 10^{-12}}{3.5} \times 100 \times 100$$

$$= 549 \text{ watts}$$

That level of transmitted power is not only reasonable but it appears to be on the safe side since a good receiver can operate with a suitable signal-to-noise ratio with about 0.1 mV of input signal in a relatively quiet environment. Since the environmental noise at the receiver is a composite from many possible sources and is unknown *a priori*, it would seem that the ground based transmitter should deliver 700 to 1,000 watts to the transmitting antennas.

Although the transmitted power requirement may vary slightly from one frequency to another, the worst case is that of the example above. Therefore, transmitted power in the range of 700 to 1,000 watts should be adequate for any frequency utilized in the propagation experiment. Inexpensive transmitters are readily available for these power levels and the frequencies of interest.

CHAPTER V
CONCLUSIONS

The goal of this work was the development of a multiple frequency propagation experiment to measure electron densities and electron collision rates in the ionospheric D-region. This experiment was designed to utilize standard HF transmitters and simple antenna systems that could be low power, portable and inexpensive. This experiment employs the radio wave signals to measure the Faraday rotation and differential absorption between ground transmitters and rocket-borne receivers traveling through the D-region. The time history of the Faraday rotation and differential absorption then permit an evaluation of the height profiles of electron density and collision rate.

A theoretical propagation model, based on the Sen-Wyller form of the magnetohydrodynamic equations, was developed to numerically calculate the wave propagation from ground to rocket at high magnetic latitudes. This propagation model included the limitations imposed by noise, equipment sensitivity and data evaluation. Curves of Faraday rotation and differential absorption, based on extreme values of electron density and electron collision rate as might be seen in the polar latitudes, were calculated to illustrate the frequencies and altitudes at which this propagation experiment would be successful. It was found that under quiet ionospheric conditions electron densities as low as 10 cm^{-3} could be measured by this propagation experiment, whereas increased collision rates such as occur in disturbed conditions reduce the resolution to less than 100 cm^{-3} . Appendix C contains an extensive derivation of the effect of rocket coning on the received signal. We found that rocket coning could produce significant errors in the apparent values of Faraday rotation and differential absorption, and that these errors were not systematic and not removable by simple averaging technique. A method was developed to remove this perturbation from the Faraday rotation and differential absorption data with the aid of continuous rocket attitude information. This technique also permits the calculation of electron

density and electron collision rate from the raw Faraday rotation and differential absorption data.

Chapter IV summarizes a study of antennas proposed for use in the rocket and also for the ground transmitter. It appears that a transmitter power in the range of 700 to 1000 watts radiating on horizontal half-wave dipoles will be adequate for this propagation experiment. The rocketborne receiving antennas utilize ferrite core loops.

The calculated curves of Faraday rotation and differential absorption together with the constraints already mentioned were used to evaluate wave frequencies for the extreme ionospheric conditions posed in Chapter III. These are summarized in the following table. Although 3.25 MHz was the lowest frequency considered in this study, frequencies lower than 3.25 MHz might be useful in other special cases.

Polar D-Region Ionospheric Conditions	Proposed Frequencies (MHz)
Winter disturbed	3.25, 10., 19.
Winter quiet	3.25, 4.25
Summer disturbed	3.25, 14., 25.
Summer quiet	3.25, 6.0

It is our conclusion that a multifrequency propagation experiment is a viable scheme for obtaining accurate D-region electron density profiles. The techniques that have been developed in this work allow an evaluation of frequencies before hand so that optimum results can be obtained; and accurate methods of data evaluation after the rocket flight.

REFERENCES

- Adams, G.W., Faraday rotation experiments in the D region, *NOAA Technical Report ERL 205-SEL 21*, 1971.
- Appleton, E.V., Wireless studies of the ionosphere, *J. Instn. Elec. Engrs.* 71, 642-650, 1932.
- Belrose, J.S., L.R. Bode and L.W. Hewitt, A preliminary investigation of diurnal and seasonal changes in electron number density over resolute bay as observed by partial reflections, *Electron Density Profiles in Ionosphere and Exosphere*, 629 pp., North-Holland Publishing Co., 1966.
- Bennett, F.D.G., J.E. Hall, and P.H.G. Dickenson, *J. Atmosph. Terr. Phys.* 34, 1321-1335, 1972.
- Dean, W.A., Electron density profiles for the 1969 PCA event, *Proceedings of COSPAR Symposium on Solar Particle Event of November 1969*, 291-305, 1972.
- Dickenson, P.H.G., J.E. Hall, and F.D.G. Bennett, Rocket measurements of electron concentration in the lower ionosphere at two European locations, *J. Atmosph. Terr. Phys.* 38, 163-173, 1976.
- Dingle, R.B., D. Arndt, and S.K. Roy, The integrals of $C_p(x)$ and $D_p(x)$ and their tabulation, *Appl. Sci. Res.* 6B, 155-164, 1957.
- Faire, A.C. and E.A. Murphy, Neutral density and temperature measurements, *Proceedings of COSPAR Symposium on Solar Particle Event of November 1969*, 445-461, 1972.
- Ginther, J.C. and L.G. Smith, Studies of the differential absorption rocket experiment, *Aeron. Rep. No. 54*, Aeron. Lab., Dep. Elec. Engr., Univ. Ill., Urbana-Champaign, 63-66, 1975.
- Hara, E.H., Approximations to the semiconductor integrals $C_p(x)$ and $D_p(x)$ for use with the generalized Appleton-Hartree magnetoionic formulas, *J. Geophys. Res.* 68(14), 4388-4389, 1963.
- Hartree, D.R., The propagation of electro-magnetic waves in a refracting medium in a magnetic field, *Proc. Cambridge Phil. Soc.* 27, 143-162, 1931.
- Jordan, E.C. and K.G. Balmain, *Electromagnetic Waves and Radiating Systems*, Prentice-Hall, Inc., Englewood Cliffs, New Jersey, 1968.
- Kane, J.A., Arctic measurements of electron collision frequencies in the D-region of the ionosphere, *J. Geophys. Res.* 64, 133-139, 1959.

Kelso, J.M., *Radio Ray Propagation in the Ionosphere*, 408 pp., McGraw-Hill Book Co., 1964.

Knoebel, H.W. and D.O. Skaperdas, Rocket measurements of Faraday rotation and differential absorption, *Rev. Sci. Instr.* 37, 1395-1400, 1955.

Kraus, J.D., *Antennas*, 543 pp., McGraw-Hill Book Co., 1950.

Mechtly, E.A., S.A. Bowhill, L.G. Smith, and H. Knoebel, Lower ionosphere electron concentration and collision frequency from rocket measurements of Faraday rotation, differential absorption, and probe current, *J. Geophys. Res.* 72, 5239-5245, 1967.

Mechtly, E.A., K. Seino, and L.G. Smith, Lower ionosphere electron densities measured during the solar eclipse of November 12, 1966, *Radio Sci.* 4, 371-375, 1969.

Mechtly, E.A., Accuracy of rocket measurements of lower ionosphere electron concentrations, *Radio Sci.* 9, 373-378, 1974.

Megill, L.R., G.W. Adams, J.C. Haslett, and E.C. Whipple, Measurement of the effective electron loss rates in the D-region during polar cap absorption events, *J. Geophys. Res.* 76, 4587-4595, 1971.

Pack, J.L. and A.V. Phelps, Drift velocities of slow electrons in helium, neon, argon, hydrogen, and nitrogen, *Phys. Rev.* 121, 798-806, 1961.

Phelps, A.V. and J.L. Pack, Electron collision frequencies in nitrogen and in the lower ionosphere, *Phys. Rev. Letters* 3, 340-342, 1959.

Ratcliffe, J.A., *The Magneto-ionic Theory and Its Applications to the Ionosphere*, 206 pp., Cambridge University Press, 1962.

Sen, H.K. and A.A. Wyller, On the generalization of the Appleton-Hartree magnetoionic formulas, *J. Geophys. Res.* 65(12), 3931-3950, 1960.

Thrane, E.V. and W.R. Piggott, The collision frequency in the E- and D-regions of the ionosphere, *J. Atmosph. Terr. Phys.* 28, 721-732, 1966.

Ulwick, J.C., Comparison of Black Brant rocket measurements of charged particle densities during solar particle events, *Proceedings of COSPAR Symposium on Solar Particle Event of November 1969*, 395-410, 1972.

APPENDIX A. MAGNETOIONIC FORMULAS

The generalized complex refractive index given by *Sen* and *Wyller*, [1960] is

$$(\mu - jx)^2 = \frac{A + B \sin^2 \phi \pm \sqrt{B^2 \sin^4 \phi - C^2 \cos^2 \phi}}{D + E \sin^2 \phi}$$

where

$$\begin{aligned} A &= 2 \varepsilon_I (\varepsilon_I + \varepsilon_{III}) \\ B &= \varepsilon_{III} (\varepsilon_I + \varepsilon_{III}) + \varepsilon_{II}^2 \\ C &= 2 \varepsilon_I \varepsilon_{II} \\ D &= 2 \varepsilon_I \\ E &= 2 \varepsilon_{III} \end{aligned}$$

The ε 's are elements of the generalized dielectric tensor

$$\varepsilon = \begin{bmatrix} \varepsilon_I + \varepsilon_{III} \cos^2 \phi & -\varepsilon_{II} \cos \phi & -\varepsilon_{III} \sin \phi \cos \phi \\ \varepsilon_{II} \cos \phi & \varepsilon_I + \varepsilon_{III} & -\varepsilon_{II} \sin \phi \\ -\varepsilon_{III} \sin \phi \cos \phi & \varepsilon_{II} \sin \phi & \varepsilon_I + \varepsilon_{III} \sin^2 \phi \end{bmatrix}$$

where

$$\varepsilon_I = (1-a) - i b$$

$$\varepsilon_{II} = \frac{1}{2} [(f-d) + i(c-e)]$$

$$\varepsilon_{III} = a - \frac{1}{2}(c+e) + i[b - \frac{1}{2}(f+d)]$$

$$a = \frac{\omega_p^2}{\nu_m} C^{3/2} \left(\frac{\omega}{\nu_m} \right)$$

$$b = \frac{5\omega_p^2}{2\omega v_m} C_{5/2} \left(\frac{\omega}{v_m} \right)$$

$$c = \frac{\omega_p^2 (\omega - s)}{\omega v_m^2} C_{3/2} \left(\frac{\omega - s}{v_m} \right)$$

$$d = \frac{5\omega_p^2}{2\omega v_m} C_{5/2} \left(\frac{\omega + s}{v_m} \right)$$

$$e = \frac{\omega_p^2 (\omega + s)}{\omega v_m^2} C_{3/2} \left(\frac{\omega + s}{v_m} \right)$$

$$f = \frac{5\omega_p^2}{2\omega v_m} C_{5/2} \left(\frac{\omega + s}{v_m} \right) .$$

The qualities ω , ω_p , v_m are wave frequency, plasma frequency, and collision frequency, respectively. The semiconductor integrals represented by $C_{3/2}$ and $C_{5/2}$ are described by Dingle, et al. [1957] and can be suitably approximated by polynomials given by Hara [1963].

$$C_{3/2}(x) = \frac{x^4 + a_3x^3 + a_2x^2 + a_1x + a_0}{x^6 + b_5x^5 + b_4x^4 + b_3x^3 + b_2x^2 + b_1x + b_0}$$

$$\begin{aligned} a_0 &= 2.3983474 \times 10^{-2} \\ a_1 &= 1.1287513 \times 10 \\ a_2 &= 1.1394160 \times 10^{+2} \\ a_3 &= 2.4653115 \times 10 \end{aligned}$$

$$\begin{aligned} b_0 &= 1.8064128 \times 10^{-2} \\ b_1 &= 9.3877372 \\ b_2 &= 1.4921254 \times 10^{+2} \\ b_3 &= 2.8958085 \times 10^{+2} \\ b_4 &= 1.2049512 \times 10^{+2} \\ b_5 &= 1.4656819 \times 10 \end{aligned}$$

$$C_{5/2}(x) = \frac{x^3 + a_2x^2 + a_1x + a_0}{x^5 + b_4x^4 + b_3x^3 + b_2x^2 + b_1x + b_0}$$

$a_0 = 1.1630641$
 $a_1 = 1.6901002 \times 10$
 $a_2 = 6.6945939$

$b_0 = 4.3605732$
 $b_1 = 6.4093464 \times 10$
 $b_2 = 6.8920505 \times 10$
 $b_3 = 3.5355257 \times 10$
 $b_4 = 6.6314497$

APPENDIX B
THE WAVE ELECTRIC FIELD VECTOR

Accurate reduction of telemetered propagation data requires a determination of the ray path between the radio transmitter and the rocket receiver. In general, an electromagnetic wave propagating through a continuously varying, stratified anisotropic medium will bend away from regions where the index of refraction μ decreases. This phenomenon leads to the process of radio wave reflection from the ionosphere. (See Ratcliffe, 1961, pp. 190-191).

In order to calculate the ray path it is generally necessary to divide the ionized medium into thin layers with the requirement that $\Delta\mu_i = \mu_{i+1} - \mu_i$ and $\Delta\chi_i = \chi_{i+1} - \chi_i$ are small compared to μ_i . The i^{th} layer may then be characterized by average values of the indices $\mu'_i = (\mu_{i+1} + 4\mu_{i+.5} + \mu_i)/6$ and $\chi'_i = (\chi_{i+1} + 4\chi_{i+.5} + \chi_i)/6$, where $\mu_{i+.5}$ and $\chi_{i+.5}$ are the indices at $(z_i + z_{i+1})/2$. The change in ray path direction at the surface of two media of different refractive index is given by Snell's law; $\mu_i \sin\theta_i = \mu_{i+1} \sin\theta_{i+1}$, where the variation in θ over the ray path is small enough (less than 5°) to be ignored so that $\mu_{i+1}(\theta_{i+1}) \approx \mu_i(\theta_i)$.

Utilizing this expression to calculate the deflection of a typical wave frequency propagating through the altitudes where differential absorption can be measured, it was found that in a 5 km thick layer, the deflection was less than 0.1° . Thus, in our calculations of differential absorption and Faraday rotation we can assume that the ray paths are straight lines.

Another characteristic of propagating waves in an ionized medium is the tendency for the E-field to acquire a component in the direction of propagation. For calculations involving rocket coning, it is necessary to show that the longitudinal E-field component is very small. To determine the plane of the phasor E, we must find the relative magnitude of E_z (the component of E in the direction of wave propagation) in terms of E_x or E_y . This can be found by a derivation similar to that for the wave polarization R. By substituting the dielectric tensor in Appendix A

into Maxwell's equations and solving for E_z/E_y , we can numerically determine the relative magnitude of the longitudinal E-field component for the coordinate system of Figure 3. The result

$$\frac{E_z}{E_y} = \frac{[(\mu - j\chi)^2 E - 2B]}{C} \sin\phi$$

can be evaluated by substituting typical values for ω , v , n_e , etc. into the expressions for B , C , E , and ϕ . Calculations show that $E_z/E_y \leq 10^{-4} + j 10^{-4}$ for typical ionospheric parameters.

We can safely conclude that for all practical applications E lies in a plane perpendicular to the ray path, which was shown to be essentially a straight line from the ground antenna to the rocket vehicle.

APPENDIX C

The effects of coning on the signal at the rocket can be described analytically by developing equations that transform the coordinate frame in which the antenna is stationary to that in which the ellipse traced out by the radio wave E-field vector is stationary, the Faraday rotation frame. Coordinate rotations are required that transform $(\underline{x}^a, \underline{y}^a, \underline{z}^a)$, where \underline{z}^a is defined as the rocket spin axis, \underline{x}^a is the direction along the antenna, and \underline{y}^a is perpendicular to both \underline{x}^a and \underline{z}^a , to the coordinates $(\underline{x}^t, \underline{y}^t, \underline{z}^t)$, where \underline{z}^t is the coning axis, \underline{y}^t points magnetic north and \underline{x}^t is perpendicular to both \underline{y}^t and \underline{z}^t . The rotational motion of the rocket in a frame fixed relative to an observer on the earth, can be described by $\dot{\alpha} = d\alpha/dt$, the rocket spin rate. The coning angle β is the angle between the rocket major axis (spin axis \underline{z}^a) and the coning axis \underline{z}^t . Finally, define $\dot{\gamma} = d\gamma/dt$ to be the coning rate; the angular velocity by which the rocket axis \underline{z}^a precesses about the axis \underline{z}^t . Figure C1 shows the spatial relationships between the two coordinate frames and the angles defined above. A clockwise rotation α about the \underline{z}^a axis can be represented by

$$S = \begin{Bmatrix} \cos \dot{\alpha} t & -\sin \dot{\alpha} t & 0 \\ \sin \dot{\alpha} t & \cos \dot{\alpha} t & 0 \\ 0 & 0 & 1 \end{Bmatrix} \quad (C1)$$

Thus $\underline{x}^b = S\underline{x}^a$. The next rotation is about \underline{x}^b and causes $\underline{z}^b = S\underline{z}^a$ to be rotated by an angle β into coincidence with \underline{z}^t . This is a clockwise rotation that can be represented by

$$C = \begin{Bmatrix} 1 & 0 & 0 \\ 0 & \cos \beta & -\sin \beta \\ 0 & \sin \beta & \cos \beta \end{Bmatrix} \quad (C2)$$

The geometry of this situation is illustrated in Figure C2 where $\underline{z}^t = C\underline{z}^b = CS\underline{z}^a$. The axis $\underline{y}^c = C\underline{y}^b = CS\underline{y}^a$ lies in the plane defined by \underline{x}^t

and \underline{y}^t . The rocket antenna now lies in the $(\underline{x}^t, \underline{y}^t)$ plane by the transformations S and C so that $\underline{x}^c = C\underline{x}^b = CS\underline{x}^a$. Finally, the $(\underline{x}^t, \underline{y}^t)$ plane is rotated about the \underline{z}^t axis by γ degrees so that \underline{x}^c and \underline{y}^c now align with \underline{x}^t and \underline{y}^t respectively. Again this is a clockwise rotation, and is represented by

$$P = \begin{Bmatrix} \cos \dot{\gamma}t & -\sin \dot{\gamma}t & 0 \\ \sin \dot{\gamma}t & \cos \dot{\gamma}t & 0 \\ 0 & 0 & 1 \end{Bmatrix} . \quad (C3)$$

The matrix PCS transforms the stationary rocket antenna axes into a coordinate system that is stationary with respect to an observer on the ground.

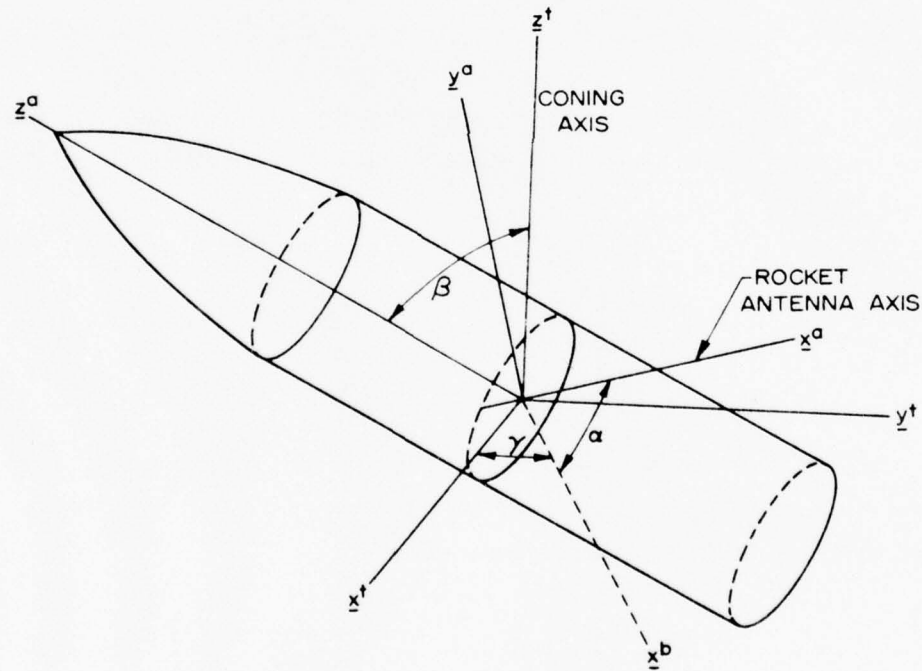


Figure C1. Stationary antenna frame $(\underline{x}^a, \underline{y}^a, \underline{z}^a)$ orientation relative to $(\underline{x}^t, \underline{y}^t, \underline{z}^t)$.

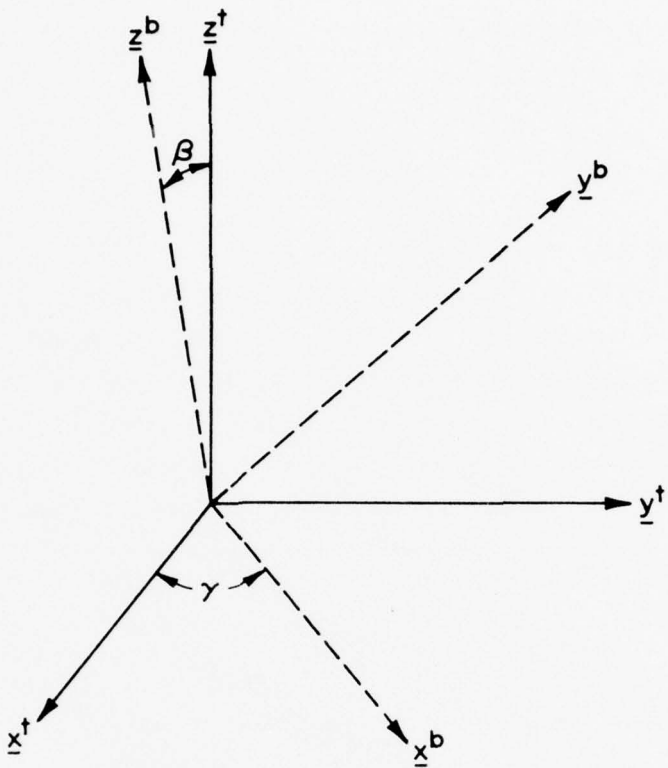


Figure C2. Orientation of $(\underline{x}^b, \underline{y}^b, \underline{z}^b)$ to $(\underline{x}^t, \underline{y}^t, \underline{z}^t)$.

Assume an angle δ exists between the radio wave ray paths and the axis \underline{z}^t about which the rocket precesses. The rotation matrix

$$D = \begin{Bmatrix} 1 & 0 & 0 \\ 0 & \cos \delta & \sin \delta \\ 0 & -\sin \delta & \cos \delta \end{Bmatrix} \quad (C4)$$

describes a rotation about the \underline{x}^t axis, taking the $(\underline{y}^t, \underline{z}^t)$ axes into the $(\underline{y}', \underline{z}')$ axes of Figure 2 of Chapter II. The transformation from $(\underline{x}', \underline{y}', \underline{z}')$ to the Faraday rotation frame $(\underline{x}^r, \underline{y}^r, \underline{z}^r)$ was developed in

Chapter II and is contained in the matrix R of equation (14). Summing all the rotations gives the matrix

$$T = RDPCS \quad (C5)$$

which transforms the antenna coordinate axes of a spinning, coning rocket to the Faraday rotation frame in the ionospheric medium.

The angle δ between the ray path \underline{z}' and the coning axis \underline{z}^t may be impossible to determine experimentally. We assume that \underline{z}^t points in the direction of the spin axis at launch. If the transmitter is close to the launch site, then the assumption that δ is less than 5° is probably reasonable at least for the up-leg and the D-region. With δ less than about 30° , the rotation D can be approximated by the expression

$$D \approx \begin{Bmatrix} 1 & 0 & 0 \\ 0 & 1 & 0 \\ 0 & 0 & 1 \end{Bmatrix} + \begin{Bmatrix} 0 & 0 & 0 \\ 0 & -\delta^2/2 & \delta \\ 0 & -\delta & -\delta^2/2 \end{Bmatrix} = I + D' \quad (C6)$$

with less than 5% error. Since the measurement of the coning angle depends upon the linearity of the magnetometer, we can associate any non-negligible experimental error by b. Substituting $\beta \pm b$ into (C2) with b small allows us to write

$$C \approx \begin{Bmatrix} 1 & 0 & 0 \\ 0 & \cos\beta & -\sin\beta \\ 0 & \sin\beta & \cos\beta \end{Bmatrix} + \begin{Bmatrix} 0 & 0 & 0 \\ 0 & \pm b\sin\beta & \pm b\sin\beta \\ 0 & \pm b\cos\beta & \pm b\sin\beta \end{Bmatrix} \quad (C7)$$

$$\approx C + E'$$

where E' is an error matrix. Substituting (C7) and (C6) into (C5) gives

$$T = RPCS + RD'PCS + RPE'S + \text{higher order error terms.}$$

The matrix product RPCS is the principal term; the other terms being error

matrices whose elements are only a small percentage of the principal matrix elements. The matrix elements for $T \approx \text{RPCS}$ are

$$\begin{aligned}
 T_{11} &= \cos\gamma' \cos\dot{\alpha} - \sin\gamma' \cos\beta \sin\dot{\alpha} \\
 T_{12} &= -\cos\gamma' \sin\dot{\alpha} - \sin\gamma' \cos\beta \cos\dot{\alpha} \\
 T_{13} &= \sin\gamma' \sin\beta \\
 T_{21} &= \sin\gamma' \cos\dot{\alpha} + \cos\gamma' \cos\beta \sin\dot{\alpha} \\
 T_{22} &= -\sin\gamma' \sin\dot{\alpha} + \cos\gamma' \cos\beta \sin\dot{\alpha} \\
 T_{23} &= -\cos\gamma' \sin\beta \\
 T_{31} &= \sin\beta \sin\dot{\alpha} \\
 T_{32} &= \sin\beta \cos\dot{\alpha} \\
 T_{33} &= \cos\beta
 \end{aligned} \tag{C8}$$

where $\gamma' = \gamma t - F$ and $F = (\phi_o - \phi_x)/2$, the Faraday rotation angle.

As a result of ignoring δ , the coning angle γt is measured in the plane of polarization so that the Faraday rotation either advances or retards the precession effect appearing in the unreduced data. The direction of the rocket dipole antenna relative to the Faraday rotation frame is $\underline{\tau}^r = T \cdot \underline{\tau}^a$, where $\underline{\tau}^a$ is the unit vector in the \underline{x}^a direction.

$$\begin{aligned}
 \underline{\tau}^r &= [\cos\gamma' \cos\dot{\alpha} - \sin\gamma' \cos\beta \sin\dot{\alpha}] \underline{x}^r \\
 &\quad + [\sin\gamma' \cos\dot{\alpha} + \cos\gamma' \cos\beta \sin\dot{\alpha}] \underline{y}^r + \sin\beta \sin\dot{\alpha} \underline{z}^r
 \end{aligned} \tag{C9}$$

The potential measured at the base of the antenna is proportional to the integrated electric field component parallel to the antenna. The scalar product of equation 16 of Chapter II and (C9) gives

$$\begin{aligned}
 E_s' &= [\cos\gamma' \cos\dot{\alpha} - \sin\gamma' \cos\beta \sin\dot{\alpha}] E_1 \cos[\omega t - (\phi_o + \phi_x)/2] \\
 &\quad - [\sin\gamma' \cos\dot{\alpha} + \cos\gamma' \cos\beta \sin\dot{\alpha}] E_2 \sin[\omega t - (\phi_o + \phi_x)/2]
 \end{aligned} \tag{C10}$$

where E_1 and E_2 are given by equation 19 of Chapter II. In the absence

of coning, $\beta = 0$ and γ' combines with $\dot{\alpha}$ so that (C10) reduces to equation 24 of Chapter II. The maximum value of equation (C10) in the wave period $2\pi/\omega$ is found by setting $\frac{dE_s}{dt} = 0$ with the assumption that $\dot{\alpha}, \dot{\gamma} \ll \omega$. The result

$$\left[\omega t - \frac{(\phi_o + \phi_x)}{2} \right]_{\max} = -\tan^{-1} \left\{ \frac{E_2}{E_1} \left(\frac{\sin \gamma' \cos \dot{\alpha} t + \cos \gamma' \cos \beta \sin \dot{\alpha} t}{\cos \gamma' \cos \dot{\alpha} t - \sin \gamma' \cos \beta \sin \dot{\alpha} t} \right) \right\} \quad (C11)$$

can be substituted back into (C10) giving

$$V_R' = V_1 \left| \cos \left[\left(\omega t - \frac{(\phi_o + \phi_x)}{2} \right)_{\max} [\cos \gamma' \cos \dot{\alpha} t - \sin \gamma' \cos \beta \sin \dot{\alpha} t] \right] \right| \\ + V_2 \left| \sin \left[\left(\omega t - \frac{(\phi_o + \phi_x)}{2} \right)_{\max} [\sin \gamma' \cos \dot{\alpha} t + \cos \gamma' \cos \beta \sin \dot{\alpha} t] \right] \right| \quad (C12)$$

where $V_1 = \ell E_1$, $V_2 = \ell E_2$, and ℓ is the effective electrical length.

The voltage V_R' in a coning rocket is equivalent to the voltage V_R , equation 25 of Chapter II in a non-coning rocket. It is seen that the peak amplitude of the signal is modulated by the relative aspect of the ray path and spin axis. If the coning rate were rapid with respect to the rocket velocity, then an averaging process would smooth out coning effects. However, if the altitude change in one precession cycle is significant, then Faraday rotation and differential absorption also change in the cycle and averaging will not yield accurate results. The spin rate must be determined experimentally by magnetometers on the rocket, but theoretically, half-rotations are solutions of the transcendental equation

$$t = \frac{\tan^{-1}}{\dot{\alpha}} \left[\frac{\tan(90^\circ - \dot{\gamma} t)}{\cos \beta} \right] \quad (C13)$$

and correspond to the instant the antenna is parallel to the earth's magnetic field. Equation (C13) is found by setting the element of the

first row and column of matrix PCS equal to zero. If Faraday rotation is zero ($\gamma' = \dot{\gamma}t$), then the 'spin marks' are coincident with the minimum values of (C12).

The complexity of (C12) clouds the easy determination of Faraday rotation and differential absorption. What we need then is a systematic method of deducing these quantities in the case of rocket coning. We have seen that differential absorption and Faraday rotation are related to the relative magnitudes of the major and minor axes of the polarization ellipse and to the spatial angular rotation of the ellipse relative to the ground-based antenna. Consider a rocket held stationary at some point along its trajectory such that γ' , β and the rocket's translational motion are fixed but it is still allowed to spin. Figure C3 illustrates this situation. The orientation of the plane of polarization ($\underline{x}^r, \underline{y}^r$) relative to the antenna plane ($\underline{x}^a, \underline{y}^a$) is determined by γ' and β which are to be measured clockwise from the line of intersection of the two planes. The maximum and minimum signals recorded over one spin cycle of the rocket are respectively proportional to the maximum and minimum projections of \underline{E} into the plane traced out by the spinning antenna. Let \underline{E}_1' be the projection of \underline{E}_1 and \underline{E}_2' that of \underline{E}_2 , where $\underline{E}_1 = E_1 \underline{x}^r$ is the major axis of the polarization ellipse, $\underline{E}_2 = E_2 \underline{y}^r$ is the minor axis, and E_1 and E_2 are given by (19). Because of the symmetry of the problem, consider only values of γ' between 0° and 180° . Let d_1 and d_2 be the respective angular separations between \underline{E}_1' and \underline{E}_2' , and the line of intersection of the two planes. Since d_1 and d_2 lie on opposite sides of the line of intersection, $d = |d_1| + |d_2|$ is the angular separation between \underline{E}_1' and \underline{E}_2' . In general, the projections of two orthogonal vectors like $E_1 \underline{x}^r$ and $E_2 \underline{y}^r$ of Figure C3 onto a plane that is not parallel to the plane of the vectors ($\beta \neq 0$ in Figure C3) are not orthogonal. If $\beta = \pi/2$, then $d = 0$ and \underline{E}_1' and \underline{E}_2' are parallel. The angle between \underline{E}_1 and its projection \underline{E}_1' is called b_1 ,

$$\underline{E}_1' = E_1 \cos(b_1) . \quad (C14)$$

Similarly for \underline{E}_2 ,

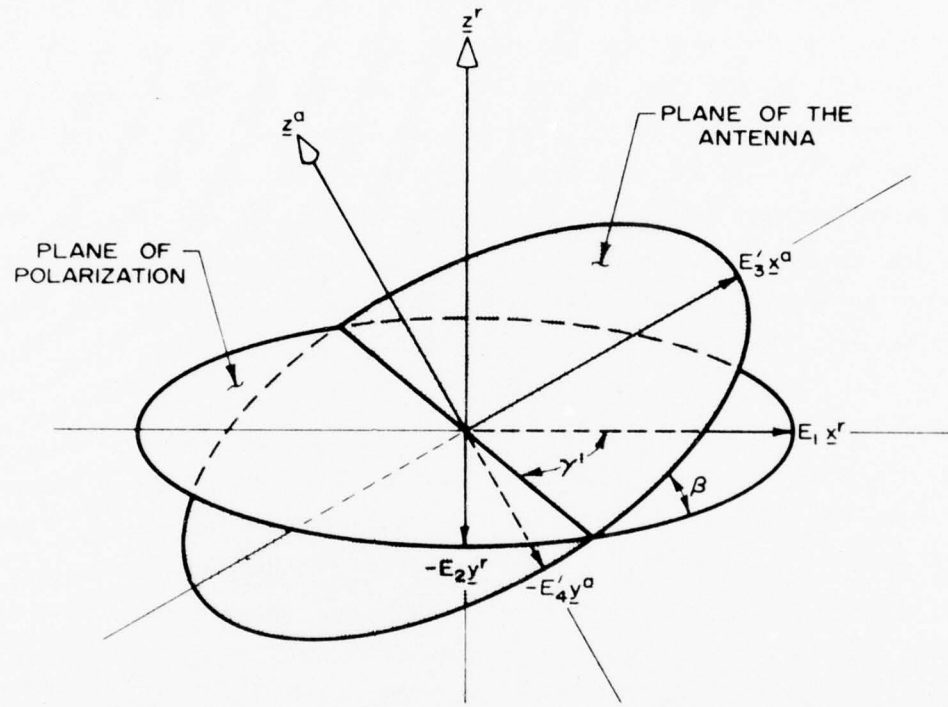


Figure C3. Orientation of the antenna plane (\underline{x}^a , \underline{y}^a) determined by the spinning antenna relative to the plane of polarization for all motion variables except spin held fixed.

$$\underline{E}_2' = E_2 \cos(b_2) \quad (C15)$$

Napier's rules for right spherical triangles give the relationships

$$\sin(b_1) = \sin\gamma' \sin\beta \quad (C16)$$

and

$$\sin(b_2) = \cos\gamma' \sin\beta \quad . \quad (C17)$$

The angles d_1 and d_2 in the plane of the antenna are then given by

$$\sin(d_1) = \tan(b_1) \cot\beta \quad (C18)$$

$$\sin(d_2) = \tan(b_2) \cot\beta \quad . \quad (C19)$$

Some arbitrary vector in the polarization plane \underline{E} can be written in terms of the orthogonal components along \underline{x}^r and \underline{y}^r

$$\underline{E} = E_x \underline{x}^r + E_y \underline{y}^r \quad .$$

These components can be projected onto the plane of the antenna

$$E_x = E_x \cos(b_1)$$

$$E_y = E_y \cos(b_2) \quad .$$

The vector sum of E_x' and E_y' in the antenna plane is given by

$$|\underline{E}'|^2 = \underline{E}' \cdot \underline{E}' = E_x^2 \cos^2 b_1 + E_y^2 \cos^2 b_2 + 2E_x E_y \cos(b_1) \cos(b_2) \cos(d) \quad . \quad (C20)$$

Since \underline{E} lies in the polarization plane, the magnitudes of E_x and E_y are less than or equal to the major and minor axes of the ellipse E_1 and E_2 respectively. Since d is not, in general, equal to 90° , E_1' and E_2' are not orthogonal vectors. Consequently, E_1' may not be the largest value

projected into the plane of the antenna, nor E_2' the smallest. As the phasor \underline{E} rotates in the polarization plane, the minimum value of $|E'|^2$ in the antenna plane from (C20) occurs when $\frac{d|E'|^2}{dE} = 0$. The components E_x and E_y in the plane of polarization satisfy

$$\frac{E_x^2}{E_1^2} = 1 - \frac{E_y^2}{E_2^2} . \quad (C21)$$

Substituting (C21) into (C20), taking the derivative with respect to E_y and setting the result to zero gives

$$C_R - \frac{E_y}{E_2} \left[1 - \left(\frac{E_y}{E_2} \right)^2 \right]^{-\frac{1}{2}} + \frac{E_2}{E_y} \left[1 - \left(\frac{E_y}{E_2} \right)^2 \right]^{\frac{1}{2}} = 0 \quad (C22)$$

where

$$C_R = \frac{E_2 \cos(b_2)}{E_1 \cos(b_1) \cos(d)} - \frac{E_1 \cos(b_1)}{E_2 \cos(b_2) \cos(d)} . \quad (C23)$$

Rearranging (C22) into the binomial form

$$\left(\frac{E_y}{E_2} \right)^4 - \left(\frac{E_y}{E_2} \right)^2 + \left(C_R^2 + 4 \right)^{-1} = 0$$

gives the roots

$$\left(\frac{E_y}{E_2} \right)^2 = 1/2 \pm (1 - R)^{\frac{1}{2}}/2 \quad (C24)$$

where

$$R = \left[\left(\frac{C_R}{2} \right)^2 + 1 \right]^{-1} . \quad (C25)$$

If $E_1' > E_2'$, the smaller value of $(E_y'/E_2')^2$ corresponds to the major axis, while for $E_1' \leq E_2'$, the larger value corresponds to the major axis. The data becomes extremely difficult, if not impossible, to reduce whenever $E_1' \leq E_2'$. After this situation occurs, reduction of the data will be very error-prone. Hence a discussion of this situation will be neglected. Let E_3' and E_4' be the largest and smallest field components respectively in the antenna plane, Figure C3. By combining (C24), (C21) and (C20) for the usual case where $E_1' > E_2'$,

$$\begin{aligned} E_3'^2 &= (1 + R) E_1'^2/2 + (1 - R) E_2'^2/2 \\ &\quad + (4 - R^2)^{\frac{1}{2}} E_1' E_2' \cos(d) \end{aligned} \quad (C26a)$$

and

$$\begin{aligned} E_4'^2 &= (1 - R) E_1'^2/2 + (1 + R) E_2'^2/2 \\ &\quad - (4 - R^2)^{\frac{1}{2}} E_1' E_2' \cos(d) \end{aligned} \quad (C26b)$$

The spin introduced error in Faraday rotation can now be found by determining the angular difference between the "apparent" minor axis E_4' and the "true" minor axis projection E_2' . Since the polarization ellipse projected onto the antenna plane is an ellipse also, the angular difference ξ is given by

$$\xi = \sin^{-1} \left\{ \left[(E_4'/E_2')^2 - 1 \right] \left[(E_4'/E_3')^2 - 1 \right]^{-\frac{1}{2}} \right\}. \quad (C27)$$

The error in differential absorption is

$$\zeta = \left[(E_3'/E_4' - 1) (E_3'/E_4' + 1)^{-1} \right] - A \quad (C28)$$

where A is given by equation (20) of Chapter II. For the usual case where $E_1' > E_2'$, ξ will change sign as γ' increases past a multiple of 90° . Similarly, ζ will change sign as γ' increases past a multiple of some angle between 0° and 90° .

The plots in Figure C4 correspond to the case of a 10 MHz wave being recorded for 10 seconds (over 7.4 km) after propagating through the summer PCA medium to an altitude of 77.8 km. At this point, a differential absorption of about -15 dB has been induced on the signal. The sole difference in input between the two is that in the upper plot, the electron density has been set to zero, while in the lower, N_e is identical to the PCA profile throughout. Rotational parameters of $\dot{\alpha} = 10 \text{ sec}^{-1}$, $\dot{\gamma} = 0.1 \text{ sec}^{-1}$, and $\beta = 30^\circ$ (see Figure C1) were taken as constants over the second interval. In the same fashion as indicated in (19) of Chapter II, $V_1 = \ell E_1$ and $V_2 = \ell E_2$ are the recorded signal borders if there were no coning present (see Figure 6B), and $V_3' = \ell E_3'$ and $V_4' = \ell E_4'$ are the distorted signal borders with coning given by (C26). Thus in the upper plot, the modulation of V_1 and V_2 is illustrated by V_3' and V_4' respectively over one complete cycle of γ' . The slight decrease in the signal amplitude in Figure C4 arises from the increasing distance of the rocket from the source. In the lower plot, the Faraday rotation and differential absorption effects are included to illustrate actual errors that would be incurred in the true signal envelope upon ignoring coning effects in data reduction. Note that $\gamma' = \dot{\gamma}t - F$ no longer completes one cycle as a result of Faraday rotation.

The coning errors induced into the unreduced data are $d\xi/dz$ and $d\zeta/dz$. These errors may be estimated numerically by calculating variations in (C27) and (C28) over small distances in the coded model. For typical coning parameters, when A is less than -10 dB, $d\xi/dz$ can easily be of the same magnitude as dA/dz or greater. The term $d\xi/dz$ is generally much smaller than dF/dz but can also become significant. In general, $d\xi/dz$ and $d\zeta/dz$ are functions of γ' , β and E_1/E_2 . The dependence of $d\xi/dz$ and $d\gamma/dz$ on these variables is non-linear and aperiodic with altitude. Statistical averaging of the unreduced data may still leave significant error. For a higher degree of accuracy it is necessary to monitor the rocket orientation in flight continuously and develop a reduction scheme that will remove the error. The remainder of this appendix will be the development of such a scheme.

In the plane of the antenna, the electric field \underline{E}' , is elliptical and satisfies

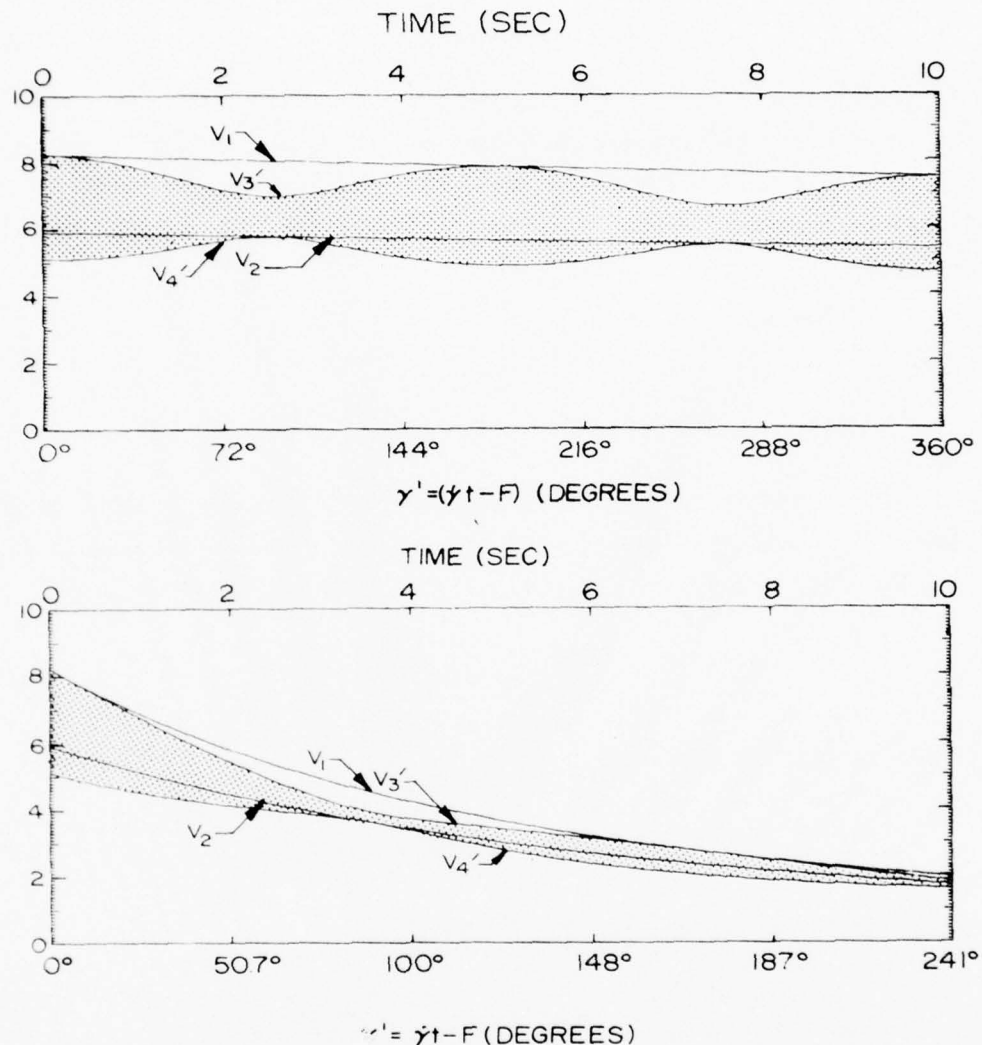


Figure C4. Typical signal modulation by rocket coning-shaded region indicates signal envelope modulation relative to the signal envelope for a non-coning rocket. Shown are modulation effects for zero electron density (top) and the disturbed profile of Figure 7 (bottom). See text for details.

$$\left(\frac{E'_x}{E'_3}\right)^2 + \left(\frac{E'_y}{E'_4}\right)^2 = 1 \quad (C29)$$

where E'_x and E'_y are the orthogonal components of \underline{E}' along E'_3 (x' direction) and E'_4 (y' direction) the major and minor axes of the ellipse respectively. The field components E'_1 and E'_2 can then be broken into the (x' , y') components by

$$\begin{aligned} E'_1 &= E'_1 \cos \theta_1 x' + E'_1 \sin \theta_1 y' \\ E'_2 &= E'_2 \cos \theta_2 x' + E'_2 \sin \theta_2 y' \end{aligned} \quad (C30a)$$

where θ_1 and θ_2 are the angles measured from x' to E'_1 and E'_2 respectively, see Figure C5. Note that $d = \theta_1 + \theta_2$, where d is given by the sum of $|d_1|$ and $|d_2|$ in (C18) and (C19). Substitution of (C30a) into (C29) gives

$$E'^2/E'^2_3 = (E'^2_3/E'^2_4 \sin^2 \theta_1 + \cos^2 \theta_1)^{-1} \quad (C31a)$$

and (C30b) into (C29) yields

$$E'^2/E'^2_3 = (E'^2_3/E'^2_4 \sin^2 \theta_2 + \cos^2 \theta_2)^{-1} \quad (C31b)$$

Combining (C26a) and (C26b) gives

$$(E'_3)^2 + (E'_4)^2 = (E'_1)^2 + (E'_2)^2 \quad (C32)$$

which with (C31) and some rearranging gives

$$\tan^2 \theta_1 \tan^2 \theta_2 = \left(\frac{E'_4}{E'_3}\right)^4 .$$

Solving the above expression simultaneously with $d = |d_1| + |d_2|$ leads to a binomial form having roots

$$\tan \theta_1 = -[(K - 1)\tan(d)]/2 - \sqrt{[(K - 1)\tan(d)]^2/4 - K}^{1/2} \quad (C33a)$$

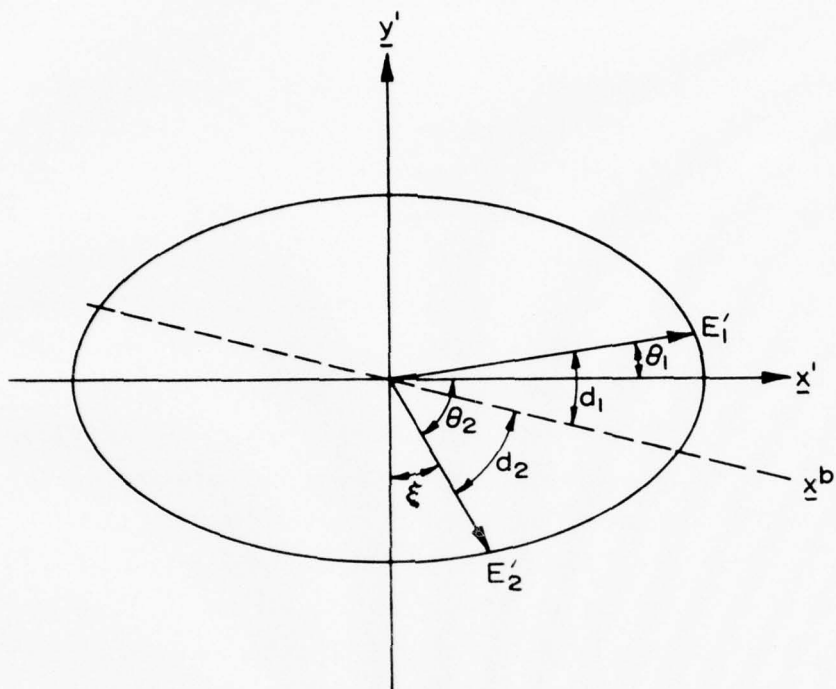


Figure C5. E-field components in the plane of the antenna.

and

$$\tan \theta_2 = -[(K - 1)\tan(d)]/2 - \left\{ [(K - 1)\tan(d)]^2/4 - K \right\}^{1/2} \quad (C33b)$$

where $K = (E'_4/E'_3)^2$. If $d = |d_1| + |d_2|$ is found from (C16), (C17), (C18) and (C19) and K is known, θ_1 and θ_2 can be found from (C33). Solution of (C30), (C14) and (C15) then gives E_1/E_2 which is the ratio needed for the calculation of A . The rate of change of A with altitude $\frac{dA}{dz}$ follows immediately.

Analytically, the Faraday rotation coning error introduced by measuring the difference between signal minima and spin marks is

$$\frac{d\xi}{dz} = \frac{\Delta F'}{\Delta z} - \frac{dF}{dz} \quad (C34)$$

where $\Delta F'$ is the change in angular separation between signal minima and spin marks over the interval Δz , and dF/dz is the true Faraday rotation rate. The calculation of $d\xi/dz$ is not difficult, and then dF/dz can be found from the measured value $\Delta F'/\Delta z$.

Consider an altitude interval Δz_i that is small enough that the quantities dF/dz_i and dA/dz_i may be considered constant over this interval. These quantities uniquely determine electron density N_e^i and collision frequency V_m^i within this interval. This will permit reduction of the data measured over Δz_i independent of measurements at other altitudes. The ratio of the minimum to maximum signal as shown in Figure 9 is the quantity $V_4'/V_3'|_i = E_4'/E_3'|_i$ assuming linear reception. The parameter F_i is the angular separation between signal minima and spin marks. The angular separation between precession marks and signal minima is $\gamma_i' \approx \gamma_t - F_i$. There is an error term in this assumption, arising from the presence of ξ_i in F_i , as in (C34). This is ultimately a second-order error term, however, since γ_i' is used for correcting coning error itself. The precession marks can be determined from magnetometer data by a process similar to determination of the spin marks. Angle β_i can be determined from the amplitude of the magnetometer data at z_i . With the four tabulated functions $V_u'/V_3'|_i$, γ_i' , F_i , and β_i discussed above, the data reduction for the k^{th} interval, $\Delta z_k = z_k - z_{k-1}$, is:

- 1) Calculate from (C16), (C17), (C18), and (C19) the parameters b_1^i , b_2^i , d_1^i , d_2^i , and $d_i = d_1^i + d_2^i$ for $i = k, k-1$.
- 2) Calculate θ_1^i and θ_2^i , $i = k, k-1$ from (C33).
- 3) From (C31) the ratios $(E_1'/E_3')^2|_i$ and $(E_2'/E_3')^2|_i$, $i = k, k-1$ can be calculated.
- 4) Calculate $E_1'/E_2|_i$ from (C14) and (C15) for $i = k, k-1$.
- 5) From (18) and (17) calculate A_i for $i = k, k-1$. Then $dA/dz|_k = (A_k - A_{k-1})/(z_k - z_{k-1})$
- 6) Calculate ξ_i from (C27) for $i = k, k-1$. Note that $E_4'/E_2|_i = [E_4'/E_3|_i][E_2'/E_3|_i]^{-1}$.
- 7) Calculate $dF/dz|_k$ from (C34) where $\Delta F'_k = F'_k - F'_{k-1}$, and $d\xi/dz|_k = (\xi_k - \xi_{k-1})/\Delta z_k$.

- 8) Iterate collision frequency v_m^k and electron density N_e^k by the expressions

$$N_e^k = \frac{dF/dz|_k N_e^{k'}}$$

$$v_m^k = \frac{dF/dz|_k}{dF/dz|_k'} \frac{dA/dz|_k}{dA/dz|_{k'}} v_m^{k'}$$

where $N_e^{k'}$ and $v_m^{k'}$ are initial assumed values, and $dF/dz|_{k'}$ and $dA/dz|_{k'}$ are the rate equations found by substituting $v_m^{k'}$ and $N_e^{k'}$ into the Sen-Wyller equations. By replacing k' with k , the above expressions rapidly converge to N_e^k and v_m^k . This last step is used by *Mechtly et al.*, [1967] and *Bennett et al.*, [1972].

It was shown in Chapter III that reliable differential absorption data can be obtained at somewhat lower altitudes than Faraday rotation data. At these low altitudes, coning errors are insignificant. The procedure given by *Mechtly et al.*, [1967] and *Bennett et al.*, [1972] is to extrapolate the collision frequency to lower altitude by assuming it is proportional to pressure; $v_m(z) = k p(z)$. *Dickenson et al.*, [1976] state that a proportionality to density $\rho(z)$ may be a better assumption, however. The first equation in step (8) above can be used to determine the lower electron density values if $v_m(z)$ is extrapolated.

In actual practice there may prove to be better ways to determine the quantities F' , γ' , and β but this is beyond the scope of this paper and will not be discussed.